SAIMM
THE SOUTHERN AFRICAN INSTITUTE OF MINING AND METALLURGY
VOLUME 126 NO. 7 JULY 2026

Enaex
Africa

REDUCING BLAST VIBRATIONS
WITHOUT COMPROMISING PRODUCTIVITY.

- Lower PPV
- Better fragmentation
- Increased precision
- Community confidence

DaveyTronic® 5

Precision you can measure. Performance you can trust.

Millisecond timing accuracy, advanced diagnostics and intelligent electronic initiation designed to improve blast control, enhance safety and support more sustainable mining operations.

Contact Us

Enaex Africa
Dunkeld Office
Oxford Parks, 2nd Floor
199 Oxford Road, Dunkeld
Johannesburg, South Africa.

Telephone:
+27 11 911 3412

enaex@enaex.com

Humanizing Mining | through Precision Blasting.

OFFICE BEARERS AND COUNCIL FOR THE 2025/2026 SESSION

President
G.R. Lane

President Elect
T.M. Mmola

Senior Vice President
M.H. Solomon

Junior Vice President
S.J. Ntsoelengoe

Incoming Junior Vice President
M.C. Munroe

Immediate Past President
E. Matinde

Honorary Treasurer
W.C. Joughin

Ordinary Members on Council

W. Broodryk	M.A. Mello
A.D. Coetzee	K. Mosebi
Z. Fakhraei	M.J. Mothomogolo
B. Genc	S.M. Naik
F. Lake	G. Njowa
K.M. Letsoalo	S.M. Rupprecht
S.B. Madolo	A.T. van Zyl

Co-opted Council Members
K.W. Banda
M.L. Wertz

Past Presidents Serving on Council

N.A. Barcza	W.C. Joughin
R.D. Beck	C. Musingwini
Z. Botha	J.L. Porter
V.G. Duke	M.H. Rogers
I.J. Geldenhuys	G.L. Smith
R.T. Jones	

M.L. Wertz – TP Mining Chairperson
W. Broodryk – TP Metallurgy Chairperson

C.T. Chijara – YPC Chairperson
T.S. Ndlela – YPC Vice Chairperson

Branch Chairpersons

Botswana	K. Mosebi
DRC	Vacant
Johannesburg	A. Hefer
Limpopo	M.S. Zulu
Namibia	T. Aipanda
Northern Cape	Vacant
North West	T. Nsimbi
Pretoria	P.G.H. Pistorius
Western Cape	M.H. Solomon
Zambia	N.M. Kazembe
Zimbabwe	L. Shamu
Zululand	Vacant

PAST PRESIDENTS

*Deceased

* W. Bettel (1894–1895)
* A.F. Crosse (1895–1896)
* W.R. Feldtmann (1896–1897)
* C. Butters (1897–1898)
* J. Loevy (1898–1899)
* J.R. Williams (1899–1903)
* S.H. Pearce (1903–1904)
* W.A. Caldecott (1904–1905)
* W. Cullen (1905–1906)
* E.H. Johnson (1906–1907)
* J. Yates (1907–1908)
* R.G. Bevington (1908–1909)
* A. McA. Johnston (1909–1910)
* J. Moir (1910–1911)
* C.B. Saner (1911–1912)
* W.R. Dowling (1912–1913)
* A. Richardson (1913–1914)
* G.H. Stanley (1914–1915)
* J.E. Thomas (1915–1916)
* J.A. Wilkinson (1916–1917)
* G. Hildick-Smith (1917–1918)
* H.S. Meyer (1918–1919)
* J. Gray (1919–1920)
* J. Chilton (1920–1921)
* F. Wartenweiler (1921–1922)
* G.A. Watermeyer (1922–1923)
* F.W. Watson (1923–1924)
* C.J. Gray (1924–1925)
* H.A. White (1925–1926)
* H.R. Adam (1926–1927)
* Sir Robert Kotze (1927–1928)
* J.A. Woodburn (1928–1929)
* H. Pirow (1929–1930)
* J. Henderson (1930–1931)
* A. King (1931–1932)
* V. Nimmo-Dewar (1932–1933)
* P.N. Lategan (1933–1934)
* E.C. Ranson (1934–1935)
* R.A. Flugge-De-Smidt (1935–1936)
* T.K. Prentice (1936–1937)
* R.S.G. Stokes (1937–1938)
* P.E. Hall (1938–1939)
* E.H.A. Joseph (1939–1940)
* J.H. Dobson (1940–1941)
* Theo Meyer (1941–1942)
* John V. Muller (1942–1943)
* C. Biccard Jeppe (1943–1944)
* P.J. Louis Bok (1944–1945)
* J.T. McIntyre (1945–1946)
* M. Falcon (1946–1947)
* A. Clemens (1947–1948)
* F.G. Hill (1948–1949)
* O.A.E. Jackson (1949–1950)
* W.E. Gooday (1950–1951)
* C.J. Irving (1951–1952)
* D.D. Stitt (1952–1953)
* M.C.G. Meyer (1953–1954)
* L.A. Bushell (1954–1955)
* H. Britten (1955–1956)
* Wm. Bleloch (1956–1957)
* H. Simon (1957–1958)
* M. Barcza (1958–1959)
* R.J. Adamson (1959–1960)
* W.S. Findlay (1960–1961)
* D.G. Maxwell (1961–1962)
* J. de V. Lambrechts (1962–1963)
* J.F. Reid (1963–1964)
* D.M. Jamieson (1964–1965)
* H.E. Cross (1965–1966)
* D. Gordon Jones (1966–1967)
* P. Lambooy (1967–1968)
* R.C.J. Goode (1968–1969)
* J.K.E. Douglas (1969–1970)
* V.C. Robinson (1970–1971)
* D.D. Howat (1971–1972)
* J.P. Hugo (1972–1973)
* P.W.J. van Rensburg (1973–1974)
* R.P. Plewman (1974–1975)
* R.E. Robinson (1975–1976)
* M.D.G. Salamon (1976–1977)
* P.A. Von Wielligh (1977–1978)
* M.G. Atmore (1978–1979)
* D.A. Viljoen (1979–1980)
* P.R. Jochens (1980–1981)
* G.Y. Nisbet (1981–1982)

A.N. Brown (1982–1983)

* R.P. King (1983–1984)

J.D. Austin (1984–1985)

* H.E. James (1985–1986)

H. Wagner (1986–1987)

* B.C. Alberts (1987–1988)
* C.E. Fivaz (1988–1989)
* O.K.H. Steffen (1989–1990)
* H.G. Mosenthal (1990–1991)

R.D. Beck (1991–1992)

* J.P. Hoffman (1992–1993)
* H. Scott-Russell (1993–1994)

J.A. Cruise (1994–1995)
D.A.J. Ross-Watt (1995–1996)
N.A. Barcza (1996–1997)

* R.P. Mohring (1997–1998)

J.R. Dixon (1998–1999)
M.H. Rogers (1999–2000)
L.A. Cramer (2000–2001)

* A.A.B. Douglas (2001–2002)
* S.J. Ramokgopa (2002-2003)

T.R. Stacey (2003–2004)
F.M.G. Egerton (2004–2005)
W.H. van Niekerk (2005–2006)
R.P.H. Willis (2006–2007)
R.G.B. Pickering (2007–2008)
A.M. Garbers-Craig (2008–2009)
J.C. Ngoma (2009–2010)
G.V.R. Landman (2010–2011)
J.N. van der Merwe (2011–2012)
G.L. Smith (2012–2013)
M. Dworzanowski (2013–2014)
J.L. Porter (2014–2015)
R.T. Jones (2015–2016)
C. Musingwini (2016–2017)
S. Ndlovu (2017–2018)
A.S. Macfarlane (2018–2019)
M.I. Mthenjane (2019–2020)
V.G. Duke (2020–2021)
I.J. Geldenhuys (2021–2022)
Z. Botha (2022-2023)
W.C. Joughin (2023-2024)
E. Matinde (2024-2025)

Typeset and Published by
The Southern African Institute of Mining and Metallurgy
PostNet Suite #212
Private Bag X31
Saxonwold, 2132
E-mail: journal@saimm.co.za

Printed by
Camera Press, Johannesburg

SAIMM
THE SOUTHERN AFRICAN INSTITUTE OF MINING AND METALLURGY

VOLUME 126 NO. 7 JULY 2026

Contents

Journal Comment: The second century is a choice
by J. Zietsman iv

President's Corner: From strengthening an institution to stewarding a system
by G.R. Lane ..... v-vi

Honorary Legal Advisers
M H Attorneys

Auditors
Genesis Chartered Accountants

Secretaries
The Southern African Institute of Mining and Metallurgy
7th Floor, Rosebank Towers, 19 Biermann Avenue,
Rosebank, 2196
PostNet Suite #212, Private Bag X31, Saxonwold, 2132
E-mail: journal@saimm.co.za

ISSN 2225-6253 (print) · ISSN 2411-9717 (online)

SAIMM PYROMETALLURGY INTERNATIONAL CONFERENCE PAPERS

Upgrading of ferruginous manganese tailings by hydrogen-rich reduction for the ferroalloy industry
by D.A. Barrett, M. Tadie, B. von der Heyden, R. Cromarty 385
This paper investigated the prereduction of ferruginous manganese tailings from the Nchwaning mine. Selected conditions achieved the highest Mn/Fe ratio of 4.52 and an Mn grade of 57 wt.%. While below the desired target specification (Mn/Fe of at least 7.5 wt.% and Mn grade 44 wt.%), such targets can be met by blending the product stream with other low-grade Mn ores that contain minimal Fe. These findings highlight the potential for the upgradation of ferruginous manganese tailings.

Dissolution of SiO_2 in SiO_2-CaO-Al_2O^3 slags
by M. B. Folstad, M. Zhu, M. Tangstad 395
The dissolution rate of silica (SiO_2) into different compositions of SiO_2-CaO-Al_2O_3 slags was studied at 1500 °C and 1550 °C under an inert atmosphere of argon. The results show that the dissolution process is controlled by mass transfer of SiO_2 in the slag. The experimental results were used to evaluate the dissolution rate, which was found to increase with increasing CaO/Al_2O_3 ratios as well as with increasing temperature.

Reduced order model for isothermal pre-reduction of chromite pellets with hydrogen
by M. Khama, Q.G. Reynolds, B.S. Xakalashe 405
Pre-reducing chromite with hydrogen offers significant benefits. For this purpose, computational models were developed. The Thiele modulus method was used to predict the degree of reduction, the diffusion of gases through the product layer, the unreacted core radius of the grain radius, and local and global conversion. The final conversion deviates from the experimentally calculated conversion by a maximum relative error of 2.7% while the initial conversions differ significantly, reaching a maximum error of 65%.

Technology evolution in the Southern African Ni-Cu-PGM smelting industry
by R. Hundermark, G. Marsden, R. Snodgrass, K. van der Merwe 411
The Southern African Ni-Cu-PGM smelting industry has evolved significantly, with smelting technology development closely linked to processing more concentrate and to addressing the changes of concentrates from the various platinum group metals-containing reef types. With the outlook in demand for PGMs changing as a function of automotive requirements, smelting technology will continue to evolve for enhancement of safety and environmental protection, reduced costs, and greater efficiencies.

Impact of feed mixture control on arc behaviour in direct-current arc furnace smelting of chromite – a modelling study
by Q.G. Reynolds, M.W. Erwee, S. Swanepoel, R. Fourie 427
Unexpected excursions in electrode hoist position are occasionally observed on direct-current arc furnace plants producing ferrochromium. One possible mechanism is variations in feed reductant balance altering the freeboard gas composition and the thermophysical properties of the arc plasma. This hypothesis is investigated and results show that these two effects act in opposing directions and largely cancel one another. Future investigation is proposed.

The second century is a choice

The SAIMM Pyrometallurgy International Conference convened in May 2026 under the theme Foundations for Competitiveness and Sustainability. The theme was chosen because, since 2014, more than 2.2 million tonnes of ferroalloy smelting capacity have been curtailed or closed. By early 2026, only 11 of 66 ferrochrome smelters were operating, while record tonnages of raw chrome ore left our ports — carrying with them the 80% of value that smelting would have captured at home. These facts are where sound engineering begins, and foundations are what must now be rebuilt.

Our community answered. For the first time, pyrometallurgy, furnace tapping, and refractories convened as three symposia in one gathering, under one SAIMM pyrometallurgy banner — a deliberate consolidation carrying a message to industry and government alike: foundations are laid together. One hundred and nine papers from fifteen countries filled the programme. The selection in this special edition shows a discipline that is alert, rigorous, and determined.

The week opened with the PyroFuZA Workshop — the Future of Pyrometallurgy in South Africa — where some fifty senior leaders from industry and government deliberated as equals. Every participant affirmed that this industry is worth saving; the overwhelming majority affirmed that it can be saved. And for the first time, a fifty-year horizon was accepted as meaningful: South Africa as a world leader in high-temperature science and technology. Work on the vision, roadmap, and five-year plan is now in preparation.

A century ago, Hendrik van der Bijl laid the foundations on which our industry grew: power, steel, and patient capital. Those foundations have expired. Our endowment has not. The richest ore bodies on earth still lie in our ground, demand for what we make keeps growing, and our people remain at the global frontier of the discipline. Together they will carry us to the fifty-year vision. What stands between decline and a second century is not thermodynamics. It is choices — made together, and made now.

Read these papers as working drawings for that second century. Then let us restart the engine room of our economy — together.

J. Zietsman
Chair: SAIMM Pyrometallurgy International Conference 2026

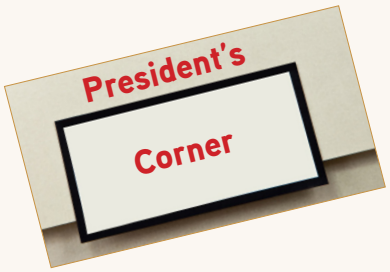

From strengthening an institution to stewarding a system

It is often said that a picture speaks a thousand words. As I reflected on the journey of the past 11 months, I realised that the accompanying illustration captures its evolution more clearly than a list of activities or achievements ever could.

It has been an incredible year—shaped by conversations, relationships, tough questions, unexpected insights, and an increasingly clear understanding of the constraints facing the minerals industry and the role SAIMM must play in addressing them.

When I began my presidency, my commitment was straightforward: to help strengthen SAIMM.

A strong professional institute requires an effective operating model, clear governance, capable leadership, disciplined execution, and a value proposition relevant to its members and the industry it serves. Much of the early work therefore focused on strengthening SAIMM from within.

That work remains important. An institution cannot address the needs of its industry unless it has the capability to perform its own role effectively.

However, as the year progressed, my perspective began to change.

Through hundreds of engagements with students, young professionals, university leaders, experienced practitioners, mining and metallurgical companies, technical associations, professional bodies, regulators, and industry leaders, a common pattern gradually emerged.

Universities are under pressure. Structured workplace development is inconsistent. Mentoring capacity is limited. Progression to professional registration is slow. The pool of experienced technical practitioners is diminishing, specialist knowledge is at risk of being lost, and the industry is becoming increasingly complex.

The challenge is therefore not simply whether we are producing enough graduates. It is whether the professional capability system is consistently developing the technicians, technologists, professionals, specialists, mentors, and future leaders required to operate, improve, and lead an increasingly complex industry.

This led to the defining insight of the year:

One of the most significant constraints facing the future of the minerals industry is a fragmented and weakening professional capability system—one that no single organisation can rebuild alone.

The question guiding my presidency consequently evolved from:

How do we strengthen SAIMM to how must SAIMM evolve to help address the capability constraints facing the minerals industry?

I began the year looking inward at SAIMM. Listening led me to look outward at the industry. The pattern that emerged revealed a system constraint—and that changed what I believe SAIMM must become.

Professional capability does not develop within a single institution. It emerges through an interconnected system involving education, workplace experience, mentoring, professional registration, technical communities, knowledge sharing, and continuing professional development.

When these elements work together, capability develops and compounds. When they become fragmented, people are lost between stages, development becomes inconsistent, and the industry gradually loses the technical depth and professional competence on which its future depends.

What became increasingly clear to me is that capability must be treated as an endowment in its own right—deliberately built, renewed, and protected, just as the industry invests in its mineral resources and in the physical and digital assets required to develop it.

Without the people capable of operating, improving, and leading increasingly complex businesses, neither the resource endowment nor the asset base can be converted into sustainable value.

President's Corner (continued)

SAIMM must therefore evolve beyond the traditional boundaries of a membership institute to become a more industry-facing professional institution. This means beginning with the present and future needs of the minerals industry and aligning its programmes, partnerships, knowledge platforms, and development pathways with the people and capabilities the industry requires.

Its role is not to serve the short-term interests of any individual organisation, but to provide an independent platform through which the industry's longer-term capability needs can be understood and addressed.

SAIMM should not attempt to own the professional capability system or replace the organisations already working within it. Its contribution is to help the system function more effectively: to convene, connect, enable capability development, preserve knowledge, provide an independent professional voice, and steward the long-term health of the system.

Strengthening SAIMM was therefore not displaced by the wider capability agenda. It became the foundation from which the Institute could contribute to it.

This thinking has already begun to take practical form through the strengthening of SAIMM's operating model, the development of the SAIMM Academy, deeper engagement with universities and industry, and new collaborative platforms focused on workplace development and the professional pipeline.

The work, however, is only beginning. Capability develops over many years, while a presidency lasts for only one. The true measure of this year will not be the number of initiatives started. It will be whether the thinking continues, the connections deepen, and SAIMM helps the industry to develop the people and capabilities required for its future.

I am deeply grateful to everyone across SAIMM, academia, industry, and the wider professional community who shared their perspectives and contributed to this journey. Every conversation added something to the picture.

The year reinforced a belief that has shaped much of my professional life: sustainable performance is achieved not by continually demanding greater effort from people, but by designing better systems through which people can develop, contribute, and succeed.

I began the year wanting to strengthen an institution.

I now have a deeper appreciation that the purpose of strengthening SAIMM is to enable it to address the needs of the minerals industry and strengthen the professional capability system upon which that industry depends.

The future of the minerals industry will be determined not only by the resources we possess, but by the capability of the people we develop and the professional capability system we collectively build and sustain.

Strengthen the institution. Connect the system. Steward the future.

G.R. Lane
President, SAIMM

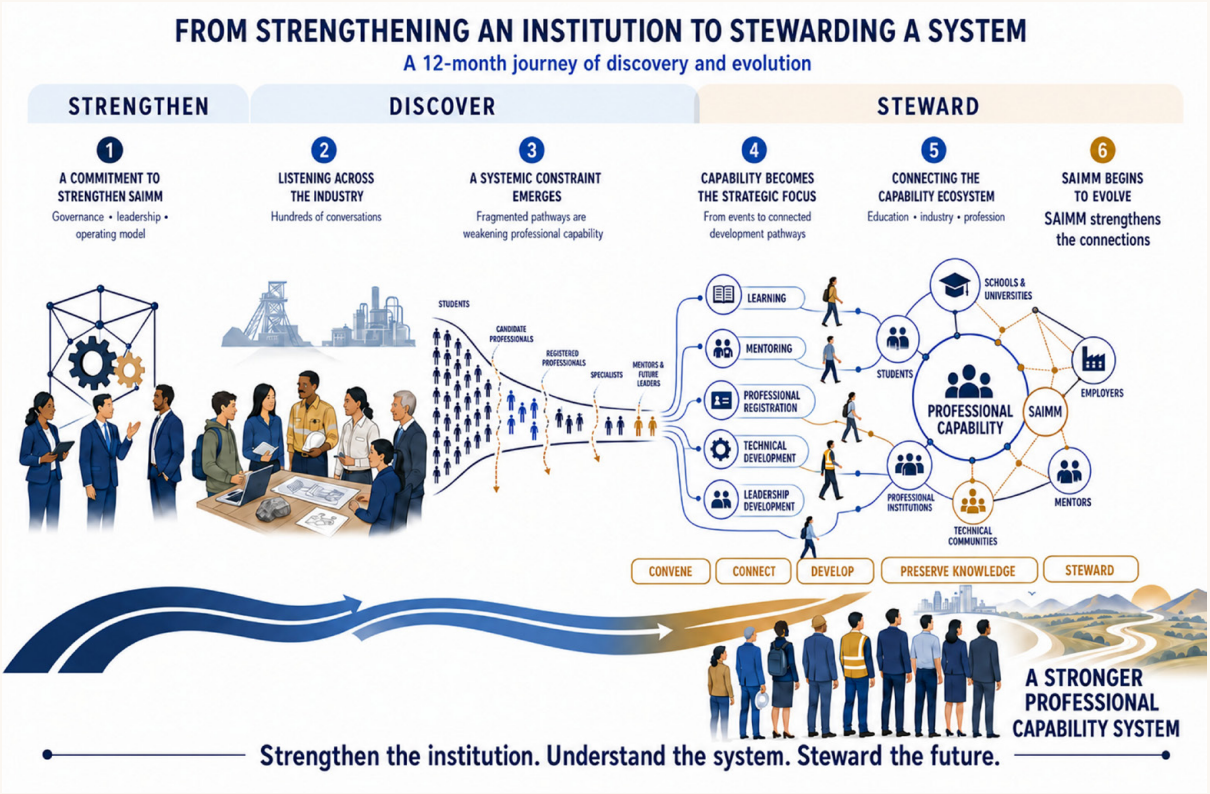

Upgrading of ferruginous manganese tailings by hydrogen-rich reduction for the ferroalloy industry

by D.A. Barrett[1], M. Tadie[1], B. von der Heyden[1], R. Cromarty[2]

Affiliation:
[1]African Rainbow Minerals Chair in Geometallurgy, Stellenbosch University, South Africa
[2]University of Pretoria, South Africa

Correspondence to:
D.A. Barrett

Email:
19barrda@gmail.com

Dates:
Received: 19 May. 2026
Published: July. 2026

How to cite:
Barrett D.A., Tadie M. von der Heyden B. Cromarty R. 2026. Upgrading of ferruginous manganese tailings by hydrogen-rich reduction for the ferroalloy industry. *Journal of the Southern African Institute of Mining and Metallurgy*, vol. 126, no. 7, pp. – 385 - 394

DOI ID:
https://doi.org/10.17159/2411-9717/1007/2026

ORCiD:
D.A. Barrett
https://orcid.org/0009-0006-4390-0502
M. Tadie
https://orcid.org/0000-0003-3111-5188
B. von der Heyden,
https://orcid.org/0000-0002-4006-9278
R Cromarty
https://orcid.org/0000-0002-2424-040X

This paper is based on a presentation given at the SAIMM Pyrometallurgy International Conference 2026, 26-28 May 2026, CSIR International Convention Centre, Pretoria, South Africa

Abstract

This paper investigated the prereduction of ferruginous manganese tailings from the Nchwaning mine by isothermal reduction between 650 °C and 1050 °C. The treated tailings underwent subsequent magnetic separation to upgrade the Mn/Fe ratio and manganese grade so that the tailings can be used as high-quality ferroalloy feedstock. The tailings contain recoverable manganese but is penalised by elevated and complex iron content. There is a high degree of mineralogical variability found in the untreated tailings. Iron is present both as hematite and in solid solution within manganese minerals such as bixbyite, braunite, and braunite II. A hydrogen atmosphere was used in this paper as it is sufficiently reducing to produce metallic iron that can be separated magnetically. Lime and silica additives were investigated to determine their influence on Fe reduction kinetics and globule formation, which impacts the separability of Fe and Mn. Optical microscopy and SEM analysis of the treated material revealed distinct metallurgical behaviour between iron reduced from hematite – forming larger globules (50 µm to 600 µm) – and iron reduced from Mn-hosted phases, which formed smaller globules (0.1 µm to 2 µm). Relatively milder reducing conditions achieved the highest Mn/Fe ratio of 4.52 and an Mn grade of 57 wt.%. While below the desired target specification (Mn/Fe of at least 7.5 wt.% and Mn grade of at least 44 wt.%), this can still be met by blending the product stream with other low-grade Mn ores that contain minimal Fe. These findings highlight the potential for the upgradation of ferruginous manganese tailings.

Keywords

gravity concentration, trough length, heavy mineral sands, recovery

Introduction

Manganese is a mineral of global economic importance due to its contributions to the steel industry, where it is utilised to deoxidise and desulfurise steel, as well as increase its hardness, toughness, and strength (Cairncross, Beukes, 2013; Wellbeloved et al., 1997). Whilst high-grade manganese ores can be product-tailored for ferroalloy production, lower-grade material, including tailings, may require feed preparation because smelting behaviour can be unpredictable, and will likely result in a reduced energy efficiency. Further, the loss of value through tailings and unutilised low-grade ore negates maximum resource utilisation efficiency. For material to be used as smelter feed in high-quality ferroalloy production, a manganese grade of at least 44 wt.% Mn and a Mn/Fe ratio of at least 7.5 is required after the blending of different ores and fluxes (Elliott, Barati, 2020). This paper focused on ferruginous manganese tailings obtained from the slimes dam at the Nchwaning mine in the Kalahari Manganese Field, however the results should be applicable to similar secondary materials. The material had an elevated and complex iron content that necessitates the selective removal of iron from the tailings for it to be used as smelter feed for ferroalloy production.

The selective removal of iron can be achieved using physical, hydrometallurgical, or pyrometallurgical beneficiation steps, or in combination. In most cases, physical processing steps alone are not sufficient to separate Fe from Mn (Singh et al., 2020). Hydrometallurgical methods show promise but pyrometallurgical beneficiation approaches have been chosen as the focus for this paper (Liu et al., 2019; Singh et al., 2020; You et al., 2017). Pyrometallurgical steps include the separation of the pre-reduction stage of smelting in the flowsheet that enables the upgrade of material and simultaneously reduces energy requirements (Larssen et al., 2020; Davies et al., 2023; Ernst et al., 2024; Schanche, Tangstad, 2021; Sarkar et al., 2024). Magnetic separation can be combined with pre-reductive roasting in flowsheet development to upgrade the material by selectively removing iron-rich phases that have a higher magnetic susceptibility, such as metallic iron or magnetite, from the manganese-rich phases, such as manganosite, following pre-reduction (Matabadal, 2022; Kivinen et al., 2010; Mpho et al., 2013).

Studies on Nchwaning ore have provided insights into the behaviour of this material during reduction in a CO-CO_2 environment. Previous research on the ferruginous Nchwaning ore has shown little success in upgrading the Mn/Fe ratio (Matabadal, 2022), underlining the need for further work towards this end. The primary reason the process did not achieve the desired Mn/Fe ratio was the formation of a FeO-MnO solid solution oxide phase that was difficult to reduce further and hindered magnetic separation of Fe and Mn (Matabadal, 2022). The formation of this composite oxide in ferruginous Mn ore has also been reported in other research studies under CO-CO_2 atmosphere conditions (El-Geassy et al., 2008; Zhang et al., 2017; Gao et al., 2019; Liu et al., 2019; Larssen et al., 2020; Davies et al., 2023). Pre-reduction roasting in the traditional CO-CO_2 atmosphere is therefore unlikely to yield the desired results. The use of hydrogen in the atmosphere has been shown to enhance both the extent and rate of reduction, resulting in the formation of metallic Fe, which is more readily separable in magnetic separation (Ernst et al., 2024). Furthermore, the addition of lime and/or silica flux to the unreduced ore has yielded mixed results in reducing iron and manganese oxides. Some studies have shown that the addition of CaO promoted Fe whisker formation (Zhong et al., 2017; Şeşen, 2001; Zhao et al., 2013), while others suggested that the formation of porous Fe layers increased the rate of reduction (Prakash et al., 2000; Shigematsu, Iwai, 1993; Ostrovski et al., 2004). Further, the investigation by Turkdogan and Vinters (1973) found that the addition of CaO retarded reduction, while the addition of SiO_2 had a negligible effect. Shigematsu and Iwai (1993) also found that the addition of SiO_2 can increase the rate of reduction of FeO to Fe. Interaction effects between the additives and original minerals will be limited as no liquid is formed at the considered reduction temperatures, but the additives can still influence reduction through solid state diffusion and ion diffusion (Zhao et al., 2013).

This paper investigated the pre-reduction of ferruginous manganese tailings from the Nchwaning mine in a hydrogen-rich atmosphere, followed by magnetic separation as a beneficiation process to produce ferroalloy smelter feed, aiming to support flowsheet development. To be suitable for ferroalloy smelter feed, the target specifications were an Mn grade of at least 44 wt.% and an Mn/Fe ratio of at least 7.5, while maximising Mn recovery.

Materials and methods

This paper conducted a thorough experimental design that investigated the influence of four key process variables: reduction temperature, degree of hydrogen enrichment, the addition of CaO, and the addition of SiO_2. The experimental approach is summarised in Figure 1. All drying was conducted at 110 °C for twelve hours to remove any surface moisture. The material was split into representative 30 g samples using a rotary splitter. The dried material had a D_{50} of 185 µm. The fine particle size required briquetting before being reduced, where polyvinyl alcohol was used as a binder. All magnetic separation was performed using a Davis tube, a wet magnetic separator, at a single, controlled magnetic intensity with 0.6A being fed to the electromagnet.

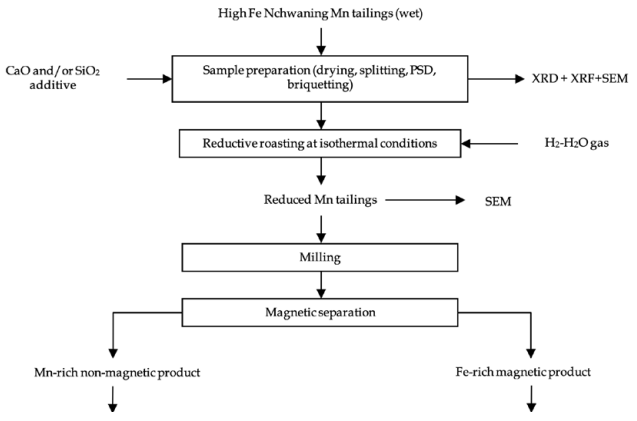

Figure 1—Summary of experimental approach and material flow

A controlled atmosphere retort furnace made of Kanthal APMT was used for all experimental runs. The schematic of the setup is shown in Figure 2. Gasses were fed to the controlled atmosphere furnace at the bottom, which allowed for them to be heated to the required temperature before entering. The retort was lowered into a chamber furnace during use. The gas flow was controlled using multiple gas flow controllers (MFC), and the water vapour was added to the inlet gas using a bubbler in a temperature-controlled water bath to entrain the vapour in the bubbled gas. Heating and cooling of the furnace was carried out in a nitrogen atmosphere. Hydrogen gas was introduced at a constant flow rate 2 NL/min, with a reduction time of two hours.

A central composite design was employed in this investigation; to represent curvature in response behaviour and to quantify the influence of interactions between process variables (Montgomery, 2013). The process conditions for the reduction temperature and the degree of hydrogen enrichment were selected using the iron oxide stability diagram in Figure 3. Manganese readily reduces to MnO before the reduction of iron oxides so the manganese oxide stability diagram is not necessary (Larssen et al., 2020). The reduction conditions, shown in red in Figure 3, were chosen to be well within

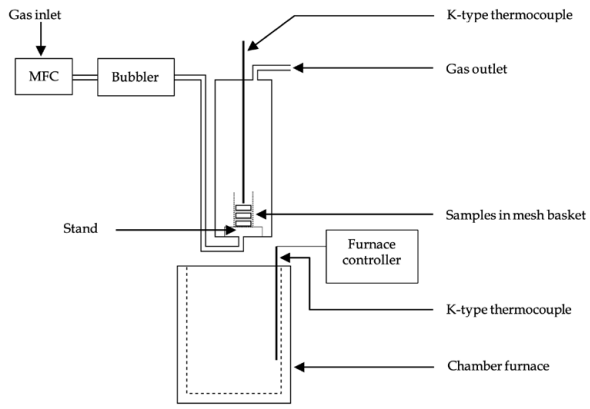

Figure 2—Controlled atmosphere furnace schematic

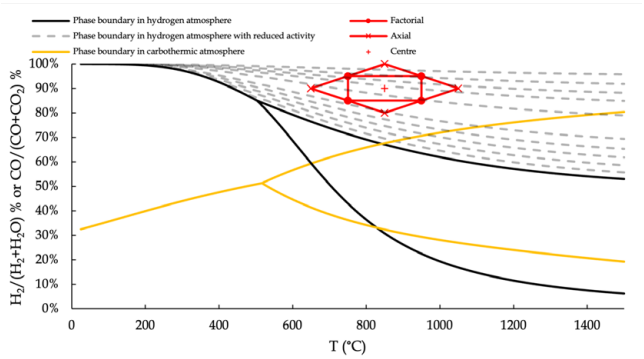

Figure 3—Iron oxide stability diagram in both carbothermic and hydrogen-enriched atmospheres with variable FeO activity. Experimental conditions investigated are marked in red, and the activity of FeO is indicated on each respective dashed line. Data obtained from FactSage (Bale et al., 2002)

Table 1
Summary of process conditions

Variable	High level	Low level	Centre point	High axial point	Low axial point
Temperature (°C)	950	750	850	1050	650
H2/(H2+H2O) (%)	95	85	90	100	80
CaO addition (wt.%)	6	2	4	8	0
SiO2 addition (wt.%)	6	2	4	8	0

Table 2
Chemical composition (wt.%) of untreated Nchwaning material according to X-ray fluorescence

	Mn	Fe	Ca	Si	Mg	Al	Na	P	Ti	L.O.I
Wt.%	44.52	17.42	3.39	1.67	0.26	0.10	0.04	0.02	0.02	2.86

Table 3
Mineral distribution of major Mn minerals in untreated Nchwaning material according to SEM-EDS analysis

Mineral	Bixbyite	Braunite	Braunite II	Manganite
Formula	$(Mn, Fe)2O_3$	$3(Mn, Fe)2O_3{\cdot}MnSiO_3$	$7(Mn, Fe)_2O_3{\cdot}CaSiO_3$	Ɣ-MnOOH
Wt.% of Mn minerals	26.5	15.2	54.5	3.8

the metallic Fe stability region, to promote the formation of metallic Fe, even when the activity of FeO is reduced. The dosage levels for CaO and SiO_2 were determined using the studies by Zhao et al. (2013) and Shigematsu and Iwai (1993) as guidelines. The levels used for each response variable are summarised in Table 1.

Results and discussion

Characterisation

The chemical composition of the untreated samples is presented in Table 2, with the Central Analytical Facility at Stellenbosch University conducting the X-ray fluorescence analysis. The material had an acceptable Mn grade of 44.5 wt.%, but was penalised by an elevated Fe content, which results in a low Mn/Fe ratio of 2.56.

X-ray diffraction was conducted by XRD Analytical and Consulting in Pretoria. The analysis revealed that the Nchwaning material contained five types of manganese minerals, making up 70.5 wt.% of the sample. Important minerals included braunite (61.2 wt.%), manganite (8.0 wt.%), hematite (23.2 wt.%), and calcite (6.1 wt.%). Only braunite and manganite made up more than one wt.% of the sample among the Mn minerals, and the analysis was unable to differentiate between braunite, braunite II, and bixbyite, as Cu k*a* radiation was used. To accurately account for the different Mn minerals, a bulk SEM-EDS analysis of the untreated material was conducted. The analysis normalised the number of cations for each candidate mineral, then used a charge balance to match each mineral grain to the most probable phase, according to the method proposed by Schumacher (1991). The distribution of the major Mn minerals present in the sample is presented in Table 3, with braunite II being the most abundant phase.

The Mn grade and the Fe content in the sample was highly variable from grain to grain, resulting in high variability in the Mn/Fe ratio as well. The distribution in Mn/Fe ratio for the major manganese minerals is illustrated in Figure 4, with braunite II exhibiting the lowest Mn/Fe ratio. The target Mn/Fe ratio to be suitable for ferroalloy production is 7.5, indicated by the dashed red line in Figure 4. The proportion of grains with a Mn/Fe ratio of less than 7.5 was 7%, 50%, and 76% for bixbyite, braunite, and braunite II, respectively, with 64% of the total Mn grains falling below this.

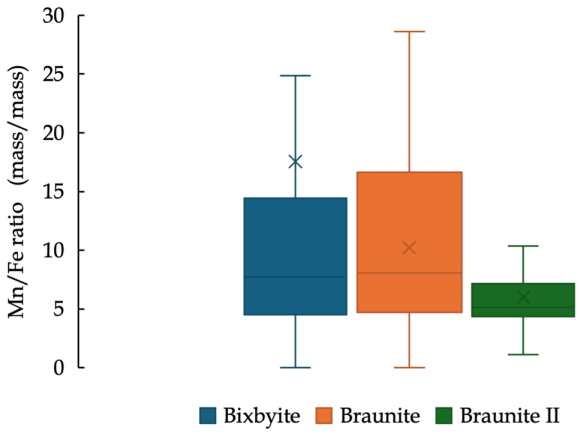

Figure 4—Box and whisker plot showing Mn/Fe ratio in manganese minerals

Therefore, braunite II posed the most significant challenge in upgrading the Mn/Fe ratio.

The manganese minerals also contained a high degree of iron present in solution, with up to 39 wt.% of the total iron in the sample being found in these Mn minerals. The Mn mineral grains were found to contain up to 20.4 wt.% Fe, with braunite II having a mean Fe content of 12.3 wt.%. These high concentrations of Fe in manganese minerals fall within expected theoretical limits, with work by Momoi et al. (1985) finding up to 40 wt.% Fe in synthesised ferrian braunite. The high iron content complicated separation as the highest possible Mn/Fe ratio achievable was 6.33, if all hematite present was removed, without removing the iron in the Mn minerals. Therefore, to achieve an Mn/Fe ratio of 7.5, Fe had to be separated from the Mn minerals as well, or the most ferruginous Mn grains had to be removed.

Experimental results

The results of the XRF analysis of the treated magnetic and non-magnetic fractions were used to calculate the Mn/Fe ratio, Mn grade, and Mn recovery to the non-magnetic stream. The highest Mn/Fe ratio achieved was 4.52 for an experimental run where all operating conditions were at their low level (Table 1). This test run also resulted in an Mn grade of 57.4 wt.% and an 85.5% recovery of Mn.

Following reduction, the metallic iron that formed was found to have distinctly different sized globules, depending on mineral that the iron was initially associated with. The size analysis was performed using Fiji image processing software. The metallic iron that formed from the reduction of hematite resulted in larger particles with a feret diameter from 50 µm to 600 µm, while the metallic iron globules that formed from the iron in solid solution in manganese minerals resulted in small particles with a feret diameter between 0.1 µm to 2 µm. The particle size distribution (PSD) after milling influences the liberation of the metallic iron, and therefore the subsequent separation efficiency. The iron particles are more likely to be well liberated if the particle size is fine, however, this would result in higher milling costs and increase the difficulty of solids handlings. The D_{80} passing size for the milled material was 80.6 µm, which makes it unlikely that the small iron globules would be well liberated.

Statistical modelling

Statistical analysis, using Statistica, was used to isolate the influence of each factor on the response variables. Second-order models were regressed for each response using response surface methodology. The models yielded adjusted R^2 values of 0.77, 0.81, and 0.83 for the Mn/Fe ratio, Mn grade, and Mn recovery to the non-magnetic stream, respectively. Pareto charts were used to select statistically significant factors for further analysis.

Changes in the reduction temperature and degree of hydrogen enrichment had similar influences on all response variables, as they both determine the reduction conditions present. However, the reduction temperature had a more significant influence on the response variables than the degree of hydrogen enrichment. As the temperature increased, the amount of mass reporting to the magnetic stream initially increased sharply before plateauing at higher temperatures as reduction reached completion (Figure 5). This is due to the reduction from wustite (FeO) to metallic Fe being the last to occur, thus increasing the magnetic susceptibility of the treated sample. The addition of silica had a positive interaction effect with the reduction temperature on the mass pull, where the influence of SiO2 addition is negligible at low temperatures but markedly increases the mass pull at temperatures greater than 850 °C.

The predicted influence of each the lime and silica additions on the Mn grade of the non-magnetic stream is presented in Figure 6. The error bars represent the 95% confidence interval for the model. Both additives had a negative impact on the Mn grade, due to diluting the overall stream. The addition of CaO was not found to have a significant influence on any other response variable. Therefore, CaO did not influence the reduction process, which is supported by the perfectly linear negative relationship between lime addition and Mn grade. On the other hand, the addition of SiO_2 also dilutes the stream initially, but the Mn grade plateaus at higher addition levels due to the interaction effect between the reduction temperature and silica addition.

The predicted influence of each reduction temperature and the silica additions on the Mn/Fe ratio is presented in Figure 7. The Mn/Fe ratio decreased sharply with the initial increase in reduction temperature, then plateaued at higher temperatures as the full extent of reduction was reached. The higher reduction temperature caused more Fe globules to form in Mn grains, which were not adequately liberated during milling, resulting in excess Mn being carried to the magnetic stream – therefore lowering the Mn/Fe ratio in the non-magnetic stream as the reduction temperature increased. The addition of silica initially lowered the Mn/Fe ratio, before reaching a minimum Mn/Fe at about 4 wt.% SiO_2 added and increased thereafter due to the interaction between SiO_2 and the reduction temperature.

Mineral texture analysis

A detailed mineral texture analysis of the treated samples was conducted to better understand the behaviour seen in the statistical models. This analysis was performed using SEM-EDS and optical microscopy in combination. All textural analysis is performed on the treated samples before milling and magnetic separation.

At the lowest temperature, that is, 650°C, not all the treated hematite grains were fully reduced, thus limiting the degree of separability due to a difference in magnetic susceptibility. No iron globules were found to form in the Mn mineral grains. When the reduction temperature reached 750 °C, all treated

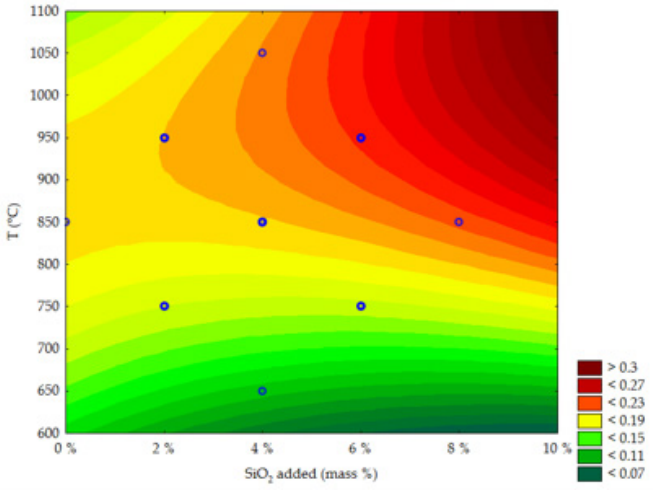

Figure 5—Response contour showing the predicted mass pull to the magnetic stream with respect to both the mass of silica added and the reduction temperature when both other factors are at their centre point level (H2 = 90% and CaO added = 4 wt.%)

hematite was fully reduced (Figure 8), with only small regions in the middle of metallic Fe globules within treated hematite exhibiting incomplete reduction. These mostly reduced Fe globules in Figure 8, which illustrates how the reduction proceeds from the outside of the globule towards the centre due to mass transfer limitations as the dense metallic iron layer forms , as well as the porous nature of the grain. These large pure metallic Fe grains should have been well liberated and reported to the magnetic stream during magnetic separation.

The treated manganese mineral grain, illustrated in Figure 9, has

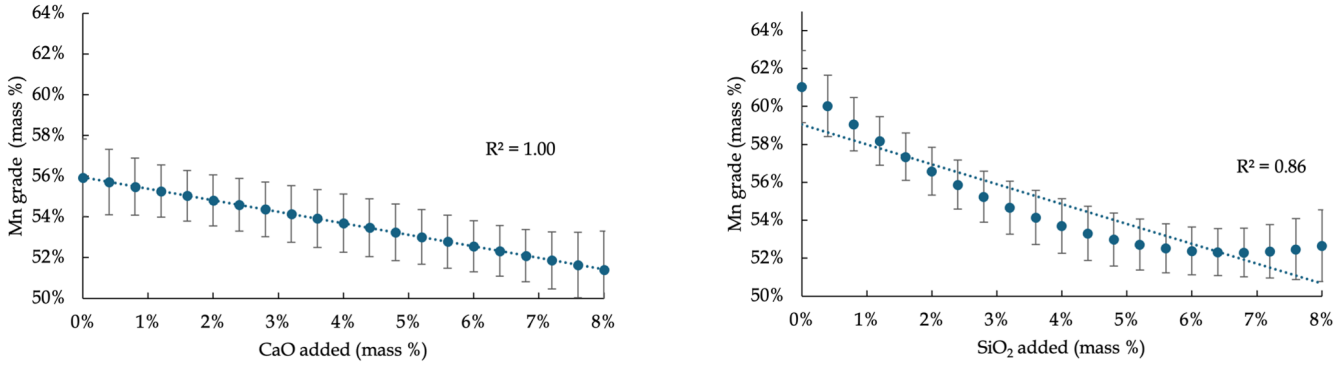

Figure 6—Curves showing the predicted change in manganese grade in the non-magnetic stream with respect to (a) the mass of lime added, and (b) the mass of silica added when all other factors are at their centre point level (T = 850°C, H_2 = 90%, CaO added = 4 *w*t.%, and SiO_2 added = 4 *w*t.%)

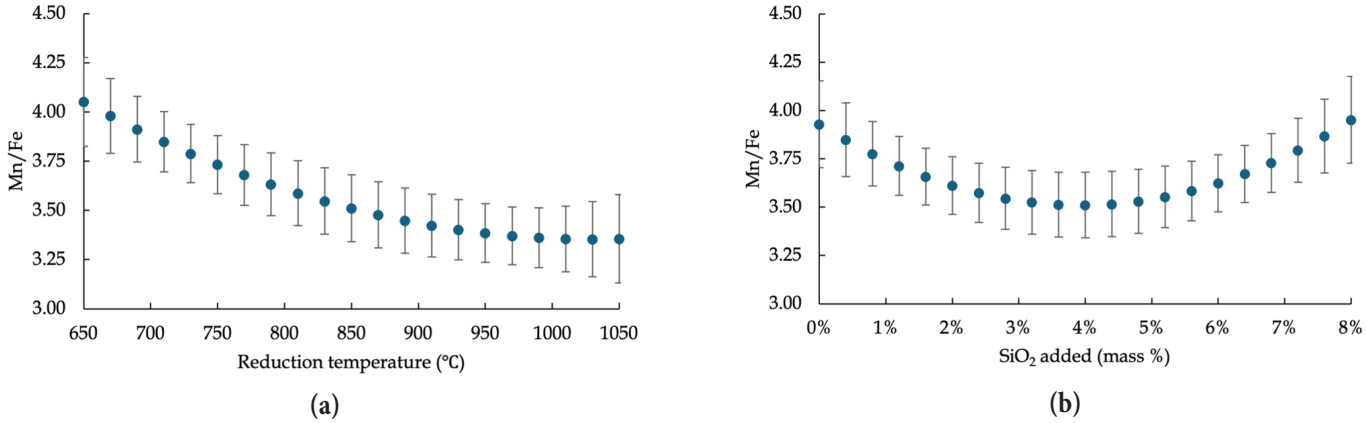

Figure 7—Curves showing the predicted change in Mn/Fe in the non-magnetic stream with respect to (a) the reduction temperature, and (b) the mass of silica added when all other factors are at their centre point level (T = 850°C, H_2 = 90%, CaO added = 4 wt.%, and SiO_2 added = 4 wt.%)

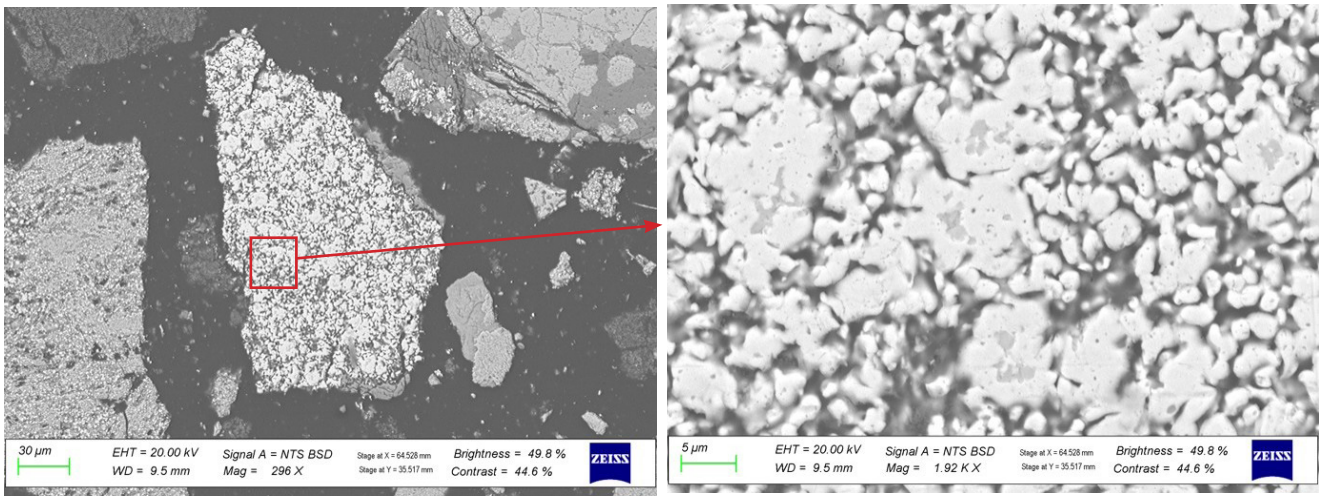

Figure 8—SEM images illustrating treated hematite at (a) 296x, and (b) 1920x. Sample treated at 750 °C; 85% H_2; 2 wt.% CaO added; 6 wt.% SiO_2 added

been reduced to form a stable solution of manganosite containing wustite and other minor impurities. This grain contained 13.1 wt.% iron, the highest iron content found in this experimental run without any Fe-alloy globules forming. The median Fe content for braunite II was 11.8 wt.%, and the overall median Fe content for Mn minerals was 10.5 wt.% for the Nchwaning material. Therefore, most Mn mineral grains did not have a high enough Fe content for Fe-alloy globules to form. Without the formation of any Fe-alloy globules to increase the magnetic susceptibility, these grains should have correctly reported to the non-magnetic stream. The grains illustrated in Figure 9 and Figure 10 are from the best performing experimental run.

The treated manganese mineral grain (Figure 10) had a higher Fe content (20.3 wt.% Fe) than the grain in Figure 9. The higher Fe content resulted in Fe-alloy globules forming with a median Feret diameter of 0.74 µm. These globules contained 70.0 wt.% Fe and 23 wt.% Mn. The globules would have increased the magnetic susceptibility of their associated particle after milling and will likely have reported to the magnetic stream, along with any entrained Mn, lowering the Mn/Fe of the non-magnetic stream.

The trend where a higher Fe content in Mn mineral grains resulted in Fe-alloy globules forming, was evident in all test runs. Additionally, a lower iron content was required for globules to form in stronger reducing conditions. These observations are summarised in Table 4, with Fe-alloy globules forming in grains with lower Fe content in relatively stronger reducing conditions (850 °C and at least 90% H2). This behaviour was due to the relationship between the activity of a phase and its concentration (Ganguly, 2001).
In stronger reducing conditions, the threshold to form Fe-alloy globules was lower, and these globules therefore formed in more Mn mineral grains. Thus, raising their magnetic susceptibility and causing more entrained Mn to incorrectly report to the magnetic stream, which resulted in a decreased Mn/Fe ratio in the non-magnetic stream at stronger reducing conditions. This behaviour could be used, in conjunction with variable magnetic intensity of the magnetic separator, to target Mn grains with the highest Fe and separate on a grain by grain basis, rather than only the Fe-alloy globules.
In experimental runs with both an elevated temperature (> 850 °C)

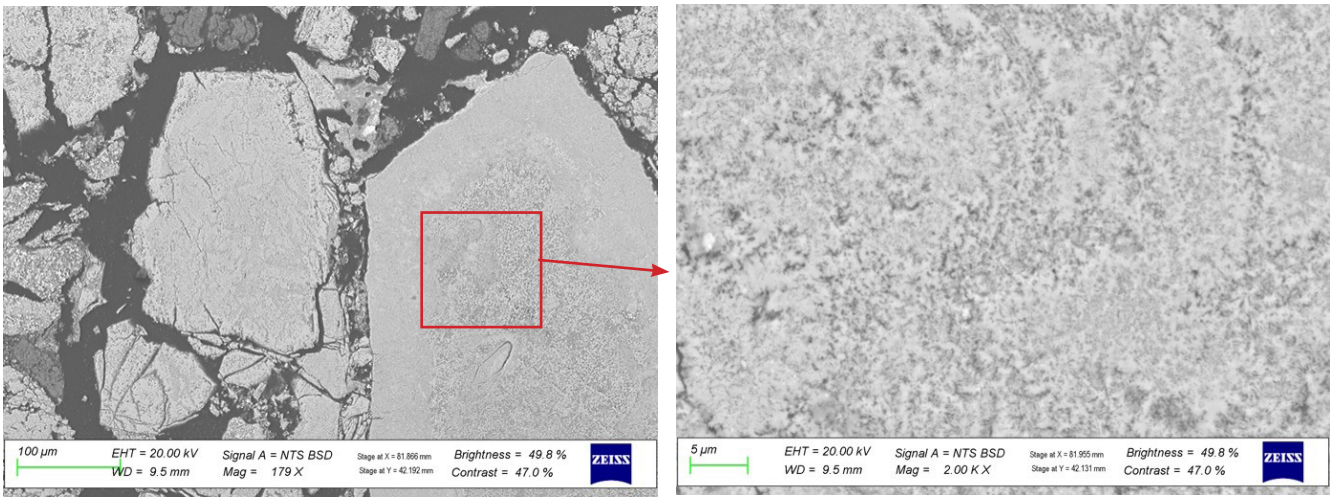

(a) (b)

Figure 9—SEM images illustrating a treated manganese mineral grain with no Fe-alloy flecks at (a) 179x, and (b) 2000x. Sample treated at 750 °C; 85% H_2; 2 *w*t.% CaO added; 2 *w*t.% SiO_2 added

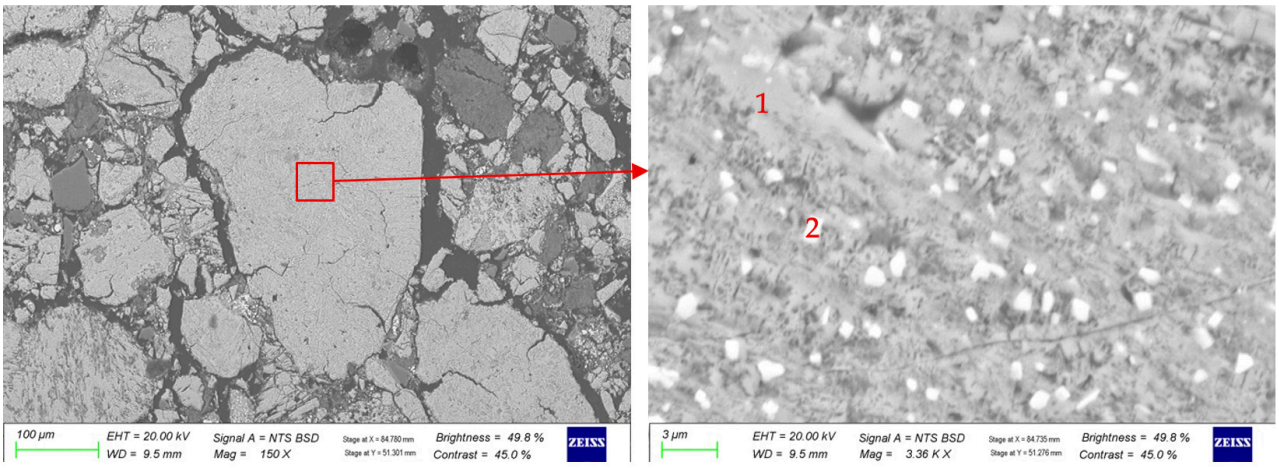

(a) (b)

Figure 10—SEM images illustrating a treated manganese mineral grain with Fe-alloy flecks at (a) 150x, and (b) 3360x. The labels in (b) refer to (1) Mn oxide and (2) Fe alloy. Sample treated at 750°C; 85% H_2; 2 wt.% CaO added; 2 wt.% SiO_2 added

and silica additions (> 4 wt.% added), a new structure was found in treated manganese mineral grains with an elevated Si and Ca level, likely braunite II, illustrated in Figure 11. Most Mn mineral grains contained just the manganese-rich oxide phase and Fe-alloy globules, if they formed. This new structure also contained an Mn-Ca silicate phase that contains 21 wt.% Mn, 20 wt.% Ca, 14 wt.% Si, and 5 wt.% Fe – whereas the Mn oxide phase contained 74 wt.% Mn, 3 wt.% Fe, 3 wt.% Ca, and 2 wt.% Si. The most important difference, due to its ramifications on the magnetic separability of Mn, is the formation of large, thin Fe-alloy globules that were not likely to have been liberated well during milling. Therefore, the formation of this new structure in treated braunite II grains resulted in an increased mass pull to the magnetic stream and a decreased Mn/Fe ratio in the non-magnetic stream. This behaviour accounts for the interaction effect between the reduction temperature and silica additions that was discussed during the statistical analysis, although it is unclear what mechanism could be causing it. It is noted that the doped silica is not likely to have transported into the grain, as no liquid phases should have formed during reduction at the experimental conditions investigated. Therefore, the elevated Ca and Si in the Mn-Ca silicate phase likely originate from the original braunite II grain, and are merely more concentrated in this new phase.

Suppose perfect liberation of all metallic Fe, formed from the

Table 4

Comparison of Fe contents in Mn mineral grains required for Fe-alloy globules to begin forming

T (°C)	H_2 (%)	Highest Fe bulk without globules (wt.%)	Lowest Fe bulk with globules (wt.%)
750	85	13.1	13.6
750	85	8.6	16.8
650	90	21.0	62.2
850	80	5.3	11.0
850	100	4.0	7.4
850	90	5.4	7.7

Table 5

Comparison of theoretical maximum Mn/Fe achievable and actual performance from experimental runs

T (°C)	H_2 (%)	CaO added (wt.%)	SiO_2 added (wt.%)	Average Mn/Fe initial	Average Mn/Fe oxide	Mn/Fe achieved in non-magnetic stream	Per cent achieved
750	85	2	2	3.75	5.47	4.52	67.3
750	85	6	2	4.08	5.11	4.22	65.3
850	100	4	4	5.11	9.42	3.55	14.6
950	95	6	6	N/A	20.20	3.58	5.8
850	90	4	4	7.24	10.23	3.53	12.8

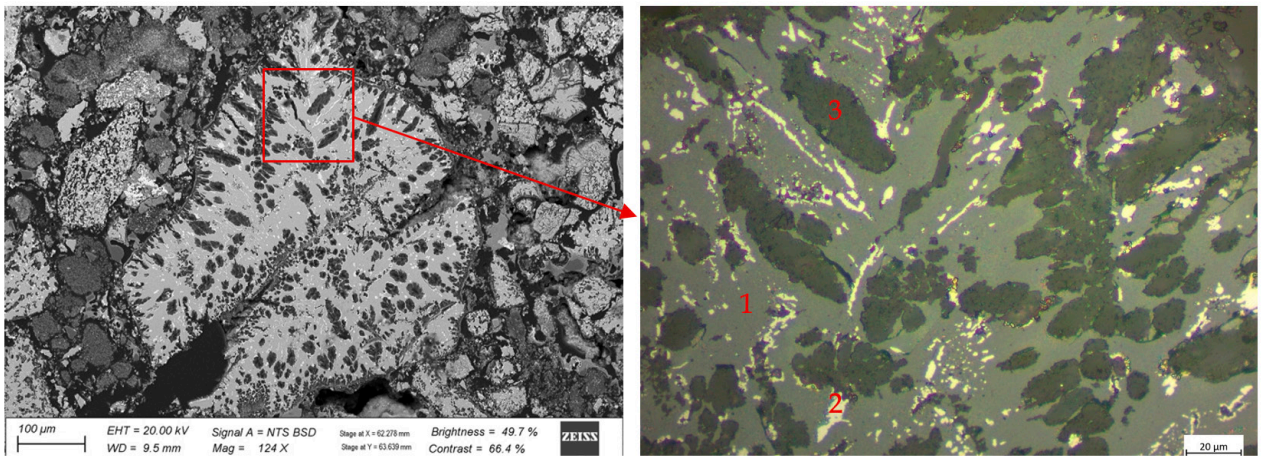

(a) (b)

Figure 11—Images illustrating a treated manganese mineral grain taken using (a) SEM, and (b) an optical microscope. The labels in (b) refer to (1) Mn oxide, (2) Fe alloy, and (3) Mn-Ca silicate. Sample treated at 950°C; 95% H2; 6 wt.% CaO added; 6 wt.% SiO2 added

reduction of both hematite and Fe-alloy globules in Mn minerals, and then the perfect subsequent magnetic separation were possible. In that case, the theoretical maximum Mn/Fe ratio that can be achieved was the Mn/Fe ratio in the oxide. Iron that remained trapped in solution with the Mn oxide will not be separated. To understand how well the magnetic separation worked, the actual upgrade in Mn/Fe (from the initial ratio of 2.56) can be compared to the theoretical upgrade possible (Table 5). The experimental runs with relatively milder reducing conditions (750 °C and 85% H_2) had a lower theoretical maximum Mn/Fe ratio, due to much of the iron remaining in solid solution, but they achieved more than 65% of this maximum. Conversely, the runs with relatively stronger reducing conditions had a much higher theoretical maximum Mn/Fe due to the formation of Fe-alloy globules, but these same globules cause entrained manganese to report to the incorrect stream, and less than 15% of this maximum is achieved. The alloy globules that form with the Mn minerals are too small to be well liberated after milling.

Conclusions

The hydrogen-rich reductive roast followed by magnetic separation process was investigated for its suitability in upgrading ferruginous manganese tailings from the Nchwaning mine tailings dam. The goal of the process was to upgrade the material to be suitable for ferroalloy production, which requires a manganese grade of 44 wt.% and an Mn/Fe ratio of at least 7.5.

The results of the optimisation study indicate that the target Mn/Fe ratio was not achievable within the investigated range of process conditions. The best conditions achieved an Mn/Fe ratio of 4.52, an Mn grade of 57.4 wt%, and a manganese recovery of 85.5 wt. at 750 °C, 2 wt.% CaO added, 2 wt.% SiO_2 added, and in 85% H_2. While the Mn/Fe ratio is below the desired 7.5, the high Mn grade of 57.4 wt.% means that the product can be blended with low-grade carbonate ores with a low Fe content to produce higher quality ferroalloy smelter feed.

The mineralogical variability had a significant influence on the reductive roasting and subsequent magnetic separation. The variable Fe content in Mn grains was found to determine whether Fe-alloy globules were likely to from under specific reducing conditions. The stronger the reducing conditions, the lower the threshold Fe content required to form Fe-alloy globules. At reduction temperatures of 950 °C or higher (and with elevated silica), the treated braunite II grains were found to form a new Mn-Ca silicate phase that allowed for the formation of larger Fe-alloy globules. However, the PSD of the phases after milling, and the intensity of the magnetic separator did not allow for these Fe globules to be well liberated and subsequently separated.

The statistical analysis revealed that relatively weaker reducing conditions resulted in the best Mn/Fe ratio, Mn grade, and Mn recovery. This behaviour was due to the reducing conditions being still strong enough to entirely reduce the discrete hematite particles into metallic Fe without reducing much of the Fe within the solid solution in Mn grains. The metallic Fe was well liberated and therefore efficiently separated. Stronger reducing conditions led to the formation of magnetic Fe-alloy globules in Mn grains, which were poorly liberated after milling, causing some of these globules to report to the magnetic stream along with associated Mn. The loss of Mn to the magnetic stream resulted in a decreased Mn/Fe ratio, Mn grade, and Mn recovery.

Recommendations

The biggest obstacle to the separation of Mn and Fe was the degree of liberation of the iron alloy globules that formed in the manganese grains. The size of the Fe globules formed was too small to feasibly liberate via conventional milling. It is therefore recommended to investigate a narrower temperature range with more experimental levels that focuses on only generating Fe globules in high Fe manganese minerals, then separate these larger particles rather than focusing on those less than 2 µm in diameter. The strength of the magnetic field can also be added as a parameter to better separate the Fe particles.

Silica additions had a significant influence on the reduction and subsequent magnetic separation, but no conclusive evidence was found regarding the exact mechanism by which this was achieved. It is therefore recommended to conduct further tests that focus on this, and utilise extensive mineral characterisation, such as QEMSCAN, to better understand the mechanisms at play.

References

Bale, C.W., Chartrand, P., Degterov, S.A., Eriksson, G., Hack, K., Mahfoud, R.B., Melancon, J., Pelton, A.D., Petersen, S. 2002. FactSage Thermochemical Software and Databases. Calphad, vol. 26, pp. 189–228.

Cairncross, B., Beukes, N.J. 2013. The Kalahari Manganese Field: The Adventure Continues, Struik Nature.

Davies, J., Tangstad, M., Schanche, T.L., Du Preez, S.P. 2023. Pre-reduction of United Manganese of Kalahari Ore in CO/CO2, H2/H2O, and H2 Atmospheres. *Metallurgical and Materials Transactions B*, vol. 54, pp. 515–535.

El-Geassy, A.A., Nasr, M.I., Omar, A.A., Mousa, E.A. 2008. Isothermal reduction behaviour of MnO2doped Fe2O3compacts with H2at 1073–1373 K. *Ironmaking & Steelmaking*, vol. 35, pp. 531–538.

Elliott, R., Barati, M. 2020. A review of the beneficiation of low-grade manganese ores by magnetic separation. *Canadian Metallurgical Quarterly*, vol. 59, pp. 1–16.

Ernst, M.S., Tangstad, M., Du Preez, S.P. 2024. Pre-reduction of Nchwaning manganese ore in CO/CO2, H2/H2O, and H2 atmospheres. *Minerals Engineering*, vol. 216.

Ganguly, J. 2001. Thermodynamic modelling of solid solutions. *EMU Notes in Mineralogy.*

Gao, L., Liu, Z., Pan, Y., Feng, C., Chu, M., Tang, J. 2019. Systematic study on separation of Mn and Fe from ferruginous manganese ores by carbothermic reduction roasting process: Phase transformation and morphologies. *Journal of Materials Research and Technology*, vol. 8, pp. 5591–5609.

Kivinen, V., Krogerus, H., Daatvittila, J. 2010. Upgrading of Mn/Fe Ratio of Low-Grade Manganese Ore for Ferromanganese Production. *The Twelth International Ferroalloys Congress, 2010 Helsinki.*

Larssen, T.A., Senk, D., Tangstad, M. 2020. Reduction of Manganese Ores in CO-CO2 Atmospheres. *Metallurgical and Materials Transactions B*, vol. 52, pp. 363–381.

Liu, B., Zhang, Y., Lu, M., Su, Z., Li, G., Jiang, T. 2019. Extraction and separation of manganese and iron from ferruginous

manganese ores: A review. *Minerals Engineering*, vol 131, pp. 286–303.

Matabadal, Y. 2022. Evaluation of the Reduction Roast-Magnetic Separation Process to Upgrade Low-Grade Ferruginous Manganese Ore Fines. MEng, *University of Pretoria*.

Momoi, H., Horikawa, M., Fujino, K. 1985. Synthesis and characterisation of ferrian braunite. *Mineralogical Journal*, vol. pp. 12, 367–375.

Montgomery, D.C. 2013. Design and Analysis of Experiments. 8th ed.: John Wiley & Sons.

Mpho, M., Samson, B., Ayo, A. 2013. Evaluation of reduction roasting and magnetic separation for upgrading Mn/Fe ratio of fine ferromanganese. *International Journal of Mining Science and Technology*, vol. 23, pp. 537–541.

Ostrovski, O., Anacleto, N., Ganguly, S. 2004. Reduction of manganese ores by methane-containing gas. Tenth International Ferroalloys Congress, 2004 Cape Town, South Africa.

Prakash, S., Goswami, M.C., Mahapatra, K.S., Ghosh, K.C., Das, S.K., Sinha, A. N., Mishra, K.K. 2000. Morphology and reduction kinetics of fluxed iron ore pellets. *Ironmaking & Steelmaking*, vol. 27.

Sarkar, A., Schanche, T.L., Wallin, M., Safarian, J. 2024. Evaluating the Reaction Kinetics on the H2 Reduction of a Manganese Ore at Elevated Temperatures. *Journal of Sustainable Metallurgy,* vol. 10, pp. 2085–2103.

Schanche, T.L., Tangstad, M. 2021. Prereduction of Nchwaning Ore in CO/CO2/H2 Gas *Mixtures. Minerals*, vol. 11.

Schumacher, J.C. 1991. Empirical ferric iron corrections: necessity, assumptions, and effects on selected geothermobarometers. *Mineralogical Magazine*, vol. 55, pp. 3–18.

Şeşen, M.K. 2001. The influence of CaO on the precipitation behaviour of iron in the reduction of iron oxide. *Scandinavian Journal of Metallurgy*, vol. 30, pp. 1–7.

Shigematsu, N., Iwai, H. 1993. Effect of the Addition of SiO_2 and SiO_2–CaO on the Reduction of Dense Wüstite at High Temperatures. Tetsu-to-Hagane *(Journal of the Iron and Steel Institute of Japan)*, vol. 79, pp. 913–920.

Singh, V., Chakraborty, T., Tripathy, S.K. 2020. A Review of Low Grade Manganese Ore Upgradation Processes. *Mineral Processing and Extractive Metallurgy Review*, vol. 41, pp. 417–438.

Turkdogan, E.T., Vinters, J. V. 1973. Reducibility of iron ore pellets and effect of additions. *Canadian Metallurgical Quarterly*, vol. 12, pp. 9–21.

Wellbeloved, D.B., Craven, P.M., Waudby, J.W. 1997. Manganese and manganese alloys. In: ELVERS, B., HAWKINS, S., SCHULZ, G. (eds.) Ullman's Encyclopedia of Industrial Chemistry. New York: John Wiley & Sons.

You, Z., Li, G., Peng, Z., Zhang, Y., Qin, L., Jiang, T. 2017. Reductive roasting of iron-rich manganese oxide ore with elemental sulfur for selective manganese extraction. *Journal of Mining and Metallurgy, Section B: Metallurgy*, vol. 53, pp. 115–122.

Zhang, Y., Du, M., Liu, B., Su, Z., Li, G., Jiang, T. 2017. Separation and recovery of iron and manganese from high-iron manganese oxide ores by reduction roasting and magnetic separation technique. *Separation Science and Technology*, vol. 52, pp. 1321–1332.

Zhao, Z.L., Tang, H.Q., Guo, Z.C. 2013. Effects of CaO on precipitation morphology of metallic iron in reduction of iron oxides under CO atmosphere. *Journal of Iron and Steel Research International*, 20, 16–24.

Zhong, H., ER, D., Wen, L. 2017. Theoretical study on influence of CaO and MgO on the reduction of FeO by CO. *Applied Surface Science*, vol. 399, pp. 630–637. ◆

YPC EVENTS SERIES 2026

The role of youth and young professionals in Future Proofing African Mining, Today

BACKGROUND AROUND THE THEME

- Focus on sustainability and innovation
- Inclusivity and job creation
- Aligns to the Mining Indaba theme
- Beyond mining

THE EVENTS FOR THE MONTH:

YPC Student Debate presented by the SAIMM Johannesburg Branch: 27 August 2026, DRA Head Office, Sandton, Johannesburg.

Topic: Does mining provide additional value apart from only extracting resources within communities.

Debate Topics: Fostering innovation, infrastructure development and economic growth across various sectors.

The Johannesburg Branch in partnership with the Young Professionals Council is proud to present the Student Debate featuring The University of Johannesburg and University of the Witwatersrand.
This event will provide a stage for students from The University of Johannesburg and University of the Witwatersrand, within the minerals discipline to present compelling arguments on industry relevant themes.

Young Professionals Conference: 29-30 September 2026, Mintek, Randburg, Johannesburg

Topic: The role of youth and young professionals in Future Proofing African Mining, Today
The conference promises to be an engaging and informative event that will explore the latest trends, ideas, and innovations in the minerals industry. This conference offers young professionals the opportunity to network with peers and industry experts, establish professional relationships, and collaborate on future projects. A conference dedicated to young professionals emphasising the importance of empowering young professionals to lead the way in driving innovation and sustainability in the South African minerals industry.

Student Colloquium: 28 October 2026, Mintek, Randburg, Johannesburg.

Topic: Adapting the African Mining industry to changing global trends to ensure long term sustainability.

The Southern African Institute of Mining and Metallurgy has been organizing and presenting the annual Student Colloquium since 2002, to afford the best final-year mining and metallurgical students an opportunity to present their final year projects to an audience of mining and metallurgical industry experts.
Students are given an opportunity and platform to showcase their best research and innovation that contributes to advancing the mining and minerals industry to greater heights

FOR FURTHER INFORMATION CONTACT:
Gugu Charlie,
Conference and Events Coordinator
E-mail: gugu@saimm.co.za
Tel: +27 11 538-0238 Web: www.saimm.co.za

Dissolution of SiO_2 in SiO_2-CaO-Al_2O_3 slags

by M. B. Folstad, M. Zhu, M. Tangstad

Affiliation:
Norwegian University of Science and Technology, Trondheim, Norway

Correspondence to:
M. B. Folstad

Email:
marit.b.folstad@ntnu.no

Dates:
Received: 19 May. 2026
Published: July. 2026

How to cite:
Folstad, M. B., Zhu, M., Tangstad, M. 2026. Dissolution of SiO_2 in SiO_2-CaO-Al_2O_3 slags. *Journal of the Southern African Institute of Mining and Metallurgy*, vol. 126, no. 7, pp. 395 – 404

DOI ID:
https://doi.org/10.17159/2411-9717/1021/2026

ORCiD:
M. B. Folstad
https://orcid.org/0000-0001-6862-8425
M. Zhu
https://orcid.org/0000-0002-5758-9747
M. Tangstad
https://orcid.org/0000-0001-9751-7716

This paper is based on a presentation given at the SAIMM Pyrometallurgy International Conference 2026, 26-28 May 2026, CSIR International Convention Centre, Pretoria, South Africa

Abstract

The dissolution rate of silica (SiO_2) into different compositions of SiO_2-CaO-Al_2O_3 slags was studied at 1500° C and 1550 °C under an inert atmosphere of argon. The results show that the dissolution process is controlled by mass transfer of SiO_2 in the slag. The experimental results were used to evaluate the dissolution rate, which was found to increase with increasing CaO/$Al2O_3$ ratios as well as with increasing temperature. Boltzmann–Matano analysis was applied to obtain a profile-based effective chemical inter-diffusivity. The extracted inter-diffusivity coefficients decrease systematically with increasing SiO2 content and fall in the range of ~10^{-12} – 10^{-13} m^2/s. These low values imply intrinsically slow diffusion-controlled SiO2 enrichment, so that approaching equilibrium is unlikely within the residence time of descending materials in industrial furnaces.

Keywords

Silica dissolution kinetics, SiO_2-CaO-Al_2O_3 slag, Silicon production, Boltzmann–Matano analysis, Slag viscosity

Introduction

Metallurgical silicon (Si) is industrially produced in submerged arc furnaces through carbothermic reduction of quartz (SiO_2). The overall mass balance is written as in Reaction 1, but the actual process is more complex and happens in several steps. In addition to the charge materials, oxide impurities are present in the furnace and will react and interact with the charge.

$$SiO_{2\,(s)} + 2C_s = Si_l + 2CO_g \quad [1]$$

The amount of accumulated slag in the furnace is an important factor in deciding the productivity of the furnace, and significant variations have been observed between different furnaces during furnace excavations over the last 15 years (Jusnes, 2020; Ksiazek, 2018; Ksiazek et al., 2013; 2018; Tangstad et al., 2014; Tranell et al., 2010). Accumulated slag is typically found along the furnace walls, sometimes extending all the way up to the charge top, and at the furnace bottom. The slag is more viscous than the Si metal and more slag accumulated will therefore affect the fluid flow in the furnace. A too thick layer of accumulated slag along the furnace walls hinders the raw materials from descending and, hence, narrows the reaction route. Accumulated slag at the bottom of the furnace affects the tapping process, as it may hinder the metal flow towards the tap-hole and it can also clog to the tap-hole.

The slag in the Si furnace mainly contains SiO_2, CaO, and Al_2O_3. Figure 1 shows the phase diagram of this system. It is found that the accumulated slag in the upper parts of the furnace generally has a higher SiO_2 content compared to the slag accumulated further down in the furnace (Folstad, 2023). The viscosity of the slag has a great impact on how the materials move through the furnace. It is preferable to have a lower viscosity to ensure a good mass flow and let the raw materials react as they descend. An increasing amount of SiO_2 in the slag will increase the viscosity. The amount of SiO_2 in the slag will also affect the liquidus temperature. For slags with a high amount of CaO or $Al2O_3$, the addition of SiO_2 lowers the liquidus temperature. However, for slags with SiO_2 > 60 wt%, more SiO_2 to the system will decrease the liquidus temperature. The Si furnace is normally divided into a low temperature zone that includes the higher parts of the furnace and along the furnace walls, and a high temperature zone

in the lower parts of the furnace around the electrode tip (Schei et al., 1998). This means that the slag inside the Si furnace experiences different temperatures, depending on where it is in the furnace. Figure 2 shows an illustration of the Si furnace, including the main zones and approximate temperatures at the different positions. The temperatures are based on COMSOL simulations from Myrhaug (2020) and temperature measurements from Johansen et al. (1998), and Ksiazek et al. (2021). The highest temperatures can be found right below the electrodes around the arc. Below the cavities is the metal bath, which holds a temperature around 2000 °C. With increasing distance from the arc, towards the furnace lining and upwards, the temperature decreases. The temperature in the charge area is normally around 900 °C – 1200 °C, but during challenging conditions the temperature has been measured up to 1700 °C.

Based on these temperatures, slag is not expected to be found in the upper parts of the furnace during normal operation. However, the existence of slag higher up in the inactive zone could be explained by a high crater pressure pushing the slag from the bottom to the lining, and up towards the charge top. Kadkhodabeigi (2011) modelled the effect of the crater pressure on the melt flow pattern in the furnace bottom and found that a high crater pressure pushes the melt towards the furnace walls. This model does not include slag in the melt, which has a higher viscosity than the metal. However, the findings of slag higher up in the furnace in the inactive zone indicate a sufficient high crater pressure to move the slag in the same way as the metal to the furnace wall and upwards. The objective of this paper is to investigate the dissolution of descending quartz into accumulated SiO_2-CaO-Al2O_3 slag as a potential cause for the increased SiO_2 levels observed in the upper parts of the furnace. To evaluate this, we have investigated the dissolution rate at 1500 °C and 1550 °C for three different slag compositions relevant to silicon production.

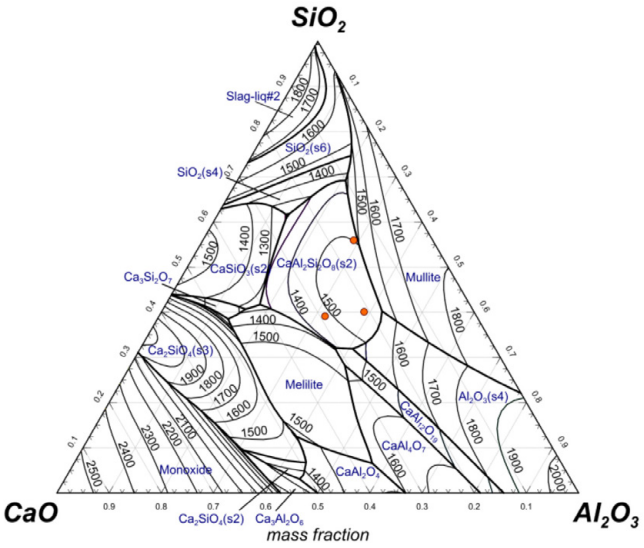

Figure 1—The SiO_2-CaO-Al_2O_3 ternary phase diagram, generated using FactSage 8.4

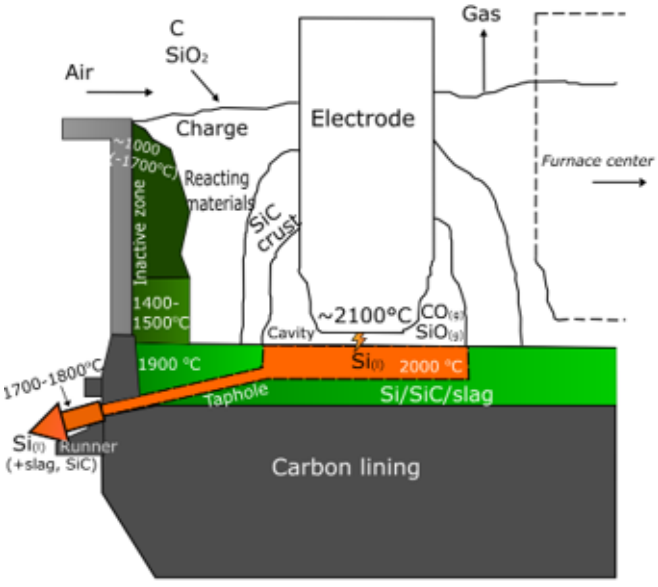

Figure 2—Illustration of a Si furnace including the main zones and approximate temperatures at different positions. The temperatures are based on modelled temperatures from Myrhaug (2020), and temperature measurements from Johansen et al. (1998) and Ksiazek et al. (2021)

Previous studies on SiO2 dissolution kinetics

The literature available on SiO_2 dissolution in SiO_2-CaO-Al_2O_3 slag relevant to Si production is limited. Most research has been carried out on the reaction related to the steel industry. Experimental studies have found that the dissolution process is controlled by diffusion in the liquid slag. Several researchers have also deduced the diffusivity from dissolution rate data (Feichtinger et al., 2014; Gou et al., 2023; Majdič, Wagner, 1965; Ren et al., 2022; Samaddar et al., 1964). A short summary of these diffusion coefficients, together with the respective slag compositions, temperatures, and viscosities, is presented in Table 1.

The first studies on the dissolution behaviour were done by dipping solid SiO_2 in slags for a fixed time. Samaddar et al. (1964) and Oishi (1965) studied the dissolution of fused silica at temperatures between 1350 °C and 1500 °C. They found that the dissolution of vitreous SiO_2 was controlled by transport within the liquid boundary layer, and that the CaO/Al_2O_3 ratio increased at the interface. The diffusion coefficients were calculated based on slag characteristics for the slag composition of 40% SiO_2 – 40% CaO – 20% Al_2O_3 and were found to be in the range of 10^{-12} m2/s.

Later studies were conducted in high-temperature confocal scanning laser microscopy (HT-CSLM). Feichtinger et al. (2014) studied the dissolution of amorphous SiO2 particles in six different compositions of SiO_2-CaO-Al_2O_3 slag with SiO_2 concentrations between 37.1% and 50.5% at 1450 °C. They found that the shape of the dissolution curves varied as a function of the slag composition. The dissolution pattern was strongly affected by slag viscosity, not by the concentration or the activity of SiO_2. Slags with higher viscosities resulted in longer dissolution times. The patterns were compared with the shrinking core model, and they showed that this model could not represent the dissolution behaviour observed in their study. The effective binary diffusion coefficient was calculated from Fick's second law of diffusion.

Ren et al., (2022) also studied the dissolution mechanism of SiO_2 in the HT-CSLM for three different slag compositions at temperatures from 1520 °C to 1580 °C. Their study confirms that the dissolution of SiO_2 inclusions is primarily controlled by mass transfer in the slag phase rather than the chemical reaction at the interface. They also found that decreasing the CaO/Al_2O_3 ratio also decreases the diffusion coefficient, and that increasing temperature increases the diffusion coefficient. From their results, the dissolution rate is affected by both the concentration gradient and the interface area. Gou et al., (2023) studied the dissolution of SiO_2 inclusions

with varied size using the CSLM and found that with increasing initial size of SiO_2 inclusions increased the dissolution time in a low silica slag with composition 8.3% SiO_2 – 50% CaO – 41.7% Al_2O_3 at 1500 °C. Both Ren et al., and Gou et al., found a linear relationship between the dissolution rate and a ratio of concentration difference and slag viscosity ($\Delta C/\eta$). This linear correlation suggests that viscosity is the dominant factor in the dissolution kinetics.

Kristiansen (2022; 2023) studied the dissolution rate of industrial quartz into three compositions of SiO_2-CaO-Al_2O_3 slags relevant for the Si production. His research indicated that the dissolution was controlled by the chemical reaction and that the dissolution was driven by the basicity of the slag, isothermal holding time, and the interface area of the liquid slag. He found the activation energy for two slags of 50% SiO_2 - 21% CaO – 29% Al_2O_3, and 62% SiO_2 - 20% CaO – 18% Al_2O_3 to be 119.9 kJ/mol and 83.7 kJ/mol, respectively.

Materials, equipment and methods

Based on slag compositions found in accumulated slag samples in industrial Si furnaces (Folstad, Tangstad, 2021; Jusnes et al., 2021), we utilised three different SiO_2-CaO-Al_2O_3 slag compositions with two different CaO/Al_2O_3 ratios. We melted mixtures of SiO_2, limestone ($CaCO_3$) and Al_2O_3 powder in an induction furnace. Table 2 presents the purity of the powders and the suppliers. To ensure a homogenous slag phase, we remelted the mixtures three times at temperatures up to 1800 °C, which is significantly above the expected liquidus temperatures for the different slag compositions. Table 3 lists the compositions of all three slags, their respective liquidus temperatures T_{liq}, and their viscosities η at 1500 °C and 155 °C. The compositions are plotted in the ternary phase diagram in Figure 1.

For the dissolution experiments, we used SiO_2 substrates with a 10 mm diameter and 3 mm height. To prevent the slag from spreading during the heating experiments, we coated the edges of the substrates with a thin layer of boron nitrate. The preparation involved pressing 0.6 g of slag powder into pellets, which were then placed on top of the SiO_2 substrates. We conducted the dissolution experiments in a sessile drop furnace, heating the samples up to 1500 °C or 1550 °C at a rate of 50 °C/min. This temperature exceeds the liquidus temperature for Slag 1 and 3. Isothermal holding times varied from 0 to 60 minutes, where 0 minutes indicate no isothermal holding time. The sessile drop furnace utilises graphite heating elements, and a B-type thermocouple measures the temperature. Figure 3 shows the SiO_2 and slag before the experiment, and the slag after experiment.

We used an EPMA, JEOL JXA 8500 to investigate the SiO_2 and slag after the sessile drop furnace experiments. After the furnace runs, we mounted the samples in epoxy and then prepared a vertical cross section in the centre of each sample. We imaged the cross sections with EPMA and determined the oxide compositions via a wavelength-dispersive X-ray spectrometer (WDS) to quantify the different elements in the samples.

Table 1
Summary of earlier research on the dissolution of SiO_2 in SiO2-CaO-Al2O3 slag. D is the diffusion coefficient and η is the viscosity.

Author	Slag composition			T [°C]	D [m^2/s]	Viscosi-ty [cP]	Comment
	SiO_2	CaO	Al_2O_3				
Samaddar et *al.*, (1964).	40	40	20	1350	$1.8\cdot10^{-12}$	2311	Forced convection.
				1390	$3.2\cdot10^{-12}$	1652	
				1425	$4.5\cdot10^{-12}$	1251	
				1500	$6.5\cdot10^{-12}$	720	
Majdič and Wagner (1970),	45	38.5	16.5	1500	$2.8\cdot10^{-10}$	896	D calculated with Fick's second law of diffusion.
Feichtinger et al., (2014).	54.6	34.1	10.6	1450	$4.4\cdot10^{-11}$	2410	
	50.5	38.3	10.6		$8.5\cdot10^{-11}$	1250	
	45.3	43.7	10.4		$1.8\cdot10^{-10}$	1080	
	42.8	46.6	10.8		$2.4\cdot10^{-10}$	1020	
	37.1	36.4	26.5		$3.8\cdot10^{-11}$	600	
	42.3	38.8	18.9		$6.0\cdot10^{-11}$	470	
Ren et al., (2023).	48.4	43.6	5.0*	1520	$3.3\cdot10^{-10}$	305	* +3.0% MgO.
				1550	$3.9\cdot10^{-10}$	258	
				1580	$4.0\cdot10^{-10}$	219	D calculated from modified version of the rate equation for mass-transport-controlled dissolution.
	45.8	41.2	10.0*	1520	$2.0\cdot10^{-10}$	356	
				1550	$2.3\cdot10^{-10}$	299	
				1580	$2.1\cdot10^{-10}$	252	
		38.8	15.0*	1520	$1.4\cdot10^{-10}$	428	
	43.2			1550	$1.5\cdot10^{-10}$	356	
				1580	$1.3\cdot10^{-10}$	298	

Table 2

The raw materials used in Slag 1-3 for the dissolution experiment

Product	Supplier	Purity
SiO_2	ThermoFisher Scientific (2024)	>99.9%
Limestone ($CaCO_3$)	FranzeFoss Minerals AS (2024)	>99.7%
Al_2O_3	ThermoFisher Scientific (2024)	>99.9%

Table 3

SiO_2- CaO-Al_2O_3 slags used in the dissolution experiments. Compositions are given in wt%; liquidus temperatures (Tliq) and viscosities for the slags are calculated using FactSage 8.4

	SiO_2	CaO	Al_2O_3	C/A	Tliq	Viscosities [cP]	
					[°C]	1500 °C	1550 °C
Slag 1	56	15	29	½	1497	45 636	25 012
Slag 2	40	21	39	½	1552	8753	5118
Slag 3	39	29	32	1	1467	3083	2975

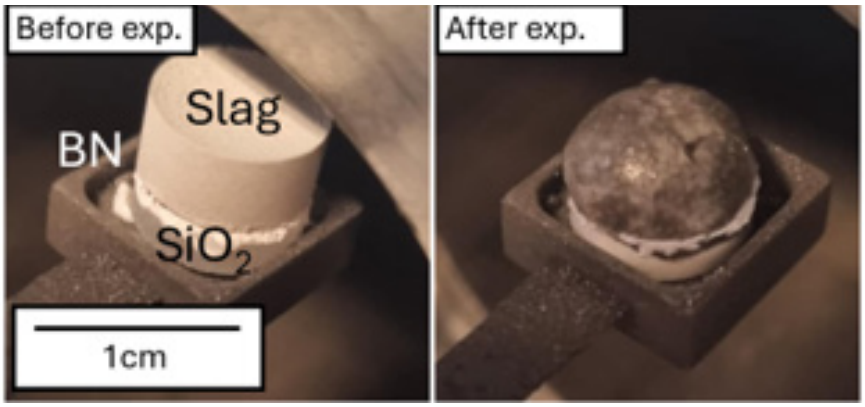

Figure 3—Slag and SiO2 before sessile drop experiment and slag after dissolution experiment

Results and discussion

This chapter presents the experimental findings on the dissolution of SiO_2 in SiO_2-CaO-Al_2O_3 slags and discusses their implications for industrial furnace operations. The first section evaluates the concentration profiles obtained via EPMA-WDS to verify if the transport is diffusion-controlled. Subsequently, Boltzmann-Matano analysis is used to quantify the concentration-dependent diffusivity and the activation energy of the process. Finally, these kinetic data are linked to slag viscosity and residence time to explain the accumulation of SiO_2-rich slag in the inactive zones of the furnace.

Figure 4 presents cross-sectional images of four dissolution experiments with the SiO_2 and Slag 1 after isothermal holding times ranging from 0 to 60 minutes at 1500 °C. The SiO_2 concentration in the slag was measured in the slag phase using EPMA-WDS analysis, starting from the SiO_2 interface and extending 140 µm into the bulk slag. The resulting concentration profiles are shown in Figure 5 as a function of distance from the interface. Beyond this distance, the slag composition remained equal to the initial concentration. One curve is shown in light grey. This represents Slag 1 with a 30-minute isothermal holding time and is considered an outlier. These graphs show a distinct concentration gradient near the interface, and the SiO_2-rich zone extends progressively further into the slag with time while approaching a far-field plateau. This behaviour is consistent with the growth of a transport boundary layer and suggests diffusion-dominated dissolution in the early stages. This is consistent with earlier research (Feichtinger et al., 2014; Gou et al., (2023); Majdič, Wagner, 1970; Oishi et al., 1965; Ren et al., 2022; Samaddar et al., 1964). Several of the concentration profiles in Figure 4 do not converge towards the initial bulk concentration of the slag. This is because the slag solidified into two distinct phases during cooling, as can be observed in the cross-sectional images. To account for this phase separation in the calculations, an average concentration was utilised. By applying this average concentration, the measured values converge towards the initial bulk concentration of the slag.

By fitting the dissolution profile, it was found that a constant-diffusivity assumption can only reproduce the near-interface region within the first 20 µm, but it systematically underestimates the concentration penetration at larger distances. This indicates that the mass transfer varies strongly with local SiO_2 content, implying a strongly composition-dependent effective diffusivity that is

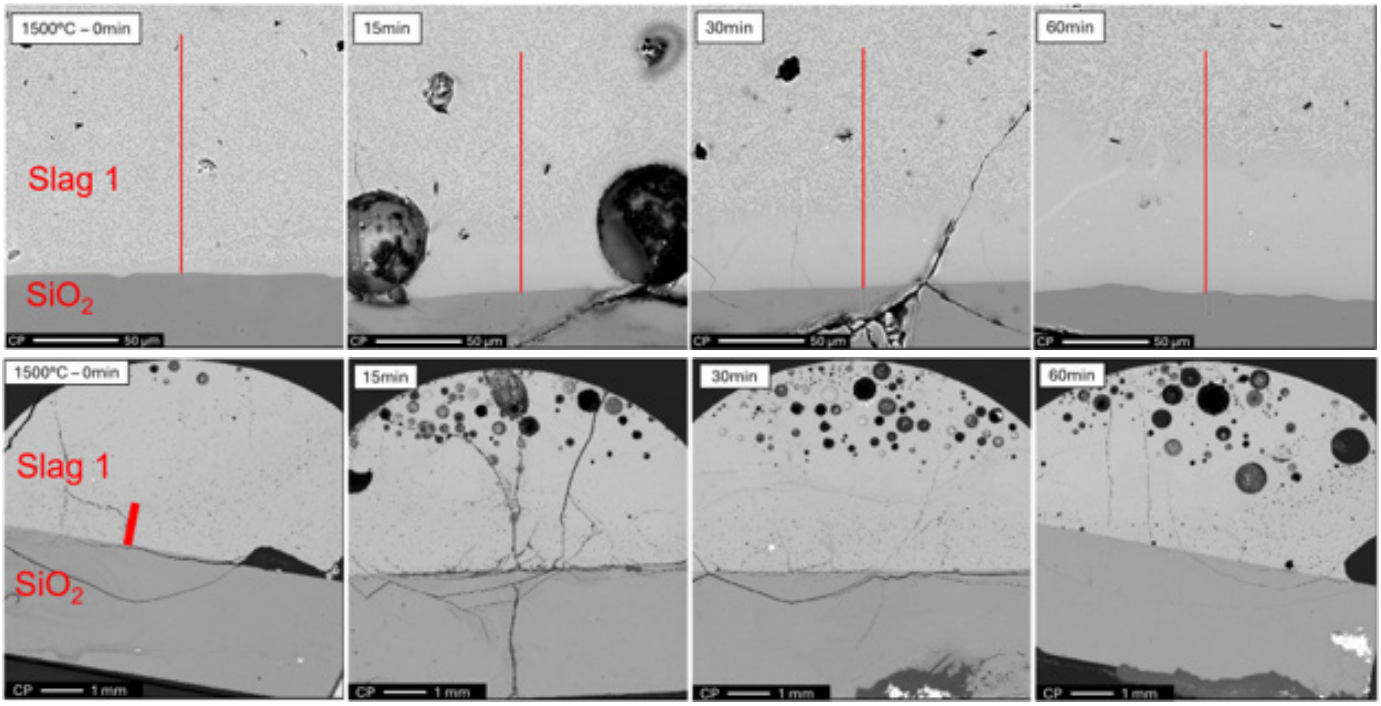

Figure 4—Cross-section images of SiO2 and Slag 1 captured with EPMA after different holding times from 0-60 minutes at 1500 °C

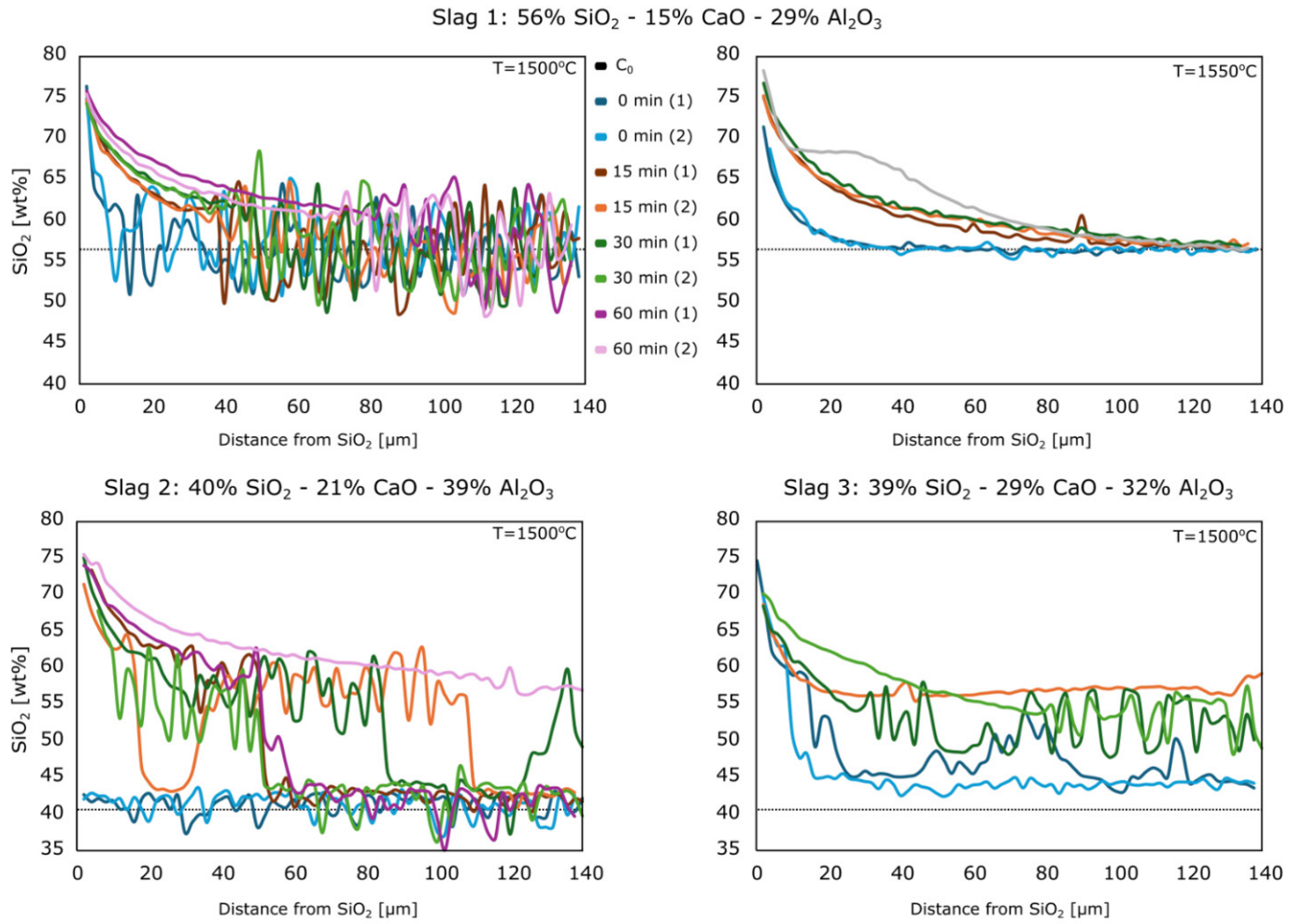

Figure 5— The experimental results given as SiO_2 concentration as a function of the distance from the SiO_2 interphase of the vertical cross sections. The SiO_2 concentration was measured in the slag phase using EPMA-WDS analysis. One curve is shown in light grey. This represents Slag 1 with a 30-minute isothermal holding time and is considered an outlier

consistent with higher values at lower SiO_2 contents. To quantify this composition dependence from the measured concentration profiles, Boltzmann–Matano (B–M) analysis was employed to invert the experimental C(x,t)-data and extract an effective concentration-dependent diffusivity $\tilde{D}(C)$ (Heo, Park, 2022).

The B–M approach assumes a diffusion-dominated, self-similar concentration field, such that the concentration profiles measured at different times should have the same shape when plotted against the scaled coordinate η, from Equation 2 (Crank, 1979). If diffusion is the dominant transport mechanism, the data curves from different time intervals should collapse onto a single 'master curve' in η-space; therefore we first perform a Boltzmann collapse test to verify this self-similarity assumption and to identify the time and composition ranges over which B–M inversion is applicable.

$$\eta_{BM} = \frac{x}{\sqrt{t}} \quad [2]$$

Where η is a time-independent position variable, x is the distance from the interface and t is the time.

Figure 6 shows the B-M screening results for the SiO_2 dissolution profiles, including the raw concentration profiles and the corresponding Boltzmann-scaled plots (C vs. $\eta_{BM}=x/\sqrt{t}$) used to assess self-similarity.

The analysis shows that the curves from Slag 1 at both 1500 °C and 1550 °C exhibit a strong collapse. This behaviour is consistent with diffusion being the main driver near the interface and supports the applicability of B-M analysis for determining the concentration-dependent diffusivity $\tilde{D}(C)$ for this composition. Similarly, the curves for Slag 3 collapse reasonably well near the interface for two profiles, making a diffusion-controlled mechanism plausible, albeit with caution. Slag 2 collapses poorly. This poor fit suggests that Slag 2 is unique and that additional process, such as convection or phase-related effects, may contribute. This slag has a higher liquidus temperature compared to Slag 1 and 3, and is most likely only partly melted at the experimental temperature of 1500 °C. Because B-M analysis assumes a homogeneous slag phase, it cannot accurately be applied to Slag 2, indicating that the dissolution mechanism for this composition is different.

Figure 7 shows the concentration-dependent effective diffusivity extracted from the SiO_2 dissolution profiles of Slag 1 and Slag 3 using B–M inversion, reported as the median with an interquartile range band across the available profiles. For all conditions, $\tilde{D}(C)$ decreases systematically with increasing SiO_2 content, with values spanning roughly from 10–12 to 10^{-13} m^2/s over the composition intervals around 65 wt% SiO_2. This strong composition dependence is consistent with the expectation that SiO_2-enrichment increases melt polymerisation and viscosity, thereby reducing species mobility. Furthermore, the diffusivity of Slag 1 increases as the temperature increases from 1500 °C to 1550 °C.

Compared with literature values reported for lower-viscosity slags from Feichtinger et al. (2014) and Ren et al. (2022), who reported values in the range of 10^{-10} - 10^{-11} m^2/s for temperatures between 1450 °C and 1580 °C, the diffusivities obtained here are lower. However, it is worth noting that the quantities are not directly comparable because the reported values are typically inferred from mass-transfer models and should be regarded as effective transport parameters. As such, they can embed assumptions about boundary-layer thickness and may implicitly include convection-enhanced mass transfer rather than representing purely diffusive transport. In contrast, the diffusivities reported in this work are profile-based effective chemical inter-diffusivities obtained from B-M analysis. They quantify the rate at which the concentration field evolves within the near-interface boundary layer along the experimental composition path under diffusion-dominated conditions. Despite these differences, the trends are qualitatively consistent with

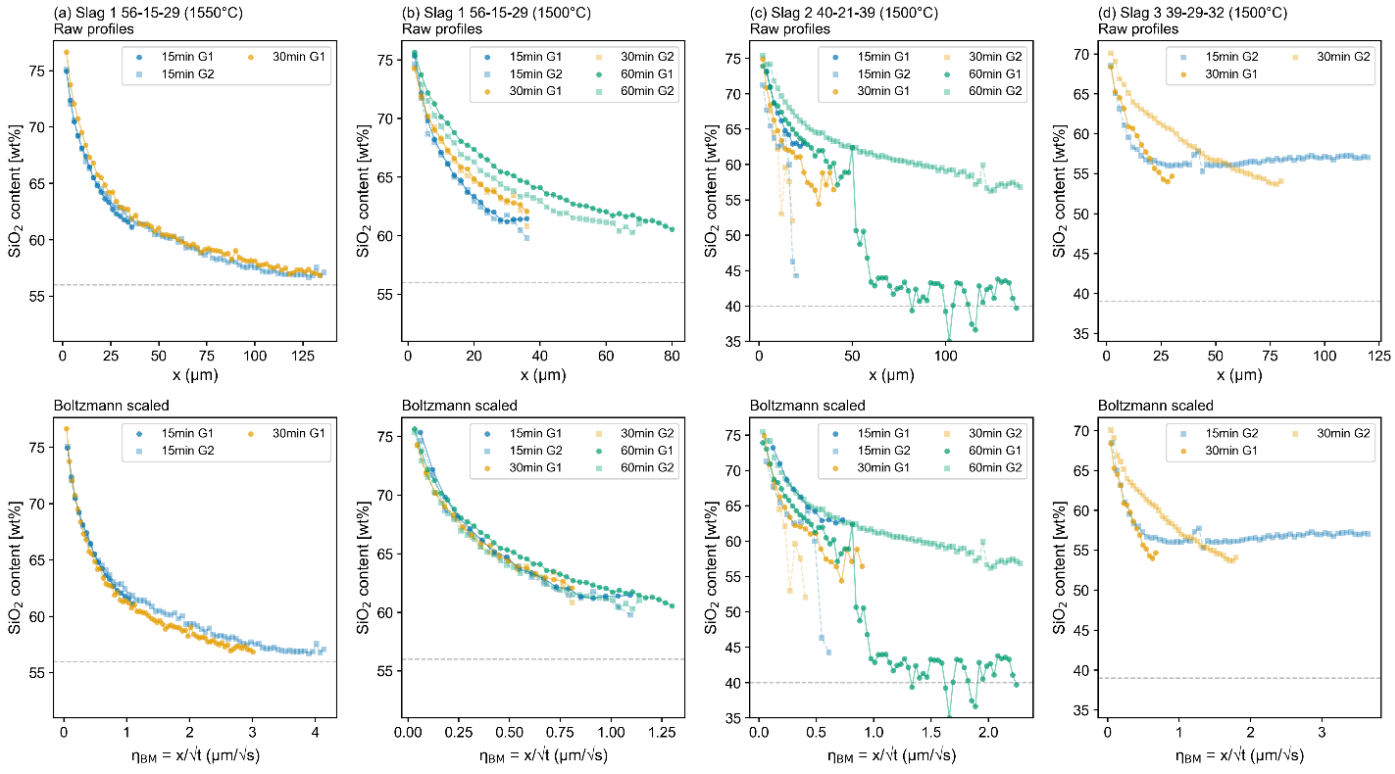

Figure 6— The Boltzmann–Matano screening summary for SiO2 dissolution profiles in studied slag

viscosity-controlled dissolution kinetics, in which higher-viscosity melts exhibit reduced mobility and lower effective transport coefficients.

Figure 8 shows the obtained apparent activation energy variation for Slag 1, where the viscous flow activation energy was obtained using the Zhang–Chou viscosity model (Zhang et al., 2014). It can be seen that both the apparent activation energy of the profile-based chemical inter-diffusivity and the activation energy of viscous flow decrease as SiO_2 content decreases. In addition, inter-diffusion values appear to drop more rapidly, suggesting that the two trends may converge and potentially cross in the low-SiO_2 region. It is also seen that the inter-diffusion activation energies remain systematically higher than those associated with viscous flow over the calculated composition range. Although experimental uncertainty cannot be excluded given the two-temperature estimate and the sensitivity of B–M inversion, the overall trend is still physically plausible. The reason is that the extracted effective chemical inter-diffusivity can reflect both kinetic mobility, which is strongly controlled by melt structure and viscosity, and thermodynamic driving-force contributions. As a result, its temperature dependence can be stronger than that of viscous flow alone, because changes in temperature affect not only the mobility of species in the melt but also the chemical-potential gradients that drive the re-establishment of chemical equilibrium along the composition path.

The temporal evolution of the SiO_2 concentration field was modelled for Slag 1. Figure 9 shows the predicted SiO_2 concentration profiles as a function of distance from the SiO_2/slag interface at increasing times. The results indicate that SiO_2 dissolution into the SiO_2-CaO-Al_2O_3 slag system is a relatively slow process. When considering the industrial silicon production process, the residence time of raw materials within the furnace must be considered. Given the low diffusion coefficients obtained in this study, in the order of 10^{-12} m^2/s – 10^{-13} m^2/s, diffusion-controlled equilibration is inherently slow. While industrial convection and mixing can accelerate mass transfer, day-scale contact times are still likely required to approach full equilibrium with quartz at 1500 °C, particularly in weakly mixed or stagnant regions.

Considering these slow rates, it is unlikely that descending slags have sufficient time to reach SiO_2 concentration of 70% – 80% purely through dissolution in the furnace. However, accumulated slag is likely to remain for a significantly longer duration. As quartz is continuously fed from the top of the furnace, the accumulated slags will have prolonged access to SiO_2. Under the assumption that the slag remains in inactive zones, it will gradually dissolve more SiO_2 until it reaches higher concentrations. Furthermore, as viscosity increases with both decreasing temperature and increasing SiO_2 content, the slag becomes more resistant to flow and is then more likely to accumulate.

Varying amounts of SiO_2 in the slag affects its physical properties and, hence, also its behaviour within the furnace. Viscosity is one of the most critical factors influencing the slag flow through the furnace. It is preferable with sufficient low viscosity to ensure a good mass transport. It is found that the accumulated slag in the upper parts of the furnace generally has a higher SiO_2 content compared to the slag found further down, while the CaO/Al_2O_3 ratio is relatively constant within the same furnace (Folstad, 2023). Slag in the inactive zone typically contains > 50% SiO_2, whereas the SiO_2 content at the furnace bottom generally is generally < 50%. Figure 10 displays the slag viscosity on a logarithmic scale as a function of increasing SiO_2 content for a fixed CaO/Al_2O_3 ratio of 0.5. The corresponding compositions are indicated by the arrow in the SiO_2-CaO-Al_2O_3-phase diagram in the same figure. The viscosity curves from 1500 °C – 2000 °C show that the viscosity increases significantly with higher SiO_2 concentrations. This trend becomes even more pronounced with higher SiO_2 concentrations. Furthermore, because the liquidus temperatures are often higher than the actual expected temperatures in that area, the slag system may be only partly liquid. This partial solidification further increases the effective viscosity.

These data also indicate that the impact of SiO_2 concentration on viscosity is in the same size range as a temperature change of 500 °C. Since the slag in inactive zone of the furnace typically ranges from 50 – 80 wt%, the viscosities at 1500 °C will vary from approximately 25 000 cP – 1 000 000 cP – ranging from the consistency of ketchup to the glass 'working point'. With both higher SiO_2 content and lower temperatures, compared to the furnace bottom, the slag in the inactive zone becomes more viscous. This higher viscosity makes the slag more resistant to flow and more likely to accumulate, which is negative for the furnace operation.

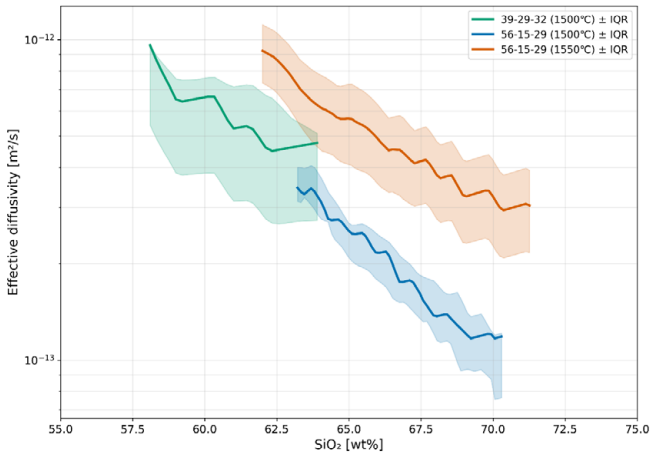

Figure 7—The concentration-dependent diffusivity for Slag 1 and 3 calculated using Boltzmann-Matano inversion of EPMA concentration profiles. Solid lines show the median concentration-dependent diffusivity D(C), and shaded bands indicate the interquartile range across profiles

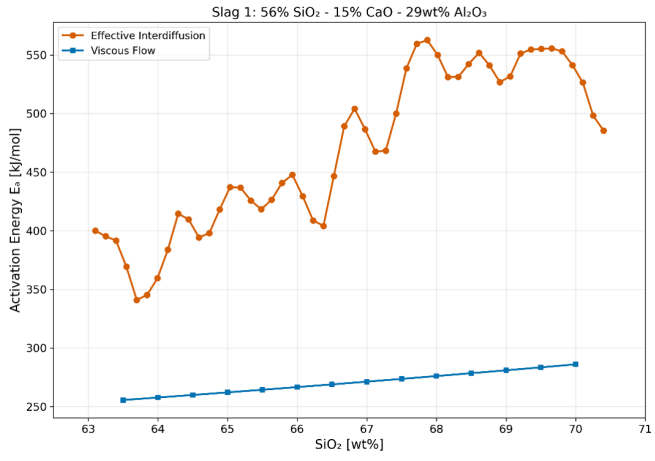

Figure 8—Apparent activation energy for the profile-based effective chemical inter-diffusion compared with the activation energy of viscous flow at the same SiO2 content

Dissolution of SiO_2 in SiO_2-CaO-Al_2O_3 slags

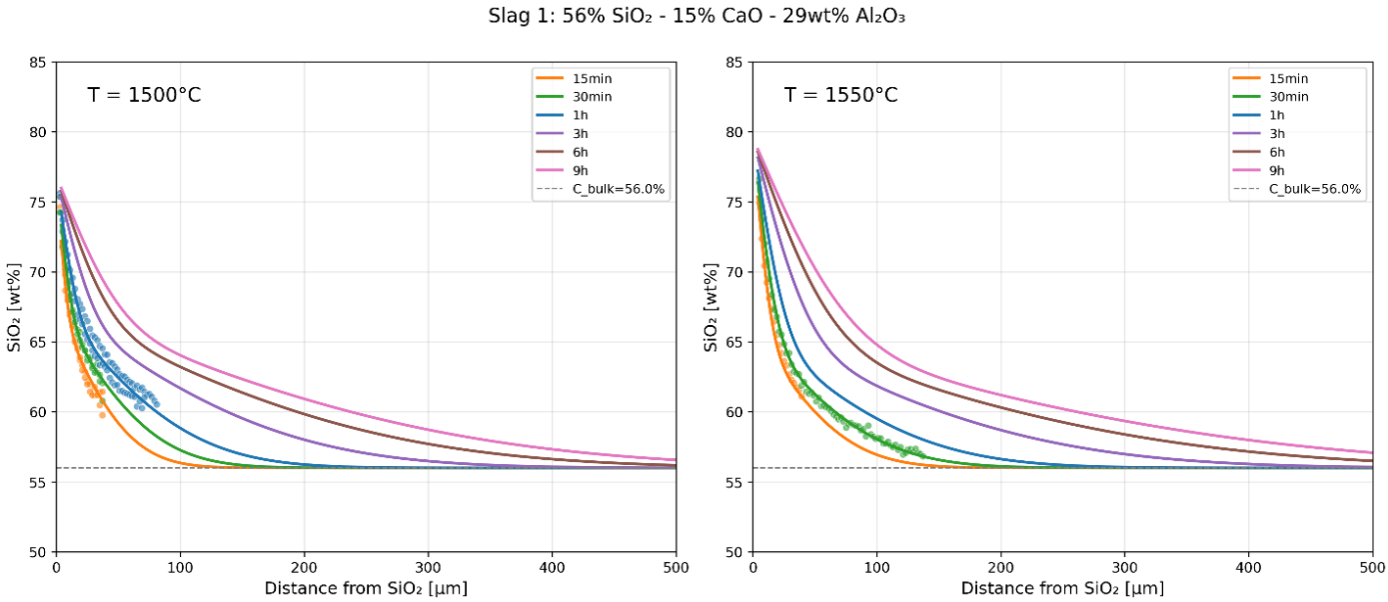

Figure 9—Estimated temporal evolution of SiO2 dissolution into Slag 1

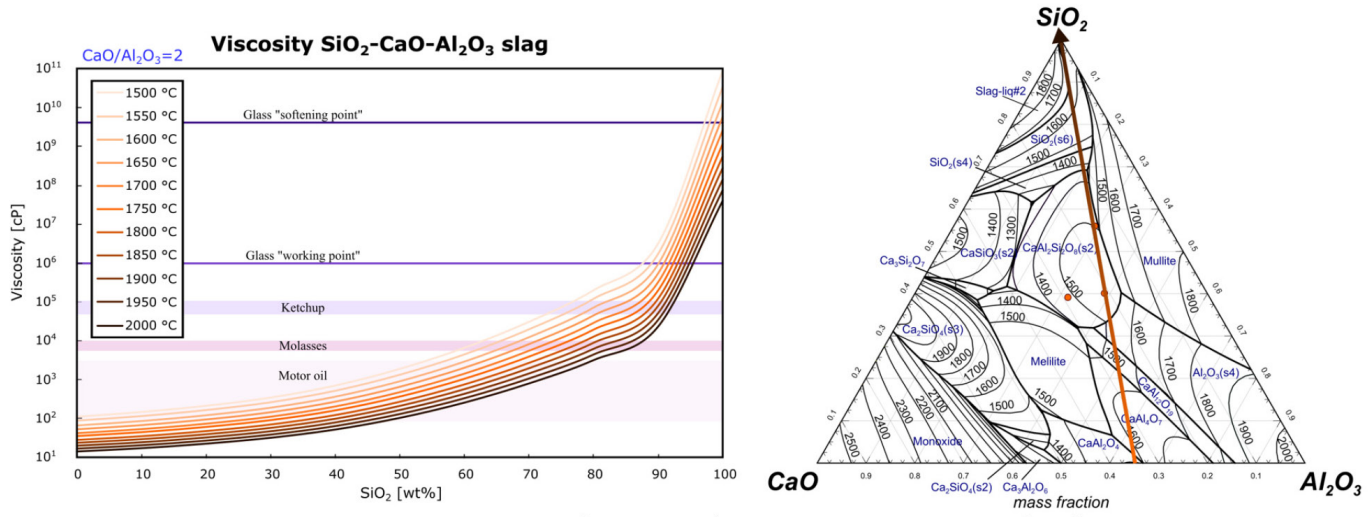

Figure 10—Viscosity as a function of SiO2 concentration in the slag

Conclusions

This study investigated the SiO_2 dissolution into different three SiO_2-CaO-Al_2O_3 slag compositions relevant for Si production. The measured profiles exhibit a growing near-interface SiO_2-enriched boundary layer and a stable far-field plateau, consistent with diffusion-dominated concentration-field evolution over the investigated length scale. Boltzmann self-similarity screening supports the use of B–M inversion to extract a profile-based effective chemical inter-diffusivity, which decreases systematically with increasing SiO_2 content and falls on the order of ~10^{-12} m^2/s – 10^{-13} m^2/s over the resolved composition range, with higher values at higher temperature. The interdiffusion activation-energy trends suggest that, in the SiO_2-rich region, thermodynamic driving-force contributions may play an important role. The low diffusivities imply intrinsically slow diffusion-controlled enrichment, making it unlikely that descending slags reach equilibrium within typical furnace residence times.

Acknowledgements

The authors would like to thank The Norwegian Ferroalloy Research Association (FFF) and the Norwegian Research Council (NRC) for their financial support through the KBN project Recursive, project no 326581.

References

Crank, J. 1979. The Mathematics of Diffusion, 2nd edn. Oxford University Press, Oxford.

Feichtinger, S., Michelic, S.K., Kang, Y.–B., Bernhard, C. 2014. In Situ Observation of the Dissolution of SiO_2 Particles in CaO-Al_2O_3-SiO_2 Slags and Mathematical Analysis of its Dissolution Pattern. *Journal of the American Ceramic Society*, vol. 97, no.1, pp.316–325.

Folstad, M.B. 2023. Slag and its effect on Si and FeSi production. PhD Thesis, Norwegian University of Science and Technology, Trondheim.

Folstad, M.B., Tangstad, M. 2021. SiO_2-CaO-Al_2O_3 slags in the Si/FeSi furnaces. Proceedings of INFACON XVI. *The Southern African Institute of Mining and Metallurgy*. Trondheim.

Franzefoss Minerals AS. 2024. https://kalk.no/en/ (accessed on 8.1.24).

Gou, L., Liu, H., Ren, Y., Zhang, L. 2023. Concept of Inclusion Capacity of Slag and Its Application on the Dissolution of Al_2O_3, ZrO_2 and SiO_2 Inclusions in CaO–Al_2O_3–SiO_2 Slag. *Metallurgical and Materials Transactions B*, vol. 54B, no.3, pp.1314–1325.

Heo, J., Park, J.H. 2022. Effect of temperature on the slag/refractory interfacial reaction with directed reduced iron (DRI) addition in an electric arc furnace (EAF) process: Diffusional growth of magnesiowüstite layer by Boltzmann-Matano analysis. *Ceramics International*, vol. 48, no. 12, pp. 17217-17224.

Johansen, S.T., Tveit, H., Grådahl, S., Valderhaug, A., Byberg, J.Å. 1998. Environmental aspects of Ferro-Silicon furnace operations - an investigation of waste gas dynamics. *Proceedings of INFACON VIII. Beijing, China*.

Jusnes, K.F. 2020. Phase transformations and thermal degradation in industrial quartz. *PhD Thesis*, *Norwegian University of Science and Technology*, Trondheim.

Jusnes, K.F., Hjelmseth, R., Folstad, M.B., Ditlefsen, N.S., Tangstad, M. 2021. Investigation of slag compositions and possible relation to furnace operation of a FeSi75 furnace. Proceedings of INFACON XVI. *The Southern African Institute of Mining and Metallurgy*. Trondheim.

Kadkhodabeigi, M. 2011. Modeling of Tapping Processes in Submerged Arc Furnaces. *PhD Thesis*, Norwegian *University of Science and Technology*, Trondheim.

Kristiansen, S. 2022. Dissolution rate and wettability of SiO_2–CaO–Al_2O_3 slag on quartz. *Project work*, *Norwegian University of Science and Technology*, Trondheim.

Kristiansen, S. 2023. Dissolution Rate and Wettability of SiO_2-CaO-Al_2O_3 Slags on Quartz. *Master Thesis*, *Norwegian University of Science and Technology*, Trondheim.

Ksiazek, M. 2018. Report: Excavation of Si furnace at Elkem Salten. Report No. 2018:00692. SINTEF, Trondheim.

Ksiazek, M., Saadieh, R., Gaertner, H., Grådahl, S., Sægrov, B., Tangstad, M., Valderhaug, A., Ringdalen, E. 2021. Industrial measurements of the gas and temperature in Si and FeSi production process. Proceedings of INFACON XVI. *The Southern African Institute of Mining and Metallurgy*. Trondheim.

Ksiazek, M., Tangstad, M., Ringdalen, E. 2013. Five furnaces five different stories. *Silicon for the Chemical and Solar Industry XIII*. pp. 33–42.

Ksiazek, M., Tangstad, M., Ringdalen, E. 2018. The rapid Si-furnace excavation - an unique chance to investigate the interior of the furnace. Proceedings of INFACON XV. Cape Town.

Majdič, A. and Wagner, H. 1970. Diffusion of Silicon in Molten Lime-Silica-Alumina Slags. Archiv für das Eisenhüttenwesen, vol. 41 no. 6, pp. 529–532.

Myrhaug, E. 2020. KPN CONTROLLED TAPPING, Examples of conceptual models based on simplified COMSOL simulations. Industrial presentation from Elkem ASA, KPN Controlled Tapping Meeting 2020.03.05.

Oishi, Y., Cooper Jr., A.R., Kingery, W.D. 1965. Dissolution in Ceramic Systems: III, Boundary Layer Concentration Gradients. *Journal of the American Ceramic Society*, vol. 48, no.2, pp 88–95.

Ren, Y., Zhu, P., Ren, C., Liu, N. and Zhang, L. 2023. Dissolution of SiO2 Inclusions in CaO-SiO2-Based Slags In Situ Observed Using High-Temperature Confocal Scanning Laser Microscopy. *Metallurgical and Materials Transactions* B, vol. 53 no. 2, pp. 682–692.

Samaddar, B.N., Kingery, W.D., Cooper Jr., A.R. 1964. Dissolution in Ceramic Systems: II, Dissolution of Aluminu, Mullite, Anorthite, and Silica in a Calcium-Aluminum-Silicate Slag. *Journal of the American Ceramic Society*, vol. 47 no. 5, pp. 249–254.

Schei, A., Tuset, J.Kr., Tveit, H. 1998. Production of High Silicon Alloy. Tapir, Trondheim.Tangstad, M., Ksiazek, M., Andersen, J.E. 2014. Zones and Materials in the Si Furnace. Silicon for the Chemical and Solar Industry XII. Trondheim, Norway.

ThermoFisher Scientific. 2024. https://www.thermofisher.com/no/en/home.html (accessed on 8.1.24.

Tranell, G., Andersson, M., Ringdalen, E., Ostrovski, O., Steinmo, J.J. 2010. Reaction zones in a FeSi75 furnace – results from an industrial excavation. *Proceedings of INFACON XI*I. Helsinki. pp. 709–715.

Zhang, Guo-Hua, Kuo-Chih Chou, and Ken Mills. "A structurally based viscosity model for oxide melts." *Metallurgical and Materials Transactions B* 45.2 (2014): pp. 698-706. ◆

Reduced order model for isothermal pre-reduction of chromite pellets with hydrogen

by M. Khama[1], Q.G. Reynolds[1,2], B.S. Xakalashe[1]

Affiliation:
[1] Mintek, South Africa
[2] University of Stellenbosch, South Africa

Correspondence to:
M. Khama

Email:
mopelik@mintek.co.za

Dates:
Received: 19 May. 2026
Published: July. 2026

How to cite:
Khama M., Reynolds Q.G., Xakalashe B.S. 2026. Reduced order model for isothermal pre-reduction of chromite pellets with hydrogen. *Journal of the Southern African Institute of Mining and Metallurgy*, vol. 126, no. 7, pp. 405 – 410

DOI ID:
https://doi.org/10.17159/2411-9717/1022/2026

ORCiD:
M. Khama
https://orcid.org/0000-0003-1443-6262
Q.G. Reynolds
https://orcid.org/0000-0002-5196-8586
B.S. Xakalashe
https://orcid.org/0000-0003-0069-7082

This paper is based on a presentation given at the SAIMM Pyrometallurgy International Conference 2026, 26-28 May 2026, CSIR International Convention Centre, Pretoria, South Africa

Abstract

Pre-reducing chromite with hydrogen offers significant benefits, including reduced energy consumption in downstream smelting and lower carbon dioxide emissions. To leverage these advantages, it is essential to develop computational models that facilitate the design, optimisation, and control of the process. Full scale models such as 3D computational fluid dynamics models are often used to investigate the multi-scale flow physics in heterogeneous reactors. However, these models impose prohibitive computational expense in the modelling of heterogeneous reacting flow systems. The high computational expense prevents the use of high dimensional systems in real time control and online optimisation of reacting flow systems. In order to facilitate incorporation of predictive models in the heterogenous reacting flow systems control loop, computationally efficient reduced order models are required. Owing to these requirements, a reduced order model for pre-reduction of chromite with hydrogen was developed with the view to rapidly predict the performance indicators for pre-reduction of chromite with hydrogen. The Thiele modulus method was used to develop the reduced order model, and the model results were compared to isothermal pre-reduction experimental results at a range of pre-reduction temperatures from 1200 oC to 1400 oC. The model predicts the degree of reduction, diffusion of gases through the product layer, unreacted core radius of the grain radius, and local and global conversion. The final conversion across all temperatures as predicted by the reduced order model deviate from the experimentally calculated conversion by a maximum relative error of 2.7% while the initial conversions differ significantly, reaching a maximum error of 65%.

Keywords

Pre-reduction, hydrogen, chromite, reduced order model

Introduction

Design and optimisation of pyrometallurgical processes is supported by computation and simulations. These processes are characterised by high energy requirements and high greenhouse gas emissions. In an effort to develop sustainable pyrometallurgical processes, pre-reduction prior to smelting is one of the solution strategies employed to reduce energy consumption and greenhouse gas emissions. To leverage the benefits pre-reduction presents to the downstream smelting process, it is crucial to characterise several performance indicators of pre-reduction reactors to gauge the optimum operating conditions. However, the performance of heterogeneous reactions at high temperatures is difficult to measure during operation (Hamadeh et al., 2018). This shortcoming is addressed by using CFD models, which can predict the dynamic features of pre-reduction reactors. In order for CFD model predictions to be considered viable, they should couple reaction kinetics (with detailed reaction mechanisms) with transport phenomenon, flow field, reactor configuration, particle size and shape, etc. The underlying physics is complex, and this, coupled with longer temporal and spatial scales including non-linearity in the governing equations imposes significant computational expense in CFD modelling of pre-reduction processes. Therefore, CFD models cannot be used for real-time control due to prohibitive computational cost.

In order to capture dynamic features of this system, a mathematical model must relate the chemical kinetics and physical properties of the grain with local temperature and pressure. In addition, it should characterise mass transfer at the grain surface and heat and mass transfer in the porous bed. Lu et al. (1996) adopted a two-scale modelling approach to develop a phenomenological model that describes reactions in a fixed bed reactor. They considered modelling at microscopic level (grain level) and macroscopic level (pellet level). At the microscopic level, the chemical kinetic equations at the grain

level are determined and at the macroscopic level, the global rate of reaction is determined by coupling heat and mass transfer with chemical kinetics from microscopic level.

There are several approaches adopted when modelling pre-reduction in a pellet by gaseous reductants and they include one interface shrinking core, three interface shrinking core, and a grain model. The one interface shrinking core model is a simplified model applicable only to dense pellets undergoing a one-step reaction and cannot be used for porous pellets where chemical reactions and diffusion happen simultaneously (Ghadi et al., 2020). On the other hand, the three interface shrinking core model uses succession of moving fronts to model the successive reactions. A grain model considers a pellet to be made of uniformly-sized nonporous grains and the reactions in each grain follow a microscopic chemical reaction-controlled shrinking core route and this approach is appropriate for gas-solid reactions in porous pellets.

The modelling of hydrogen (H_2) reduction consists of either faster/slower transport phenomena and slow/faster chemical reactions and often requires using small time steps to resolve both the faster and slower processes, and this results in prohibitive computational expense. One approach to address the high computational expense is using an effectiveness factor approach, which can capture the essential physics yet remain computationally efficient. The effectiveness factor is defined in Equation 1, and it is evident from the equation that this approach defines the competition between reaction and diffusion. At steady state conditions, the effectiveness factor can be calculated by considering that the rate of external mass transfer from the bulk fluid to the surface is equal to the overall reaction rate.

$$\eta = \frac{Actual\ reaction\ rate}{Reaction\ rate\ if\ entire\ pellet\ interior\ were\ exposed\ to\ bulk\ gas\ condition} \quad [1]$$

The objective of the study is to develop a reduced order model (ROM) to allow for rapid evaluation of performance behaviour of pre-reduction of chromite pellets with H_2. A validated and verified ROM will be used in real time control and online optimisation of reacting flow systems.

Model development

An approach for developing ROMs for gas-solid reactions by Wang et al. (2021) was used in the current study, as demonstrated by Equations 4 to 17. The assumptions made when developing a ROM are that there is a uniform temperature distribution at the grain level, porosity remains constant, and spherical grains maintain sphericity during the reaction. A picture depicting pellet and grain level scales and growth of product islands on the grain surface is shown in Figure 1. As opposed to a uniform product layer, the solid product is assumed to be dispersed nuclei and grows on the grain surface, as can be observed in Figure 1 (b). Before coalescing into a continuous layer and, consequently, the surface morphology appearing as pores, the solid product phases nucleate at discrete points on the surface of the grain (Bao et al., 2013). The general form for pre-reduction or direct reduction with H2 can be represented by Equation 2. Pre-reduction of chromite with H2 is represented by Equation 3.

$$R_s + aA_g \rightarrow bP_s + cH_2O \quad [2]$$

$$V_AFeCr_2O_4(s) + V_BH_2(g) \rightarrow V_pFe(s) + V_SCr_2O_3(s) + V_QH_2O(g) \quad [3]$$

In the modelling of pre-reduction of chromite with H_2, it was assumed that a chromite pellet is composed of micro-grains and that the reactions occur in the micro-scale pores resulting in micro-structural changes within the pellet (Li, 2020). Unlike the grain and shrinking core models that assume that the solid product forms a continuous layer covering the surface, the current model describes the solid product's discrete islands morphology on the solid reactant's surface. Notwithstanding the reaction regime, the shrinking core model assumes a shrinking reaction interface in a non-porous pellet while the grain model assumes that a porous pellet is made up of non-porous grains of reactant solid, with reactions taking place on the unreacted grain surface (Ahn, Choi, 2017). Compared to the shrinking core model, the grain model can describe the reaction front propagation throughout the reaction regime. This is because the grain model can describe the reaction front propagation as an interplay between mass transfer and reaction kinetics. Since the current model works on porous particles, it can characterise the effect of intraparticle diffusion through the pores and that, coupled with the ability to predict the discrete nuclei product growth morphology, renders this model crucial for describing the structural and chemical features of the reaction steps.

The rate of change of the ratio of unoccupied surface area (δ) and unoccupied grain radius (r_2) is represented by Equations 4 and 5, respectively. In Equations 4 and 5, r_2 tracks how the grain radius shrinks while δ tracks how much grain surface area is unoccupied

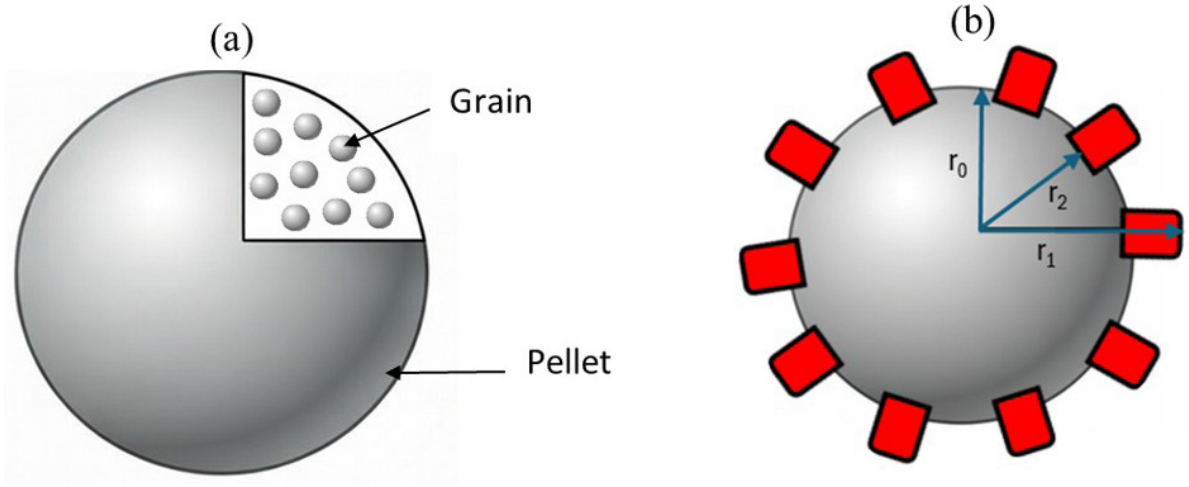

Figure 1—A picture of grain and pellet scale (a) and product islands on the grain surface (b)

by the solid product phase. Since the current model does not assume that the solid product forms a continuous and uniform layer covering the grain surface, δ is used to track the available surface area before the solid-phase products coalesce into a continuous layer.

$$\frac{d\delta}{dt} = -\frac{1}{a}\frac{V_{Rs}k}{h_c}\delta\eta(C_s - C_{eq}) \quad [4]$$

$$\frac{dr_2}{dt} = -\frac{1}{a}\frac{V_{Rs}k}{r_2(r_1-r_2)^k/_{D_p r_1}+1}\eta(C_s - C_{eq}) \quad [5]$$

In these equations, h_c is the critical reactant layer thickness, r_1 is outward grain radius defined by Equation 6, D_p is gas diffusivity through the product layer, VRs is molar volume of chromite, k is the rate constant, a is the stoichiometric factor of H_2,C_{eq} is the equilibrium gas concentration, and C_s is the surface concentration.

$$r_1 = \left[r_2^3 + (r_0^3 - r_2^3)b\,V_{ps}/V_{Rs}\right]^{1/3} \quad [6]$$

The grain conversion rate is defined by Equation 7, where α is grain conversion, k_s is the reaction rate for surface reactions and is represented by Equation 9, and k_p is the reaction rate based on species diffusion through a product layer, and r_0 is the initial grain radius.

$$\frac{d\alpha}{dt} = [\delta k_s + (1-\delta)k_p]\eta(C_s - C_{eq}) \quad [7]$$

$$k_p = \frac{1}{a}\frac{3r_2^2}{r_0^3}\frac{V_{Rs}k}{r_2(r_1-r_2)^k/_{D_p r_1}+1} \quad [8]$$

$$k_s = (1-\frac{r_2^3}{r_0^3})V_{Rs}\frac{k}{ah_c} \quad [9]$$

The effectiveness factor (η) defined in Equation 1 can be expressed as a function of Thiele modulus (φ), as shown in Equation 10. The Thiele modulus quantifies the ratio of chemical reaction rate to mass transfer rate by diffusion of reactants in a porous particle, as shown in Equation 11. This dimensionless number is used in scale-up of fixed-bed reactors and can be used to determine optimum pellet size. In Equations 11 to 14, γ represents rate constant, $D(e,s)$ is effective gas diffusivity on the external pellet surface, and ε_s is porosity on the external pellet surface, ε_0 is initial porosity, and b is stoichiometric of solid product and this case Fe.

$$\eta = 3\varphi^{-2}(\varphi\coth(\varphi) - 1) \quad [10]$$

$$\varphi = R_0\sqrt{\frac{\gamma}{D_{e,s}}} \quad [11]$$

$$\gamma = \frac{a(1-\epsilon_0)}{V_{Rs}}\left[\delta k_s + (1-\delta)k_p\right] \quad [12]$$

$$D_{e,s} = \frac{\epsilon_s^2}{D_k^{-1}+D_g^{-1}} \quad [13]$$

$$\varepsilon_s = \varepsilon_0 - (1-\varepsilon_0)\alpha_s(b\,V_{Ps}/V_{Rs} - 1) \quad [14]$$

The pellet conversion rate is expressed by Equation 15, where K_r is the reaction rate constant and is represented by Equation 16, while k_g is the external mass transfer coefficient and expressed by Equation 17.

$$\frac{dX}{dt} = \frac{1}{a}\frac{V_{Rs}}{1-\varepsilon_0}K_r(C_s - C_{eq}) \quad [15]$$

$$K_r = 1\Big/\left\{\frac{R_0}{3k_g} + \frac{V_{Rs}}{a(1-\varepsilon_0)[\delta k_s+(1-\delta)k_p]\eta}\right\} \quad [16]$$

$$k_g = Sh\frac{D_g}{2R_0} \quad [17]$$

Results and discussion

The adjustable parameters in the model calculations include reaction rate constant (k) and gas diffusivity through the product layer D_p. These parameters are defined using the Arrhenius form presented in Equations 18 and 19.

$$k = A_k\exp(\frac{E_k}{R_g T}) \quad [18]$$

$$D_p = A_p\exp\left(\frac{D_p}{R_g T}\right) \quad [19]$$

The kinetic parameters used in the model calculation are shown in Table 1.

Influence of particle size on reducibility

The effect of particle size on the degree of reduction, as predicted by the model, reveal that the degree of reduction increases with decreasing particle size, as shown in Figure 2. The enhanced reduction at small particle sizes can be attributed to topochemical reactions from the periphery to the centre of the particle and this is often the case with dense pellets. However, even with high porosity pellets, larger particle sizes result in increased diffusion path lengths and decreased rate of reduction. Smaller pellet sizes with high initial porosity reduce Thiele Modulus due to increased diffusive flux and increases in effectiveness factor, resulting in uniform utilisation as opposed to reactions confined to the outer shell.

Table 1

Kinetic parameters in the ROM

Parameter	Value
Ek (kJ/mol)	1.1 x 10^5
Ak (m^2/s)	1.4 x 10^2
Ep (kJ/mol)	1.6 x 10^4
Ap (m^2/s)	7.1 x 10^{-14}

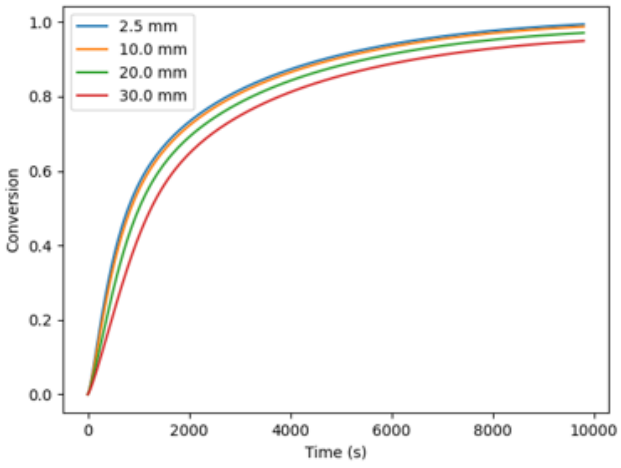

Figure 2—Influence of particle size on degree of reduction

Influence of temperature on reducibility

Chromite pre-reduction with H_2 represents heterogeneous reactions where reactions occur at the phase boundaries and they depend on heat and mass transfer between the reaction interface and the bulk fluid. As can be observed in Figure 3, the rate of conversion increases with increasing temperature, however, the difference is not as pronounced as when different particle sizes are used, highlighting that the process is governed by diffusion limitations.

Influence of porosity on reducibility

The influence of initial porosity on the degree of reduction is presented in Figure 4. Generally, species diffusion through a porous bed proceeds in parallel through macropores and micropores, however, in the current study, only the distribution of macropores was considered. As observed, the degree of reduction increases with increase in porosity due to enhanced H_2 mass transfer. At low porosity, species transport becomes more tortuous, resulting in severe transport limitations and reduced rate of reduction. Reduction at high porosity is characterised by steep conversion gradients, as evidenced by the results in Figure 4. Increasing initial porosity to above 0.4 presents minimal benefit to the rate of reduction and this was also observed in the study of Wang et al. (2021).

Changes in core radius and unoccupied reactant surface

The results in Figure 5 show that the unreacted core radius of the grain decreases while the fraction of unoccupied reactant surface area(δ) decreases. The formation of solid products Fe and Cr_2O_3 result in the decrease of the fraction of unoccupied reactant surface area. Initially, the rate of reduction is rapid and reaches a plateau-type (Figure 4), indicating two rate controlling mechanisms. The decrease in reduction rate represented by a plateau-type is due to an increase in the fraction of occupied surface area, which could have resulted in diffusion limitations.

Model validation

The model predictions for the degree of reduction were compared with experimentally determined degree of reduction, as shown in Figure 6. The isothermal reduction experiments were conducted with H_2 over a temperature range of 1200 °C to 1400 °C . The number of chromite pellets used for each test was limited to 4 and the total mass of charge per test was 10 ±0 .5 g. The number of pellets used was chosen to facilitate enhanced mass transfer of H_2 to the reaction sites. The furnace was heated at a rate of 10 °C/min under an Argon (*Ar*) atmosphere with a flow rate of 2 L/min. Upon reaching the target temperature, H_2 was introduced at 1 L/min. Simultaneously, the Ar flow rate was reduced to 1 L/min to maintain a constant total flow rate of 2 L/min and a 1:1 (H_2:Ar) gas ratio. Upon reaching the targeted temperature, the furnace was maintained at temperature for 2 hours. At the end of 2 hours holding time, Ar flow rate was increased to 2 L/min, the reducing gas flow stopped, and immediately followed by stopping power input to the furnace to facilitate the

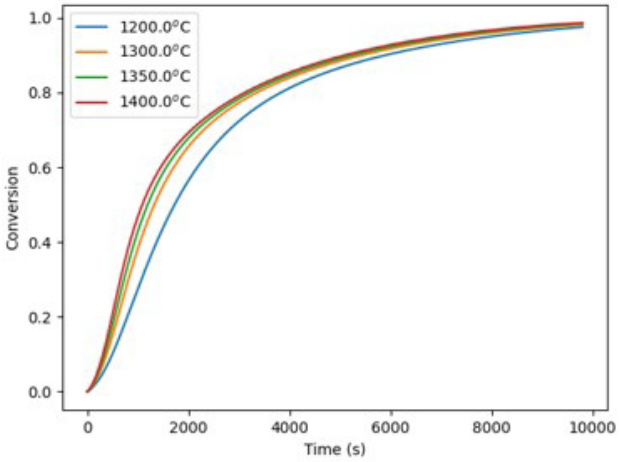

Figure 3—Influence of temperature on the degree of reduction

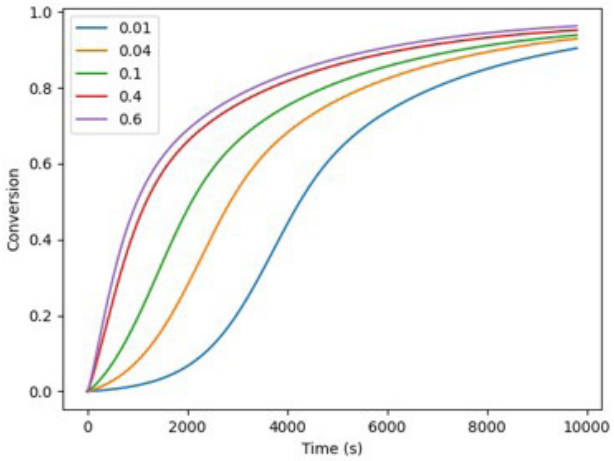

Figure 4—Influence of porosity on the degree of reduction

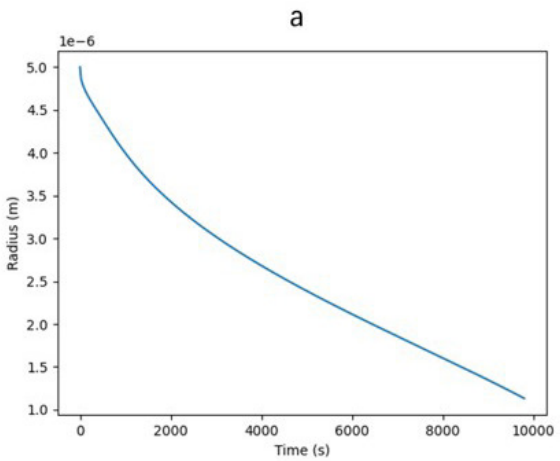

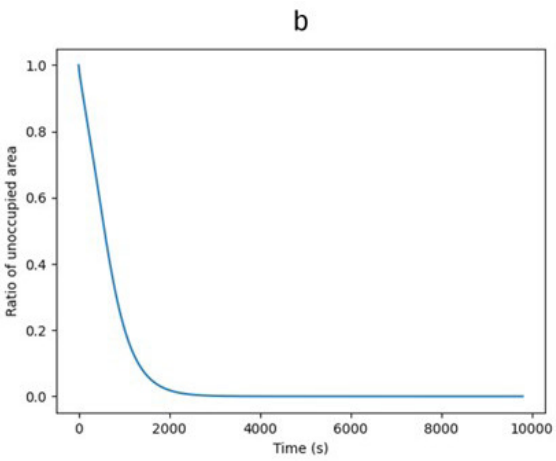

Figure 5—Changes in grain radius (a) and ratio of unoccupied reactant surface (b)

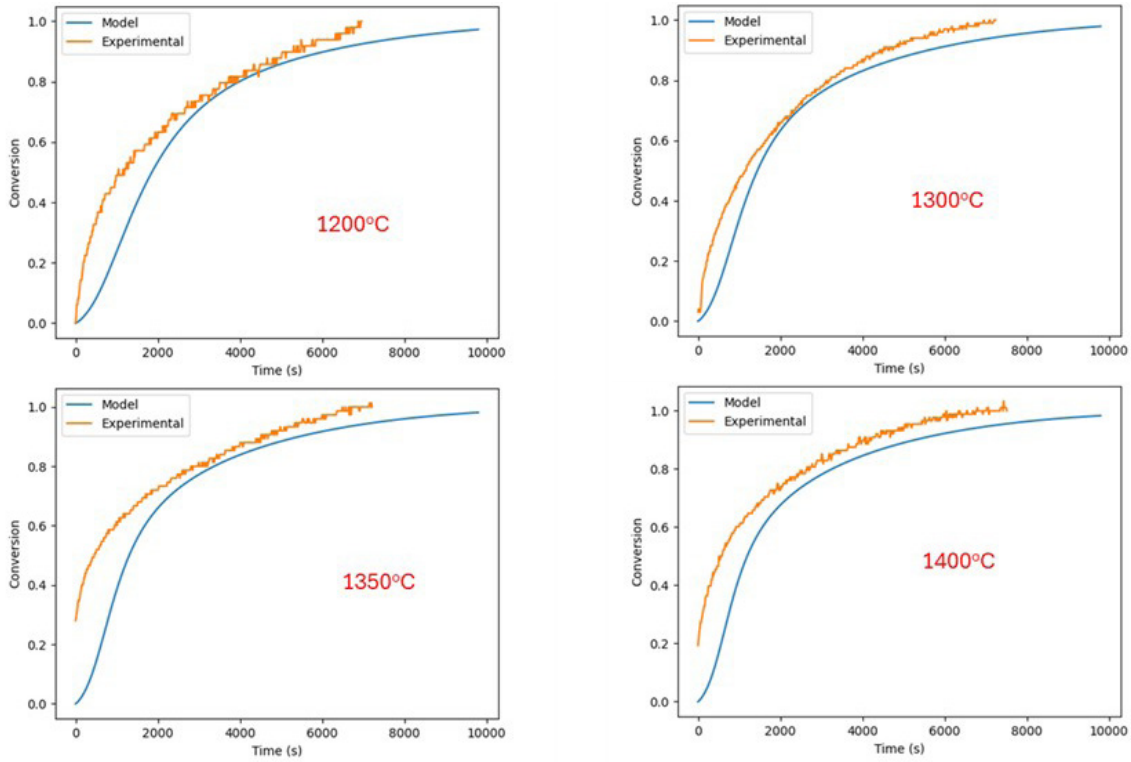

Figure 6—Comparison between experimental and model results

cooling of the sample in Ar. The full details of the method used to obtain experimental data for isothermal pre-reduction of chromite pellets using a thermogravimetric furnace is described by Khama et al. (2026). While the overall behaviour and degree of reduction fairly agree, there are still some significant differences. For instance, the final conversion across all temperatures, as predicted by the ROM, deviate from the experimentally calculated conversion by a maximum error of 2.7% while the initial conversions differ significantly, reaching a maximum error of 65%. These are primarily due to the ROM neglecting sintering and bed non-uniformities caused by flow and heat transfer effects. Specifically, the model fails to account for flow maldistribution caused by surface friction and horizontal momentum transfer into the pressure field (Hollands et al., 1984). Experimental measurements indicate that sintering takes place at temperatures above 1400 °C and the ROM does not capture how sintering retards reaction rates by increasing grain size, reducing available surface area, and elevating mass transfer resistance within the product layer.

Conclusions

A ROM was developed from the effectiveness approach and used to predict pre-reduction behaviour of chromite pellets under H_2 reducing environment. The final conversion across all temperatures, as predicted by the ROM, deviate from the experimentally calculated conversion by a maximum relative error of 2.7% while the initial conversions differ significantly, reaching a maximum error of 65%. Future work will integrate sintering effects and advection terms into the ROM framework to account for convective effects. Once fully validated, the ROM will be used for real-time control and online optimisation of reacting flow systems.

Acknowledgments

This paper is published with the permission of Mintek. The authors are grateful to Mintek for financial support under Science Vote Grant MCR0062604.

References

Ahn, H., Choi, S. 2017. A comparison of the shrinking core model and the grain model for the iron ore pellet indurator simulation. *Computers and Chemical Engineering*, vol. 97, pp. 13–26. https://doi.org/10.1016/j.compchemeng.2016.11.005

Bao, J., Li, Z., Sun, H., Cai, N. 2013. Experiment and rate equation modeling of Fe oxidation kinetics in chemical looping combustion. *Combustion and Flame*, vol. 160, no.4, pp. 808–817. https://doi.org/10.1016/j.combustflame.2012.12.010

Ghadi, A. Z., Valipour, M.S., Vahedi, S.M., Sohn, H.Y. 2020. A Review on the Modeling of Gaseous Reduction of Iron Oxide Pellets. *Steel Research International*, vol. 91, no.1. https://doi.org/10.1002/srin.201900270

Hamadeh, H., Mirgaux, O., Patisson, F. 2018. Detailed modeling of the direct reduction of iron ore in a shaft furnace. *Materials*, vol. 11, no. 10. https://doi.org/10.3390/ma11101865

Hollands, K.G.T., Sullivan, H.F., Shewent, E.C. 1984. Flow Uniformity In Rock Beds. Solar Energy, vol. 32, no. 3, pp. 343–348.

Khama, M.I., Baloyi, B.MV., Reynolds, Q. G., Xakalashe, B.S., Chetty, D. 2026. Kinetics of Isothermal and Non-Isothermal Pre-Reduction of Chromite with Hydrogen. Hydrogen, vol. 7, (no. 1), pp. 21. https://doi.org/10.3390/hydrogen7010021

Li, Z. 2020. General rate equation theory for gas–solid reaction kinetics and its application to CaO carbonation. *Chemical Engineering Science*, vol. 227. https://doi.org/10.1016/j.ces.2020.115902

Lu, H.-B., Mazet, N., Spinner, B. 1996. Modelling of gas-solid reaction-coupling of heat and mass transfer with chemical reaction. *Chemical engineering science*, vol. 51, no. 15, 3829–3845.

Wang, H., Li, Z., Cai, N. 2021. Reduced-order model for redox kinetics of oxygen carrier in chemical looping combustion. Proceedings of the Combustion Institute, vol. 38, no. 4, 5271–5279. https://doi.org/10.1016/j.proci.2020.08.002 ◆

YOUNG PROFESSIONALS COUNCIL

SAIMM
THE SOUTHERN AFRICAN INSTITUTE OF MINING AND METALLURGY

7TH YOUNG PROFESSIONALS CONFERENCE

29-30 SEPTEMBER 2026
MINTEK, RANDBURG, JOHANNESBURG

ECSA and SACNASP Validated CPD ActivityCredits = 0.1 per hour attended

The role of youth and young professionals in Future Proofing African Mining, Today

The conference promises to be an engaging and informative event that will explore the latest trends, ideas, and innovations in the minerals industry. This conference offers young professionals the opportunity to network with peers and industry experts, establish professional relationships, and collaborate on future projects. A conference dedicated to young professionals emphasises the importance of empowering young professionals to lead the way in driving innovation and sustainability in the South African minerals industry.

OBJECTIVES

- During the conference, attendees can expect to participate in engaging sessions, informative talks, and interactive workshops covering a broad range of topics. These sessions will explore innovative technologies, sustainable mining practices, and the role of young professionals in driving positive change in the industry.
- In addition to the informative sessions, there will be ample opportunities to network with peers and industry experts, share ideas, and collaborate on projects. The conference will provide a platform for attendees to showcase their work, gain feedback, and receive recognition for their contributions.
- To promote diversity and inclusion in the mining industry by creating an environment that supports and celebrates individuals from all backgrounds.

Overall, the conference is a must-attend event for young professionals in the minerals industry. Whether you are an early-career professional or an experienced industry expert, this conference is an excellent opportunity to learn, network, and contribute to the future of the minerals industry in South Africa.

Key Dates:

4 May 2026 - Submission of abstracts

22 June 2026 - Submission of papers

29-30 September 2026 - Conference

FOR FURTHER INFORMATION, CONTACT:

Gugu Charlie,
Conferences and
Events Coordinator

E-mail: gugu@saimm.co.za
Tel: +27 11 538 0238
Web: www.saimm.co.za

Technology evolution in the Southern African Ni-Cu-Platinum Group Metals (PGM) smelting industry

by R. Hundermark, G. Marsden, R. Snodgrass, K. van der Merwe

Affiliation:
Valterra Platinum, Johannesburg, South Africa

Correspondence to:
R. Hundermark

Email:
rodney.hundermark@valterraplatinum.com

Dates:
Received: 19 May. 2026
Published: July. 2026

How to cite:
Hundermark R., Marsden G., Snodgrass R. van der Merwe K. 2026. Technology evolution in the Southern African Ni-Cu-Platinum Group Metals (PGM) smelting industry. *Journal of the Southern African Institute of Mining and Metallurgy*, vol. 126, no. 7, pp. 411 – 426

DOI ID:
https://doi.org/10.17159/2411-9717/1048/2026

ORCiD:
R. Hundermark
https://orcid.org/0009-0004-4713-2200
G. Marsden
https://orcid.org/0009-0002-6750-5778
R. Snodgrass
https://orcid.org/0009-0008-8470-7666
K. van der Merwe
https://orcid.org/0009-0005-6323-1951

This paper is based on a presentation given at the SAIMM Pyrometallurgy International Conference 2026, 26-28 May 2026, CSIR International Convention Centre, Pretoria, South Africa

Abstract

The Southern African Ni-Cu-PGM smelting industry has evolved significantly from 1937 to date. As demand for platinum group metals has increased, smelting technology development has been closely linked to the need to process more concentrate, but also to changes in the chemistry and mineralogy of concentrates from the various platinum group metals-containing reef types.

Early technologies relied on blast furnaces and Great Falls converters, but from the late 1960s, electric furnaces and Peirce Smith converters were commissioned. In the early 1990s, the introduction of water-cooled copper plate coolers into the slag zones of the primary furnaces enabled greater power intensity and throughput, with further intensification from the early 2000s requiring the use of deep-cooled copper coolers. Converting technology was also modernised to include a top submerged lance converter in one instance. Approaches to converter slag cleaning have evolved from recycling slag to the primary furnaces, to milling and flotation or electric furnace slag cleaning as the Cr_2O_3 content in slags has increased.

The shift in the 1990s from Merensky ore derived concentrates to those from UG2 ores impacted the process design for the primary furnaces, with UG2 concentrates having lower matte falls and higher Cr_2O_3 levels. Conversely, concentrates derived from Platreef and Great Dyke ores, with high matte falls and lower Cr_2O_3 levels, have introduced other challenges. Furnace designs and operating philosophies have been improved to better handle these ranges of concentrates, the resulting slags and superheated mattes, the containment of which is non-trivial. The smelting of non-roasted concentrates in the primary furnaces gave rise to rapid corrosion of the copper coolers, and triggered development of corrosion mitigation strategies.

Advances in SO_2 emissions control have transitioned from single contact sulphuric acid plants in the 1970s, to the adoption of double contact acid plants, tailgas, and dual-alkali scrubbing in the early 2000s. Low SO_2 strength off-gas streams from primary furnaces are abated in some cases, with technologies such as the Sulphacid process introduced from the early 2000s and the Wet-gas Sulphuric Acid process from the early 2020s.

With advances in process intensification, increases in operating temperatures and throughputs, and use of water cooling, consequences of furnace failures have become more severe. Water leaks into the molten material environment, primary furnace containment, and slag granulation have been particularly challenging. Technologies, operating, and maintenance philosophies have been developed for prevention and mitigation of failures, and the adoption of process safety management approaches has yielded systematic benefits.

With the outlook in demand for PGMs changing as a function of automotive requirements, smelting technology will continue to evolve for further enhancement of safety and environmental protection, reduced costs, and greater efficiencies.

Keywords

Pyrometallurgy, smelting, converting, acid plants, slag cleaning, Platinum Group Metals (PGM)

Introduction

Southern Africa has dominated the supply of platinum group metals (PGM) into world markets, given the resource endowments associated with the Bushveld Igneous Complex in South Africa and the Great Dyke in Zimbabwe. The overall supply from South Africa has contributed on average 75% of the world's platinum from 1975 to 2008, and from 2008 to date, South Africa has contributed ~72% and Zimbabwe ~7% of the supply. The significant growth in absolute supply from South Africa from the 1970s to 2007 was brought about by major expansions in the mining and processing operations in the country, and

more recently in Zimbabwe (Figure 1). The focus of this paper is on the evolution of technology and flowsheets within the smelting operations of the Southern African PGM industry players, as a function of the changes in capacity requirements, concentrate feedstock types, and changes in legislation.

Early history

The discovery of the Bushveld Igneous Complex platinum deposits in 1924 brought about investment in mining and processing operations by the newly founded Rustenburg Platinum Mines (RPM, later owned by Anglo Platinum, then Anglo American Platinum, and now Valterra Platinum). In 1931 the first recovery plant using gravity concentration and flotation was commissioned, with concentrates exported to England to be smelted and refined at the Johnson Matthey (JM) works in Brimsdown and Royston. The platinum price collapse in 1932, induced by the Great Depression, momentarily slowed production output but increased demand for PGMs soon followed, resulting in higher tonnage mined with a greater proportion of sulfide-bearing ore and flotation concentrates. This posed a new challenge for metallurgists: to implement a treatment method which would reduce bulky shipments overseas and render the concentrate suitable for refining. A variety of treatment methods were considered, and it was found that smelting the flotation concentrate to produce a nickel-copper matte, as used at scale by JM in Brimsdown, was most successful and achieved high PGM recovery (Beath et al., 1961). In 1937 the first smelting operations were commissioned at Klipfontein in Rustenburg (Figure 2), with initially one small blast furnace and a Great Falls converter (Hochreiter et al., 1985). Converter matte was then shipped to the JM works for further treatment to produce refined PGMs.

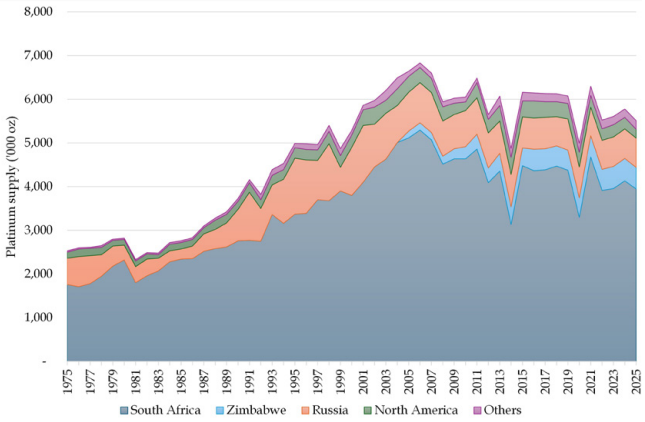

Figure 1—World platinum supply by region (WPIC, 2026)

Mined ore production had increased from 7,500 tonnes per month in 1931 to 25,000 tonnes per month between 1939 and 1945 resulting in 40,000 platinum ounces per annum produced (Beath et al., 1961; Bruce, 1996). The relatively low required smelting rate led to the selection of the blast furnace at Klipfontein. As production rates increased, reverberatory furnaces were considered, but given the ability to readily stop and start the blast furnaces, they were retained, with additional furnaces installed as production needs increased. Feed preparation involved filtering of flotation concentrates in 2.4 m x 2.4 m drum filters and then various methods were initially used to produce a competent feed for the furnaces. These included sintering on a small Dwight Lloyd machine and also making briquettes after mixing with slaked lime and flue dust. The method eventually used was to dry the drum filter cake in Büttner turbo dryers and then pelletise in Lurgi pelletising pans. Green pellets, along with coke, iron ore, and limestone were fed to four blast furnaces. The water jacketed furnaces were 3.05 m long and 0.91 m at the tuyeres and operated in a modular fashion to meet variable production demands. Slag was granulated in a wet launder, separated from water in a rake classifier and then conveyed to a slag dump as is practiced by various smelters today (Beath et al., 1961). Matte was transferred by ladle to three Great Falls-type converters (Figure 2), 3.05 m in diameter, and blown to white metal containing 74% copper plus nickel, cast in moulds, crushed to -76 mm and placed in bags of 68 kg each for shipment (Gouldsmith, Wilson, 1963). Converter slag was cast and returned with other recycles to the blast furnaces.

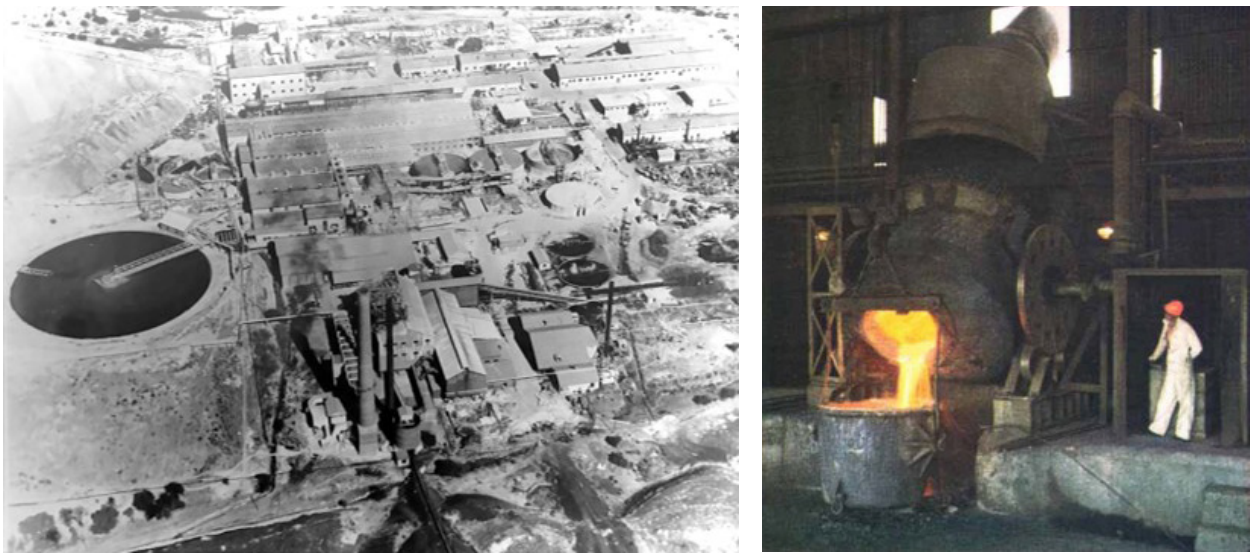

Figure 2—(left) The processing operations at Klipfontein with the smelter shown in the foreground next to the stack; (right) Pouring blown matte from one of the converters (after Johnson Matthey, 1969)

A doubling of production occurred between 1947 and 1949, in part due to the acquisition of Union Platinum Mining Co., whereafter a further doubling in 1951 led to the formation of Matte Smelters (Pty) Ltd., jointly owned by JM and RPM. At this facility, commissioned at Rustenburg during 1954 and 1955, a portion of the converter matte was then also treated, with the balance exported to JM's Brimsdown plant (Bruce, 1996). Both facilities used the Orford process utilising sodium sulfate and coke as reagents in the first step. Blast furnaces and reverberatory furnaces were used in tandem, with careful temperature control to achieve efficient separation of phases. The molten stream from the blast furnace ran into the settler where the copper sulfide or sodium sulfide 'tops' layer and a PGM-rich nickel sulfide 'bottoms' layer were formed. The 'tops' layer was run into a ladle and then charged to a Bessemer converter, where the sodium sulfate blown off was recovered to be recycled to the blast furnace feed. After fluxing iron oxide with silica, the remaining copper sulfide was blown to blister, further refined in reverberatory furnaces, and cast into anodes for electrorefining. The 'bottoms' layer was tapped intermittently, cast, crushed, and ground fine in ball mills. Sulphur was removed by roasting to nickel oxide and then it was briquetted with coal and charged to reverberatory furnaces to form nickel metal and cast into anodes for electro-refining. Pure copper and nickel cathodes were produced from the electro-refining processes and sold locally. The anode slimes from each were further enriched to 65% PGMs by roasting and leaching with sulphuric acid and then sent along with the Rustenburg gravity concentrates to Royston, England, for further refining of gold and PGMs (Gouldsmith, Wilson, 1963).

During the 1960s, further demand for PGMs led to expansion and new entrants in the South African platinum industry. RPM responded with production increases reaching 1 million ounces by 1970 and installation of another jointly owned facility with JM to refine PGMs in Wadeville. The commensurate additional smelting capacity needed could not be installed at Klipfontein, resulting in RPM's decision to construct a new facility at Waterval (also in Rustenburg) in 1969, and the later construction of Mortimer Smelter at Swartklip (near Northam) in 1973. The change in location offered an opportunity to consider new technologies and RPM ultimately selected two Elkem designed 19.5 MVA rectangular electric furnaces and Peirce Smith converters in 1967, which were then installed at Waterval in 1969 (Hochreiter et al., 1985). Concurrently, Impala Platinum had started their mining operations in 1968 and by January 1969 their first 7.5 MVA electric furnace was commissioned, with two more 7.5 MVA furnaces in 1972 and 1973, and a fourth 15 MVA furnace in 1974 (Watson, Harvey, 1992). Converter matte produced by their Peirce Smith converters was treated in a newly built refinery in Springs, utilising the Sherritt Gordon pressure-leaching process. In 1971, Western Platinum—later part of Lonrho, then Lonmin, now part of Sibanye Stillwater (SSW)—started their operations, installing a 12.5MW furnace with converter matte exported to Norway for refining (Eksteen et al., 2011; Hochreiter et al., 1985). A new era had started in the South African PGM industry with the three major role players at the time all using rectangular electric furnaces coupled with Peirce Smith converters.

The selection of electric furnaces was driven by several perceived benefits. Firstly, a move away from blast furnaces due to difficulties preparing competent pellets, increasing operational costs related to coke and labour, and the introduction of more stringent anti-pollution laws, which would have required costly modifications to capture the 1% – 2% sulphur dioxide emissions. Secondly, in comparison to reverberatory furnaces, electric furnaces presented significant benefits in energy efficiency and construction costs. The heat generation through Joule (I2R) heating in the slag bath, rather than convective and radiant heating from a flame above the bath, was far more efficient in melting concentrates, with Mostert and Roberts (1973) estimating thermal efficiencies of 60% for electric furnaces, versus 30% for reverberatory furnaces. Heat transfer, both up and down from slag to charge and slag to matte, resulted in higher matte temperatures compared to reverberatory furnaces with the benefit of also reducing magnetite formation on the hearth and at the slag/matte interface, which could impact matte tapping. The electric furnace also operated with comparatively lower roof temperatures, which impacted furnace design and refractory selection, resulting in a cheaper and more robust solution. Furthermore, and perhaps most significantly, electric furnaces were able to achieve the higher temperatures needed to maintain fluidity of the slags with relatively higher magnesium oxide (MgO) in feeds (Cramer, 2001; Hochreiter et al., 1985; Mostert, Roberts, 1973).

Peirce Smith converters replaced the Great Falls-type converters owing to the inherent advantages of their cylindrical shape and horizontal orientation. "In the vertical orientation, the tuyere immersion varied with their location on the barrel, while in the horizontal design, all tuyeres are at the same depth giving uniform immersion and blowing rates" (Nelson et al., 2018). Furthermore, the acid linings used in the Great Falls converters were seen as far more inferior to the basic chrome-magnesite bricks used to line the new Peirce Smith vessels for the corrosive slags being processed. At Waterval Smelter, furnace matte tapped into 12 tonne cast steel refractory lined ladles was transferred to the Peirce Smith converters along with silica flux and furnace aisle reverts. Converter matte was poured into moulds, cooled, and then crushed to -25 mm and bagged. Converter slag was returned to the electric furnace by means of a cast launder (Mostert, Roberts, 1973).

During the 1970s, the 'slow cooling' process was developed by RPM and JM, whereby the iron content and cooling rate of cast converter matte were controlled such that a PGM-rich Ni-Cu-Fe magnetic alloy was formed separately from a PGM-free nickel-copper matte. The converter matte was cast into a mould, covered with a lid and allowed to cool for approximately 5 – 6 days before being removed and crushed. Subsequent grinding and magnetic separation allowed for the PGMs and base metals to be recovered separately in the base metals and precious metals refineries, which were commissioned in 1981 and 1989, respectively. Following this new process for converter matte treatment, all the RPM smelter downstream processing to produce refined PGMs was conducted at Rustenburg in South Africa.

The impact of concentrate composition

The smelting and converting of nickel-copper PGM concentrates is greatly influenced by the origin of the ore, and targeting of high concentrator PGM recoveries, given the value of the precious metals (yielding high gangue content in the concentrate). These aspects have been covered widely in literature, and a brief overview is provided here as it has meaningfully driven changes in technology. The concentrates are derived from the following reef types in Southern Africa:

- The Merensky Reef reserves, which were exploited initially, are largely depleted. Merensky Reef-derived concentrate is characterised by good PGM and base metal grades, 110 g/t – 150 g/t and 5.5% – 6.3% Ni+Cu, respectively (Mostert, Roberts, 1973), with low chromium

oxide (Cr_2O_3) content. This concentrate type was the predominant feed type influencing the operation of the electric furnaces from the 1970s to late 1990s. During that time, furnace power densities were relatively low, resulting in relatively low operating temperatures, with matte temperatures ranging from 1150 °C to 1260 °C (Forbes, 1977; Watson, Harvey, 1992) and slag temperatures ranging from 1300 °C –1460 °C (Mostert, Roberts, 1973; Watson, Harvey, 1992). Mostert and Roberts (1973) note the high MgO content bringing about 'slags with high formation temperatures', in comparison to the matte with low formation temperatures of ~1000°C. The importance of this difference was further noted with respect to the design of the furnace hearths and transformers.

- The Upper Group 2 (UG2) Reef is associated predominantly with chromitite, with very low base metal content (3.3% Ni+Cu), but high PGM (140 g/t – 340 g/t) and Cr_2O_3 (2.6% – 2.8%) contents (Jones, 1999). The concentrate gives rise to very low matte falls / collector volumes (typically < 10%) when smelted. The high Cr_2O_3 content in the UG2 concentrates has a marked influence on the smelting behaviour in the primary furnaces, which is elaborated on in the following.
- The Platreef ore body on the northern limb of the Bushveld Complex is mined by Valterra Platinum at the Mogalakwena mine, and more recently by Ivanplats. Platreef concentrate is characterised by relatively low PGM grades (60 g/t – 90 g/t), high base metal contents (up to 7% Ni+Cu+Co, according to Shaw et al., 2014), and low chromium oxide content. This concentrate results in high matte falls in the primary furnaces (typically 15% – 30%). The future of the South African PGM industry is likely to become more dominated by concentrates from these northern limb deposits, as new mines are developed in this area.
- Concentrates from Great Dyke Reef deposits in Zimbabwe, are somewhat similar to the Platreef concentrates in terms of having relatively low PGM grades, high base metal content (6.4% Ni+Cu), and low chromium oxide content (0.3%) (Mabiza et al., 2011). This concentrate type also gives rise to high matte falls in the primary furnaces (typically > 30%).

The change in the concentrate feeds to the PGM producers had a marked impact on the smelting operations, particularly towards the late 1990s and early 2000s, as declining Merensky concentrate volumes were replaced with increasing UG2 concentrate volumes.

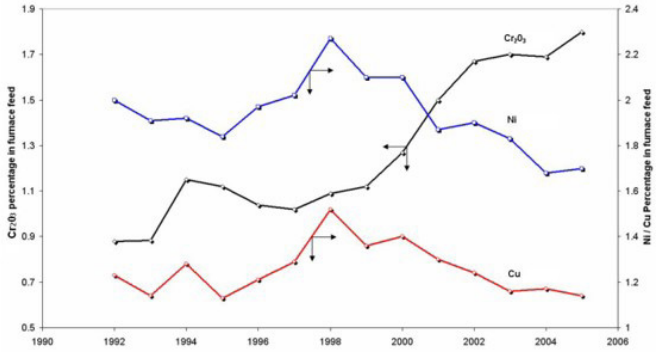

Figure 3—Increasing UG2 in Impala feed blend (after Coetzee, 2006)

This led to an increase in the Cr_2O_3 concentrations in the feed (Figure 3), and hence, slag and matte of the primary furnaces, with numerous negative impacts.

The impacts of Cr_2O_3 on the primary furnaces are well documented (Watson, Harvey, 1992; Jones, 1999; Merkle, McKenzie, 2002; Nell, 2004; Coetzee, 2006; Eksteen et al., 2011; Shaw et al., 2014), with a summary of the key issues provided in the following:

- Combined with the high MgO content in the slags, the Cr_2O_3 drives up the slag liquidus temperatures, and hence, operating temperatures. Slag operating temperatures transitioned from 1300 °C – 1460 °C for Merensky-dominant feeds to 1500 °C – 1680 °C (Eksteen et al., 2011), and at times higher, for UG2-dominant feeds. The higher slag operating temperatures greatly elevate the matte operating temperatures to as high as 1600 °C. Given the much lower matte liquidus and solidus temperatures (850 °C – 1000 °C and ~650 °C, respectively) (Eksteen et al., 2011, Rivera Li Kao, Garbers-Craig (2025), the very high matte superheat creates challenges in containment of the matte, particularly for activities around the matte tapholes (Shaw et al., 2014). The other impact of the high slag operating temperatures is increased slag electrical conductivities, which lead to shallower electrode immersions for furnaces with transformers with constrained secondary current capability, particularly when FeO-rich converter slag is returned to the primary furnaces.
- Chromium spinel forms in the furnaces due to limited solubility of the Cr_2O_3 in the slag. Merkle and McKenzie (2002) discuss Cr_2O_3 solubility being a function of slag composition and oxidation state, with higher solubility under slightly reducing conditions. Given the density of the spinels being higher than the slag and matte densities, spinel accumulation on the hearths leads to reduced volume. Watson and Harvey (1992) noted a significant concern of 'severe' build-up for Cr_2O_3 levels above 1%, albeit with furnaces operating at relatively low power densities, and motivated the increase in hearth power density on Impala F5. Later, with more intensely powered furnaces, chromium oxide solubility levels of 1.8% are mentioned, with which the Impala operation was coping (Coetzee, 2006). The presence of spinels when processing concentrates with Cr_2O_3 contents of up to 4% also drove the decision to install large transformers on the RPM Polokwane furnace (3 × 56 MVA) to allow for deep electrode immersions (75%), with the intention of enabling stirring and melting of hearth build-up (Nelson et al., 2005).
- Hearth build-up has been linked to higher entrained matte losses in slag, and significant concern around matte being tapped out slag tapholes, particularly with water granulation of slag (Watson, Harvey, 1992). The reduced amount of matte collector with UG2-rich concentrate blends also negatively impacts base and precious metal recoveries (Nell, 2004).
- Increases in hearth build-up, particularly in the colder, more quiescent areas of the furnaces (typically the tapping ends of rectangular furnaces), lead to matte tapping difficulties, with slow tapping rates and mixtures of matte, intermediate layer, and slag being tapped. In addition, spinel precipitation in launders and ladles creates both

practical tapping problems of keeping the launders and ladles clean, but also leads to reverts generation (Eksteen et al., 2011).
- Intermediate, spinel-rich layers between matte and slag lead to poor matte-slag separation and difficulty in distinguishing between the two liquid layers on a sounding bar for level measurement.
- Cr_2O_3 in furnace matte is transferred to the converters, where the high incoming matte temperatures, combined with spinel precipitation around the tuyeres leads to reduced campaign lives of the converter refractories (Eksteen et al., 2011).
- Cr_2O_3 in the converter feed reports to the slag, and historical practice involved returning the slag to the primary furnaces. The recycle of both magnetite and chromite spinels to the primary furnaces further exacerbated the build-up issues in the furnaces, along with high slag operating temperatures and shallow electrode immersions. This ultimately led to the South African PGM producers discontinuing converter slag return (Coetzee, 2006).

A further feature of the smelting of the Southern Africa Ni-Cu-PGM concentrates is that they are dried and then directly smelted in the primary electric furnaces. The implication of this is that the base metal and iron sulfide mineral phases thermally decompose in the furnaces, giving rise to labile sulphur (Mabiza et al., 2011). The bulk of the labile sulphur reacts with oxygen in the freeboard of the furnace and is emitted to the off-gas system as SO^2, however, some elemental sulphur persists in the concentrate bed ('blacktop') inside the furnace. Prior to 1991, when furnace power densities were low, and few copper coolers were installed, the presence of the elemental sulphur was not problematic. However, when copper plate coolers, and later deep-cooled copper coolers were introduced, their cold surfaces allowed for the condensation of gaseous species on the copper. This led to sulfidation of the copper – a process that is accelerated by the presence of chlorides also present in the concentrate, which has led to the failure of coolers, as detailed by Shaw et al. (2014), and in turn the solutions, which were explored and implemented. Additional details are provided further on in this paper.

The impact of processing greater volumes of Platreef and Great Dyke concentrates have been twofold. The first relates to the quantity of input sulphur into the furnaces, exacerbating copper corrosion issues, and the second relates to the quantity of matte that needs to be tapped. Historically, the primary smelting furnaces only had two matte tapholes. However, with greater volumes of highly superheated matte requiring tapping, the frequency with which matte tapholes needed repairs increased. The time taken for matte taphole repairs started to impact overall furnace availability, prompting the need for the installation of a third matte taphole on several furnaces handling higher matte volumes. A fourth matte taphole has been included in a recent furnace installation.

Concentrate handling and drying

The move to electric furnaces in the late 1960s required new drying and feeding systems to prepare the material. RPM and Impala initially selected 'wet' feeding systems. These included a drying stage, and a pelletising stage in RPM's case. The initial installation at Impala consisted of drum filters and coal-fired turbo-tray dryers to produce 6% – 8% moisture (Watson, Harvey, 1992). This material was fed to the furnace via a conveyor and feed bin system. This method of feeding created significant operating challenges, which included difficulties in transporting the concentrate, heaping inside the furnace, which required manual rabbling, frequent furnace 'blow-backs', high dust losses, and a very poor working environment. In addition, the drawback of wet feed to the furnace contributed to a high specific energy consumption of 967 kWh/t in the early 1970s (Plasket, Ireland, 1976).

RPM's Waterval Smelter configuration included drying and pelletising, in an attempt to improve furnace operations and working conditions. The concentrate was dried in Buttner dryers from 21% to 7% moisture. Coal-fired furnaces were used to provide the drying energy. The dried concentrate was fed to the pelletising process (Figure 4) and then dried further to produce dried pellets of 2% moisture (Mostert, Roberts, 1973). These dried pellets were fed with fluxes and reverts via conveyors, feed bins, and shuttle conveyors to the furnace. The move to pellets was calculated to increase smelting capacity by 25% (Mostert, Roberts, 1973)

Figure 4—(left) Pelletising pans at the Waterval Smelter (after Mostert and Roberts, 1973); (right) Flash dryers and dry concentrate silo at Polokwane Smelter (Anglo American Platinum, 2016)

and reduce dust losses and blow-backs. Another benefit, when combined with sufficient feeding ports (4 around each electrode and one between the electrode and each wall), was more complete coverage of the furnace bath. This lowered freeboard temperatures and reduced stresses on the furnace roof and off-gas systems.

In 1972 Impala introduced the first spray drying tower (Niro spray tower) to produce concentrate of less than 0.5% moisture (Watson, Harvey, 1992). Coal-fired hot gas generators provided the energy and the hot gas contacted with the concentrate slurry in a counter-current process to produce dry product. High-efficiency filters on the back end of the dryer system minimised losses in the drying process. The challenge of feeding dry concentrate to the furnace was managed by combining the dry material with the concentrate pulp, in paddle mixers, to produce a damp feed of ~5%. This enabled the continued use of the existing furnace feed systems and eliminated manual rabbling, however, the operational challenges of the wet feed, mentioned already, remained.

The first implementation of 'dry' feeding to Impala's furnaces occurred in 1986. Pneumatic conveying technology enabled the contained transport of dry material to furnace feed bins. Additional modifications to the furnace charging systems and a significant reduction in the number of feed ports accompanied the change. The dry feeding used the very low angle of repose of dry concentrate to create a blacktop across the entire surface of the molten slag, through the significantly reduced number of feed ports (28 ports down to 4 – 6 per furnace side). The dry feeding enabled a 12% – 15% increase in furnace efficiency (Watson, Harvey, 1992). Further improvements included reduced blow-backs and off-gas volumes from a reduction in water content. The CaO content in the primary furnaces was controlled using limestone at that stage, and the introduction of the contained pneumatic conveying systems also allowed for a change to burnt lime, which also provided an energy-efficiency benefit.

RPM introduced flash dryers into the Waterval flowsheet in 1992. Coal-fired hot gas generators also provided the energy requirement for the drying process, which involved hot gas and wet concentrate filter cake being combined in a co-current drying column to produce a dry product of less than 0.5% moisture. The flash dryer achieved 90% – 95% thermal efficiency, significantly higher than traditional spray dryers, which achieve 45% – 65% thermal efficiency (Cheng et al., 2018; Kemp, 2012). Cyclones and baghouses are used to provide the solid-gas separation and prevent significant dust losses, although the first installation at Waterval utilised a wet venturi scrubber process for the final dust recovery step. This change to dry feed eliminated the pelletising process, boasted lower capital, maintenance, and labour costs, and has a more effective dewatering capacity when compared to the other drying technologies previously used.

Currently all PGM smelters in Southern Africa utilise the flash dryer or spray drying process to produce the dry concentrate for feeding in the furnaces (Figure 5). Flash drying technology is favoured due to better energy efficiencies.

Electric furnace development

All the early electric furnaces, from the end of the 1960s, were rectangular in design with six electrodes set in a line. Both Impala and Western Platinum (SSW) made use of Barnes-Birlec designs while RPM used an Elkem design. All electrodes were Soderberg designs and are still retained today. The furnace and electrode designs were selected based on the relatively low power density requirement for Merensky sourced concentrates, cheap electricity costs in South Africa, and the cheaper operating cost of Soderberg electrodes relative to pre-baked graphite electrodes. Additional rectangular furnaces were installed by Impala and RPM in the 1970s, based on the successes of the initial installations with some improvements. To counter the impacts of the increased UG2 feed and spinel formation in the furnaces in the 1980s and 1990s (Figure 3), the route followed was to increase the stirring within the furnace by increasing the power density, and in other cases a preference for circular furnaces emerged. SSW were the first to install two circular furnaces in 1982 for UG2 concentrate smelting and later installed three more circular furnaces in 1991. These furnaces operated successfully and prompted SSW to continue using circular furnaces and also formed the basis for their scale-up to larger furnaces.

The PGM industry saw an increase in demand for its metals from the early 1990s to early 2000s, driven predominantly by vehicle autocatalyst and jewellery markets (Figure 1), and supply needed to increase to match this demand. This was achieved by increasing mining and concentrating capacity, which then required additional smelting capacity, resulting not only in the installation of new furnaces, but also the increase in capacity of existing furnaces. Rectangular furnaces were amenable to increased power levels (Figure 6), where the power ratings of three furnaces were approximately doubled from their original installed capacity with little change to hearth area (Waterval Furnace 1 and 2 and the Mortimer furnace with power increases from ~18 to 34 MW – 38 MW). Impala Platinum also increased furnace power from 7.5 MW to 38 MW, but this had a substantial increase in hearth area. In

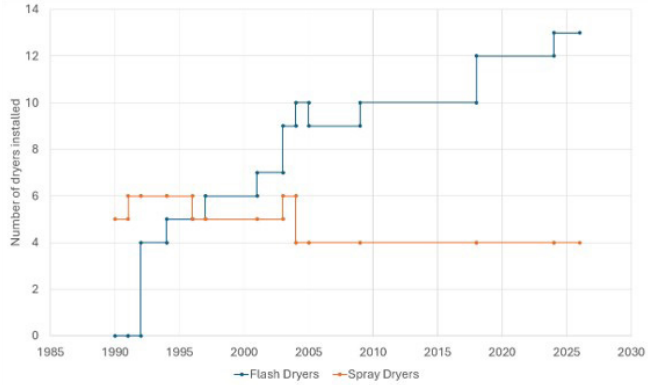

Figure 5—Concentrate dryers installed in the Southern African PGM industry

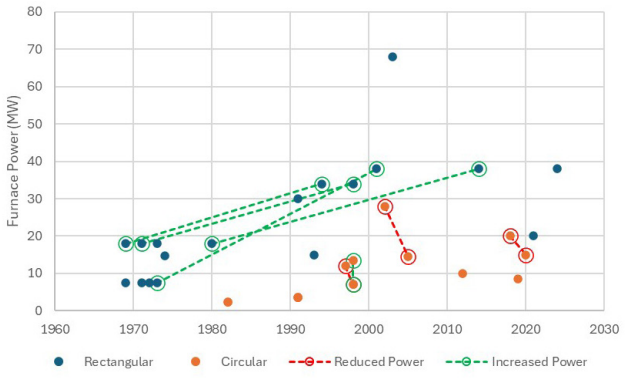

Figure 6—Furnace power over time (circular furnace power input reduction timing indicative)

2003, RPM also commissioned the largest PGM furnace (68 MW) to date at Polokwane, driven not only by market demand, but also by location and projected reserves. Larger circular furnaces were also installed at this time, however, operated at significantly lower power than planned.

Almost all installations prior to 1991 had hearth power densities of less than ~100 kW/m². These earlier furnaces made use of magnesite refractories for lower side walls, upper and lower hearths, while fireclay bricks were used for the hearth infill, upper walls, and roof (Watson, Harvey, 1992). The walls were either uncooled (natural convection), water film cooled, or water jacket cooled, while the hearths were forced-draft air cooled.

From the 1990s onwards, higher powered furnaces were installed, with increased hearth power densities of up to 175 kW/m². The increase in operating temperatures and the chemical aggressiveness of both matte and slag increased, and so lower side wall and upper hearth refractories were changed to chrome-magnesite qualities. Also associated with the increase in the power input to the furnaces at this time, sidewall cooling was introduced in the form of water-cooled copper plate coolers (Watson, Harvey, 1992). The wall cooling allowed for a slag freeze lining to form on the wall hotface, which then protected the refractory from slag attack (Sarvinis et al., 1999). As power intensities increased further in the early 2000s, with hearth power densities exceeding 200 kW/m², wall cooling intensity was increased to cater for increased wall heat fluxes (Figure 7). To achieve this, deep-cooled copper coolers were introduced, designed for peaks of up to 440 kW/m² (Nelson et al., 2005).

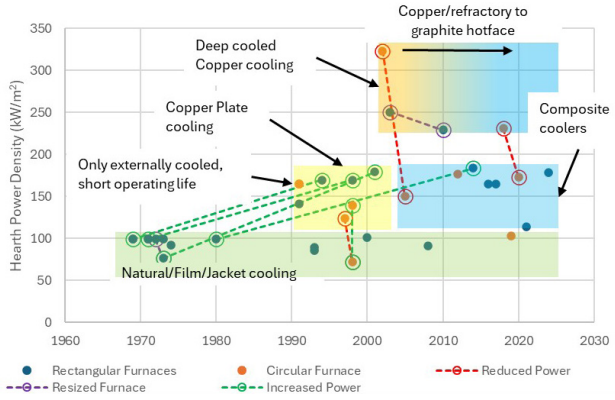

Figure 7—Evolution of electric furnace hearth power density and indicative changes in slag zone cooling technology over time (note: variations and combinations exist)

Deep-cooled coolers easily managed the thermal duty for maintaining slag freeze linings. However, their useful lives were short due to the rate of chloride-accelerated sulfidation corrosion (Shaw et al., 2014) and much less copper between the cooler hotface and the internal water passages, compared to plate coolers. The Polokwane furnace experienced a cooler failure within a year in 2005 (Hundermark et al., 2014). Work commenced on improving corrosion resistance of the deep-cooled coolers during which graphite was trialled on the hot face of the copper, which proved to be effective at reducing the rate of corrosion (Eksteen et al., 2011; Shaw et al., 2014). The key technology developments, which arose in response to the corrosion issues were:

1. Reduction in the copper cooler sizes to enable more rapid replacement of corroded sections, saving on both replacement costs and time.
2. Automated, regular pressure testing of the copper coolers for early detection of leaking components.
3. Corrosion protection barriers, particularly graphite, were installed on the hotface of the copper, which have proven to be very effective in slowing the corrosion rate (Shaw et al., 2014). The use of graphite on the hotface has extended the copper component campaign lives, however, sulphur access to the sides, top, and bottom of the copper gives rise to the need to replace coolers periodically.
4. Following the success of graphite on deep-cooled coolers and recognising the corrosion of shallow-cooled plate coolers, graphite was also introduced into the plate-cooled furnaces from 2014 onwards by sandwiching graphite between the plates forming a 'composite cooler'. Earlier trials of composite coolers were undertaken at Polokwane from 2011. This transition from plate coolers to composite coolers has increased the useable life of these coolers on the lower power intensity furnaces, however, sulfidation corrosion of any exposed copper surfaces persists. This has led to the latest development, which included cladding the copper cooler on the sides, top, and bottom with graphite (Figure 8), and appears to be effective (Joubert et al., 2024; 2025).

The evolution of the side wall cooling technology is shown graphically (Figure 9), with copper plate coolers introduced and then deep-cooled copper coolers. The incorporation of graphite into designs then followed, with various configurations in use.

Figure 8—Clad composite copper-graphite cooler with all copper surfaces protected (after Joubert et al., 2024)

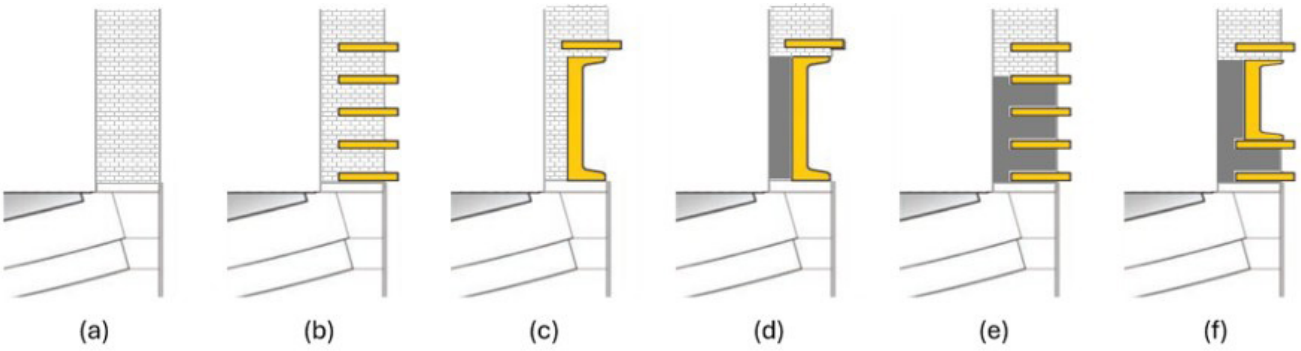

Figure 9—(a) Pure refractory with natural/water film cooling; (b) Refractory wall with copper plates; (c) Deep-cooled copper coolers with refractory on the hot face; (d) Deep-cooled copper coolers with graphite on the hot face; (e) Graphite and copper plate composite cooler; (f) Combination of upper deep-cooled copper and composite cooler

Furnace dimensioning considerations

Rectangular furnace dimensioning considerations include length-to-width ratio and end-wall-to-electrode-distance, while for a circular furnace, the diameter is a ratio of electrode diameter or electrode spacing. The process defines the electrode spacing, size of electrode, and hearth power density required, and thus approximate dimensions are determined (Nelson et al., 2015). In earlier days, dimensioning guides were developed largely from commodities other than PGMs and have thus required optimisation over time, based on operating experience. Examples of this are the 2010 matte wall extension performed at Polokwane, and the modifications to the No. 1 circular furnace installed by SSW.

Two high hearth power density primary electric furnaces were installed in 2001 and 2003, namely, a circular furnace by SSW (320 kW/m^2) and a rectangular furnace by RPM (251k W/m^2) at Polokwane, respectively. RPM also installed a circular slag cleaning furnace in 2003 with a power density of ~260 kW/m^2, which is discussed further on in this paper. The SSW circular furnace experienced containment difficulties and the nominal operating power was reduced from a design power of 28 MW to 14.5 MW (Joubert et al., 2024), bringing the hearth power density down to ~155 kW/m^2, and in line with the hearth power densities of many of the other PGM furnaces. Operating at lower intensity resulted in improved furnace integrity.

RPM's Polokwane furnace also faced containment challenges, experiencing corrosion of copper coolers (discussed in the aforementioned section), and high refractory wear rates of the matte endwall (Hundermark et al., 2014). The furnace was originally designed with the typical design ratio of 0.93 for electrode centre-to-matte-wall/electrode centre-to-slag-wall distances. The wear rate of the slag wall was deemed acceptable while the matte wall was found to wear at an unacceptably fast rate to the point of experiencing a catastrophic failure after just 9 months of operation after an end wall replacement in 2008. This prompted moving the matte endwall in 2010 by 2.7 m farther away from the closest electrode, increasing the matte-end-to-slag-end ratio to 1.45. There were fears of not being able to tap matte from the furnace, but these concerns have proved to be unfounded. Since then, consistent operation at full power (68 MW) has been possible on the Polokwane furnace at a hearth power density of ~230 kW/m^2 and with very good campaign lives on the matte endwall. With the exception of the Polokwane furnace, furnace sizing has favoured similar power densities to those in the 1990s of around 175kW/m^2. Currently, the Polokwane furnace is the only primary PGM furnace, circular or rectangular, operating at a power density above 190 kW/m^2.

Some basic design metrics of the rectangular furnaces are shown in Figure 10, namely ratios of length:width (L/W), electrode centre-to-matte-wall:electrode centre-to-slag-wall (M/S). The early installations had L/W ratios of 3.6 – 4.4, implying long and narrow furnaces. Impala discovered early that having the side walls too close to the electrodes was detrimental to side wall life (~5y) and quickly changed to a lower L/W ratio by widening their next installations from ratios of 4.4:1 to 3.4:1. This was more in line with the other rectangular furnace installations in the industry (range from 3.2:1 to 3.7:1), and the resultant furnace life was doubled (Watson, Harvey, 1992). RPM started changing L/W metrics when the furnaces were upgraded, which involved changes to refractory design, power input increase, and later changes in wall cooling technology. For all these furnaces, the M/S ratio was quite consistent (~0.75 to 0.9) other than for Polokwane, where the matte endwall was moved farther from the closest electrode in 2010 and increased the ratio to 1.45. One of the goals of the design change at Polokwane was to achieve a similar local-hearth-power-density to the smaller rectangular furnaces in the RPM fleet (Nelson et al., 2015), which also brought about a similar 'linear power density' (linear electrode face to wall power density in kW/m).

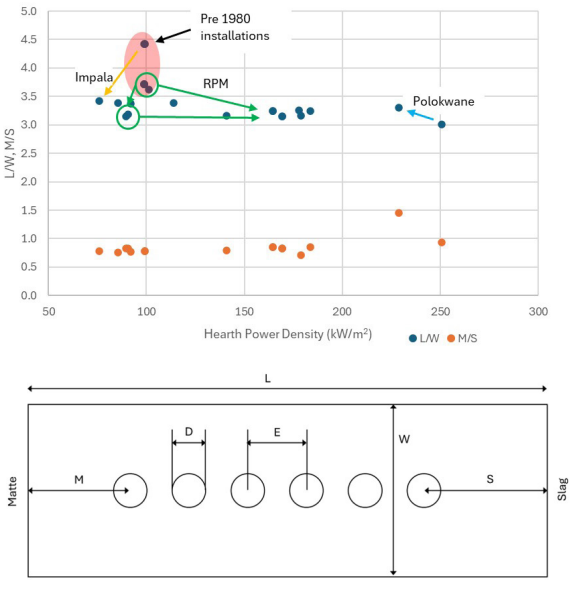

Figure 10—Rectangular furnace dimension metrics

Of note is that the diameter of the SSW circular furnace discussed earlier has recently been increased (Joubert et al., 2024; 2025) based on the linear power density metric proposed by Nelson et al. (2015). This has now enabled sustained operation of the furnace at > 15 MW.

The importance of adequate matte volume inside the furnace is a further dimensioning consideration (Nelson et al., 2015), where insufficient volume may yield higher matte temperatures and potential wear of hearth refractory by slag if the matte taphole elevation relative to the top of the hearth skewback brick is too low. For circular furnaces in particular, raising the matte taphole farther above the top of skewback brick, and thereby creating greater matte volume, has been demonstrated to be beneficial (Joubert et al., 2024; 2025).

Impact of furnace operating temperatures and intensities on hearth design

Prior to 1991, PGM electric furnaces with low power densities, converter slag recycle (containing magnetite), and chromium spinel accumulation experienced hearth build-ups, which were problematic (Watson, Harvey, 1992). This was despite the low solidus and liquidus temperatures of the primary furnace mattes. Given excess build-up in the earlier furnaces, hearth designs were relatively more insulating with the use of fireclay infill bricks and magnesite-chrome refractories in the upper and lower hearths.

As the furnace hearth power densities increased, and converter slag recycle was discontinued, build-up on the hearths no longer occurred. This is a key differentiator when compared to other commodities, where frozen heels are intentionally factored into the furnace design to promote hearth integrity, and maintaining the solidus isotherm within the upper hearth. With retention of the earlier insulating hearth designs at the time that furnace power, UG2 concentrate inputs, and matte temperatures increased, in addition to no build-up on the hearth, the matte solidus temperature isotherm moved well below the upper hearth. The implication was that liquid matte could infiltrate deep into the lower hearth and infill bricks (Figure 11). With thermal cycles on the furnace, ratcheting of the hearth occurred due to infiltration of liquid matte into brick joints, and contributed to continuous hearth growth, limiting the life of the hearth and allowing for hearth containment incidents (Shaw et al., 2014; Hundermark et al., 2020). The importance of furnace binding systems in minimising furnace growth is stressed by Watson and Harvey (1992), Shaw et al. (2014), and Nagorski et al. (2025).

With improved understanding of the importance of hearth thermal profiles associated with higher powered furnaces with no build-up, hearth refractory selection has improved. These changes aim to contain the matte solidus isotherm within the upper hearth refractories (Nagorski et al., 2025). Upper hearth refractories remain magnesite-chrome while the lower hearth refractory has changed from magnesite-chrome to more thermally conductive magnesite. Hearth infills have changed from the insulating fireclay to magnesite-based refractory, with an even higher conductivity silicon carbide infill trialled on one of the rectangular furnaces. Another circular furnace has no infill, with a dished hearth in use. Even with improved furnace hearth designs, the importance of furnace operating stability needs to be emphasised, with hearth growth being very sensitive to process and thermal cycling.

Converting

Survey information on converting in the Southern African PGM smelting industry is provided by Jones (1999; 2005), and the evolution of converting technology has been comprehensively reviewed by Nelson et al. (2018). A summary is provided in the following. With the change in primary smelting technology from blast furnaces to electric furnaces in the late 1960s, the quantity of furnace matte produced increased, and the converting technology was changed from Great Falls to Peirce Smith converters. The converting operations utilised by each PGM producer are as follows:

- RPM installed four 3.05 m × 6.1 m (~45 m^3 internal volume) converters in 1969 (Mostert, Roberts, 1973), the lengths of which were extended to 7.6 m (~56 m^3) in 1993, and two more converters of the enlarged dimensions were added in 1995 to bring the total to six converters, aligning with the increased furnace matte production requiring converting. These Peirce Smith converters were decommissioned in April 2004, following the successful ramp up of the top submerged lance (TSL) converting process.
- Impala Platinum installed three 3.05 m × 4.57 m (~33 m^3) converters in 1969 (Plasket, Ireland, 1976), later a fourth, and in 2000, added two larger converters of 3.66 m × 7.32 m (~77 m^3) (Coetzee, 2006).
- Lonmin (now SSW) installed two Peirce Smith converters in 1971 of 3.05 m × 4.57 m and later installed a third of the same dimensions in 2003 (Eksteen et al., 2011).
- Northam Platinum installed two Peirce Smith converters of 3.05 m × 6.1 m in 1992 (Jones, 1995).
- Zimplats operate two 3.05 m × 4.57 m Peirce Smith converters (Mabiza, 2006) and have recently installed two larger 3.66 m × 7.32 m converters (Crafford et al., 2025), in conjunction with the expansion of the primary smelting capacity with the addition of the new 38 MW furnace.
- Two 2t top blown rotary converters (TBRC) were utilised at Crocodile River briefly from 1989 to 1991 (Nelson et al., 2018).

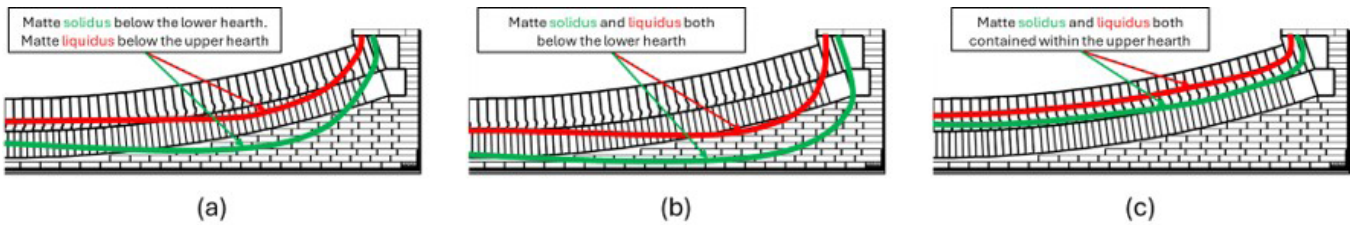

Figure 11—(a) Earlier insulating type hearth with Merensky concentrate and converter slag return; (b) Insulating hearth with increased UG2 and no converter slag return; (c) Current conductive hearth

Technology enhancements associated with the Peirce Smith converters include:

1. Use of flame optical emission spectroscopy (Bezuidenhout et al., 2017) for iron endpoint control.
2. Plant trials of sonic injection (Kapusta et al., 2012; Chibwe et al., 2015) were carried out on the SSW converters, however, to the authors' knowledge, the technology has not yet been adopted.

The evolution of the number of converters, their sizes (expressed as internal volume) and technologies for converting are summarised in the following (Figure 12).

Two factors determined the next evolution in converting technology, those being increased throughput requirements, and environmental emissions control of SO_2. With the expansion of production capacity at RPM in the late 1990s and early 2000s, particularly with the development of mines and concentrators on the eastern limb, Polokwane Smelter was commissioned in 2003 with the resultant Polokwane furnace matte requiring converting. From the mid-1990s RPM developed a new converting process based on Ausmelt TSL technology (now Metso). The Converter

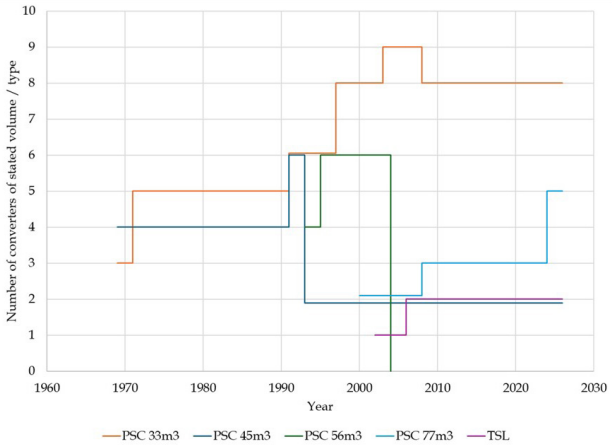

Figure 12—Evolution over time of the number of converters of specified internal volume and type

Plant (CP) was constructed adjacent to Waterval Smelter, and was commissioned in 2002 (Viviers, Hines, 2005), with a standby phase added in 2006. Novel technologies introduced in the converter included the use of deep-cooled waffle coolers in the slag zone of the crucible and a three-dimensional binding system (Figure 13). The CP receives solid matte feeds from each of the primary smelting operations and converts it to Waterval converter matte. The stationary TSL crucible allows for greatly improved off-gas capture compared to Peirce Smith converters and has enabled the facility to comply with the minimum emission standards for SO_2, with the use of a double contact acid plant. The benefit of a centralised converting facility enabled greater furnace matte throughput in a single vessel and reduced the number of converters and acid plants that would otherwise have been required, had Peirce Smith converting been retained.

Slag cleaning

Base and precious metals are lost to slag through entrained matte losses and oxidic losses. Entrained matte droplets in slag account for the bulk of the PGM losses. By contrast, the base metals may report to slag through both mechanisms, with the oxidic losses being highly dependent on the oxidation state in the process step in question.

In the primary furnaces, the extent of the PGM losses is dependent on the quantity of the matte collector phase (Nell, 2004) as a function of the probability of matte droplets colliding, coalescing, and disengaging (Nelson et al., 2005), and the quantity of slag generated. For concentrates with lower matte falls, there is a greater quantity of slag generated, and lower probability of matte droplets disengaging into the bulk matte layer. Base metal losses in the primary furnaces are governed by thermodynamic relationships between iron and base metal sulfides and iron and base metal oxides (Grimsey, 2021). With greater levels of iron reporting to slag in low matte fall concentrates (UG2), so the base metal recoveries decrease. Sakaran et al. (2024) have developed correlations of base metal recoveries as a function of feed composition, with clear differences observed depending on the predominant feed type to several primary smelting operations.

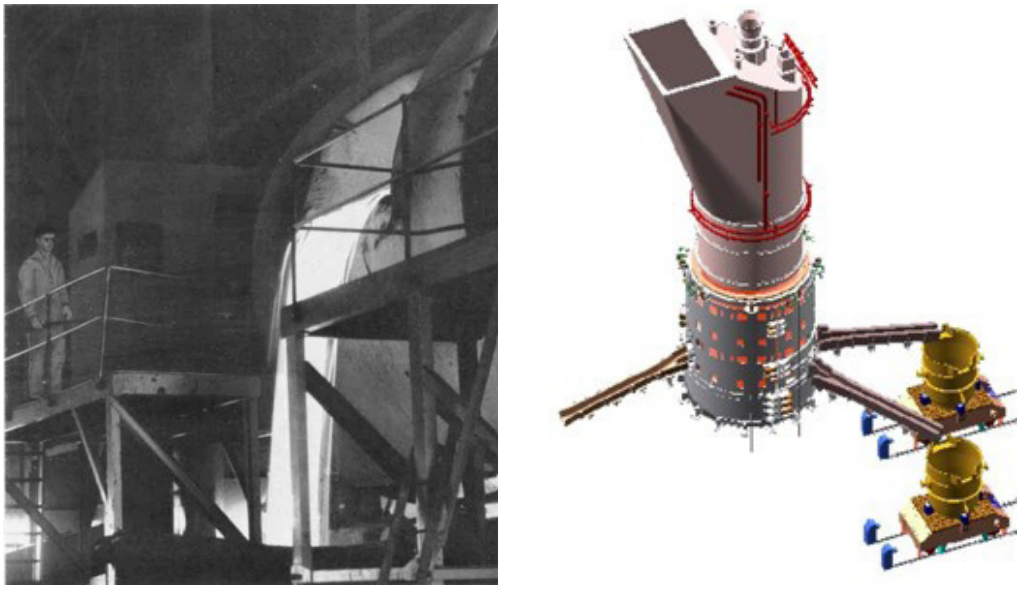

Figure 13—(left) Skimming slag from the Peirce Smith converter at Waterval (after Johnson Matthey, 1970); (right) 3D model image of the CP TSL (after Hoosen et al., 2018)

The approach to cleaning of primary furnace slags has typically been a function of the grade of the slag, and whether it is economic to clean the slag or to stockpile it. In more integrated operations where both primary smelting and converting takes place, and the historic practice of returning converter slag to the primary furnaces occurred, slag milling and flotation plants have mostly been installed. For smelting operations with primary furnaces only, in some cases the quantum of the slag losses has not justified the installation of a slag milling and flotation plant, and in other cases it has.

With more oxidising conditions present in converting, and the manner in which the matte and slag are separated through skimming in the case of Peirce Smith converters, the cleaning of converter slags is important for minimisation of losses. With the early Peirce Smith converter operations and Merensky concentrate feeds to the primary furnaces, the converter slag was traditionally returned to the primary furnaces. This practice contacted the oxidised converter slag with the incoming concentrate feed, allowing for reduction of the base metal oxides in the converter slag, and also the disengagement of mechanically entrained matte from the converter slag into the bulk matte layer in the primary furnace. This practice was discontinued by the South African industry players in the 1990s and early 2000s, as discussed earlier. For the Zimbabwean industry players, with the Great Dyke type concentrates having low Cr_2O_3 contents, return of converter slag to the primary furnace has continued (Mabiza et al., 2011; Crafford et al., 2025). In South Africa, cleaning of Peirce Smith converter slags therefore transitioned to milling and flotation, which allow for good recoveries of the entrained matte, but limited recovery of any base metal oxides. Given the batch nature of Peirce Smith converter operations, the 'slag blow' batches of slag should have relatively low oxidic losses, and it is only the final 'finishing blow' batch of slag that may have higher oxide losses.

For the RPM CP slag, the stationary crucible has two matte tapholes and one slag taphole, with tapping allowing for cleaner separation of the matte and slag, relative to skimming of Peirce Smith converters. However, the CP is operated in a continuous mode, and the converter slag is more oxidised, with higher base metal oxide losses as well as entrained matte droplets. For this reason, RPM installed a slag cleaning furnace (SCF) at the Waterval complex (Joubert et al., 2005; Jacobs, 2006), which was commissioned in 2003 in conjunction with the CP. The SCF is a circular, three electrode electric furnace of 12 m diameter, with 3 MVA × 10 MVA transformers. The nominal hearth power density of the furnace is 266 kW/m^2, although it is more typically operated in the range of 200 kW/m^2 – 220 kW/m^2, which is more intense than the other circular, primary furnaces. Deep-cooled copper coolers are installed in the slag zone of the furnace to allow for the higher sidewall heat fluxes associated with the high hearth power density on the furnace. Concentrate is added as a sulphur source and the MgO and SiO_2 assist in fluxing the FeO content in the converter slag. Metallurgical coke is added into the furnace for reduction of the base metal oxides. Due to the reductive smelting within the furnace, the matte produced is more alloy rich and so has a higher liquidus temperature (~1150 °C) relative to the primary furnace mattes. Matte is tapped at a temperature of ~1200 °C, and with the low superheat causing challenges with build-up in ladles and launders.

SO_2 abatement

The requirement to capture sulphur from smelter off-gas systems has been driven by the need to reduce impacts on ambient air quality, and by legislative requirements, with installations currently needing to comply with a defined emissions rate/limit based on the category definition of the operation. The selection of an abatement technology needs to consider the SO_2 concentration in the off-gas, as well as numerous project and operational factors, including capital and operating costs and effluent generation. Kruger (2004), Eksteen et al. (2011), and Ndlovu et al. (2023), describe approaches to evaluating the technologies available and how each is suited to the process conditions.

Early furnace off-gas cleaning focused on the removal of particulate matter from furnace off-gases. With increased production rates, leading to increased SO_2 concentrations in off-gas, companies moved towards the installation of SO_2 abatement technologies. In 1975, Impala Platinum commissioned the first single contact sulphuric acid plant in South Africa on a PGM operation, coupled with appropriate gas conditions stages for dust removal (Plasket, Ireland, 1976). RPM followed in 1976 with the installation of a single contact plant to treat Peirce Smith converter off-gas (Jacobs, 2006). These installations focused on the converter emissions as these are the highest concentration gases emitted on the smelter site (> 3 vol% SO_2). Impala Platinum performed further upgrades to the single contact plant in 2002 due to an increased number of converters installed (Coetzee, 2006).

Further increases in capacity and changes in concentrate origins caused primary furnace emissions to start increasing, both in mass load emissions and in concentrations. In particular, the significant increase in production throughputs at all of the PGM smelting operations in the Rustenburg region in the 1990s, necessitated a strong drive to improve environmental controls from each of the industry players. Consequently, SO_2 abatement equipment needed to be installed on the primary furnaces to manage ambient air quality. Fugitive emissions abatement was another important consideration to manage local ambient conditions around the smelting sites. Technologies used for primary furnace abatement were well suited to treating fugitive gases and therefore the duties could be combined (Wescott, 2007).

In 2002 RPM commissioned the converter plant (CP) at the Waterval facility. This change in process was accompanied by significant upgrades in gas cleaning technologies. A new single contact plant was installed to support the converter operation. Due to operational challenges experienced, described by Viviers and Hines (2005), the single contact plant was upgraded to a double contact double adsorption (DCDA) plant in 2005. In 2002 a novel Petersen-Fattinger Tower plant was also installed at Waterval to treat the primary furnace off-gas from both the primary furnaces. The Tower plant also treated the tailgas from the contact plant to manage final emissions to atmosphere. The Tower plant installation uses a nitric acid catalyst to remove SO_2 and produces a ~76% sulphuric acid product. Significant upgrades to the Tower plants materials of construction were also made to improve asset integrity during the same period. Significant work has been performed to better understand the materials and the maintenance of the plant, as described by Fouche (2017).

The installation of a second novel technology took place in 2002, with Impala installing a Sulfacid® plant to treat the primary furnace off-gas (Kruger, 2004). The technology relies on an activated carbon catalyst to produce a < 20% sulphuric acid product (Coetzee, 2006). Impala required further upgrades to its installed equipment to meet changed legislation and in 2009 commissioned two tailgas scrubbers based on MECS DynaWave® reverse-jet technology

(Impala Platinum Limited, 2025). The technology utilises wet lime-forced oxidation to produce a gypsum product and relies on the oxidation of calcium sulfite to calcium sulfate in the sump of the vessel to ensure the quality of the gypsum.

The first installations of wet scrubbing plants for SO_2 abatement purposes were also introduced in the early 2000s. In 2002, SSW (Lonmin at that time) installed a concentrated mode dual-alkali (CMDA) plant to treat the combined off-gas streams from the Peirce Smith converters and primary electric furnaces (Bezuidenhout et al., 2012). This system was selected due to its ability to handle large variations in off-gas flow and SO_2 strength and an intention to co-dispose the plant product (a combination of $CaSO_3$ and $CaSO_4$ referred to as $CaSO_x$) with the concentrator tailings, however, challenges were faced in disposing of the product. Options trialled included purpose-built dams and use in mine back fill and hazardous waste disposal, with the latter being practiced (Bezuidenhout et al., 2012). In 2003 RPM commissioned a wet lime scrubber for treatment of the SCF off-gas at Waterval. Significant operational challenges relating to scaling and choking of off-gas ducts necessitated the change from lime to sodium carbonate (soda ash) scrubbing, which significantly improved operations.

The next and latest technology implementation was the first installation of the Wet-gas Sulphuric Acid (WSA) technology at Valterra Platinum's Polokwane Smelter, which was commissioned in 2021 (Ndlovu et al., 2023). The plant uses the Topsoe technology to produce a > 96% sulphuric acid for sale into the market and was selected due to its low operating costs and minimal effluent production. Zimplats have also selected the WSA technology for implementation at the new expanded Selous Metallurgical Complex. Delays in approvals and construction indicate the plant could be operational by H2 2028 (Implats, 2025).

Risks and management

With the intensification of smelting processes, increasingly sophisticated controls have been introduced to manage the risks. Risk management in the PGM smelting operations is an extensive effort, which cannot all be covered in this paper; only the key issues will be covered here. Loss of containment and steam explosions caused by molten material interaction with water have historically been some of the highest consequence unwanted events in the smelting industry, and the PGM furnaces have been no exception to this. Exposure of people to the energies associated with these unwanted events results in life-threatening scenarios, which have been experienced and documented by the PGM smelting industry in various publications.

Slag granulation systems may be subject to steam explosions caused by improper process conditions. Water-slag ratios of 15:1, nozzle pressures of 550 kPa, water temperature, and launder design are listed as key variables for effective granulation as per Mostert and Roberts in 1973. These are also important today where increased automation is being used to measure these and other variables online and, in some cases, implement equipment and process interlocks to prevent unsafe conditions. Substitution of water by air in slag granulation was implemented at Northam in 2018 for converter slag (Hatch, 2018) and is being planned for implementation at the Mortimer Smelter in 2027. This has resulted in a step-change reduction in the risks associated with slag granulation. Northam have furthermore changed from wet slag handling on their primary furnace slags to dry slag handling (Northam, 2024).

In the design of the furnaces, two key factors that have impacted operational risks are high matte superheats and copper cooler corrosion. Smelting intensity has increased and process metallurgy has changed with higher MgO and Cr_2O_3 concentrations driving rising slag temperatures and, consequently, matte superheats (Shaw et al., 2014). The extreme matte superheat is a key differentiator for PGM smelting when compared to other industries (Table 1) and in addition, high thermal conductivity and convective heat transfer coefficients make the formation of reliable matte freeze linings practically unattainable. The implication is that copper coolers will melt in direct contact with PGM matte and therefore the reliance on competent refractory materials is essential to protect them in the matte zones of the furnace.

Despite the implemented design interventions, cooler failure and the resulting steam explosions continue to pose a significant hazard. The PGM smelting industry has adopted process safety management (PSM) principles, which provide a solid framework for managing these risks. However, practical challenges still arise, such as the reliance on procedural controls, gaps in process safety information, the complexity of hazard and operability study (HAZOP) and layer of protection analysis (LOPA) methods, and the difficulty of defining clear safe operating envelopes (Valiyev et al., 2025). Alongside the application of inherently safe design principles, enhanced monitoring and automation have formed a key component of the implemented approach.

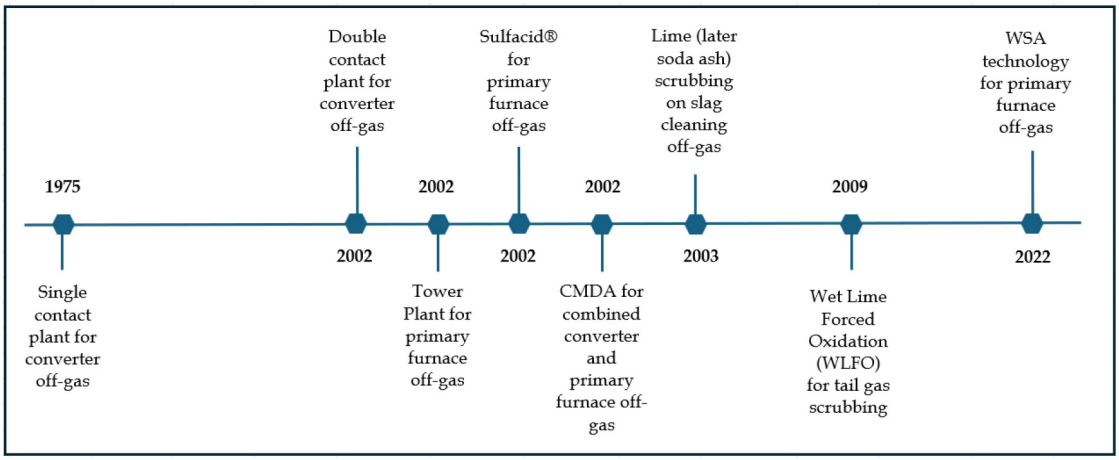

Figure 14—SO_2 abatement technology implementation timeline

Table 1

Matte superheat to solidus, ΔT = T*matte/metal* – T*solidus,matte/metal* (after Nelson and Schmidl, 2025)

		Ferrous		Ferrous - Base Metals					Non-ferrous				
		HC FeCr*	Ilmenite* - unspecified	FeNi - low-grade Ni	FeNi - mid-grade Ni	FeNi - high-grade Ni	FeNi - UHG Ni, high	Chambishi FeCuCo	Ni Matte Metallised*	Ni Matte*	NiCu PGM Matte*	Blister Cu*	Cu Matte*
Slag (S)	T_S [°C]	1825	1720	1550	1575	1600	1625	1500	1380	1350	1570	1320	1280
	$T_{S,\ liquidus}$ [°C]	1780	1680	1410	1484	1450	1575	1150	1190	1310	1450	1200	1180
	$\Delta T_{S\text{-}S,liquidus}$ [°C]	45	40	140	91	150	50	350	190	40	120	120	100
	$\Delta T_{(S\text{-}M)}$ [°C]	**125**	**170**	**100**	**90**	**160**	**175**	**175**	**110**	**180**	**90**	**40**	**100**
Matte/Metal (M)	T_M [°C]	1700	1550	1450	1485	1440	1450	1325	1270	1170	1480	1280	1180
	$T_{M,\ liquidus}$ [°C]	1675	1400	1220	1443	1405	1395	1330	1200	950	950	1080	1080
	$\Delta T_{M\text{-}M,liquidus}$ [°C]	25	150	230	42	35	55	-5	70	220	530	200	100
	$T_{M,\ solidus}$ [°C]	1460	1150		1430				730	650	650	660	660
	$\Delta T_{M\text{-}M,solidus}$ [°C]	240	400		55				540	520	830	620	520
	Comments	Very high T_S & T_M; low ΔT_S (even tap slag sub-liquidus) & ΔT_M; **Metal heel**	Very high T_S; low ΔT_S (even tap slag sub-liquidus); **Metal heel**	High T_S; high ΔT_M; **Metal heel, startup flotation**	High T_S; low ΔT_M; **4 penetrated furnace hearths if inadequate Metal heel**	High T_S; low ΔT_M; **Metal heel**	High T_S; low ΔT_M; **Metal heel**	High ΔT_S & low ΔT_M (even tap sub-liquidus); **Metal heel**	Low TS & TM; lower ΔTM; **Floated hearth**	Low TS & TM; **Floated hearth**	High TS & TM; high ΔTS; very high ΔTM; **Floated hearth**	Low TS but higher TM; high ΔTM; **Speiss Floated hearth**	Low TS & TM; high ΔTM; **Speiss Floated hearth**

Monitoring systems have been developed as a means to detect abnormal conditions and water leaks. Simple point temperature monitoring to measure copper and water temperatures has long been employed to detect unexpected heat flux conditions. These methods are limited in their ability to detect localised problems. In the early 2000s, the use of fibre optic lines cast into the copper element was first used, which would detect the highest temperature along its length and indicate imminent failure (Sakaran et al., 2018; Van Beek et al., 2014; Hopf, Rossouw, 2006). Leak detection methods have been deployed, which use automated pressure testing and more recently, continuous tundish level monitoring. Both methods have proven to be sufficiently reliable and sensitive in detecting actual water leaks. Measurement of moisture in the off-gas to detect water leaks using tuneable diode laser absorption spectroscopy (TDLAS) has been used at the Valterra Platinum converter (Govindsamy et al., 2021) and will also be installed at the slag cleaning furnace. Advanced statistical methods have been developed where 'event detection' monitors the trends of the online instrumentation (e.g., temperatures) and identifies deviations from history using principal component analysis (PCA) (Groenewald, 2018). There are two legs to the PCA-based technique; the first detects sharp/sudden changes while the second detects drifts. System errors or events detected are communicated to the operations staff. It was first trialled on the matte wall and tap blocks at Polokwane and quickly proved to be highly reliable as well as sensitive in detecting deviations. It has since then been rolled out to include all walls and hearths of all Valterra Platinum furnaces.

Separation of people from the hazards has required significant automation. Measurement of top of furnace feed level using radar (Hundermark et al., 2018) has proven successful in multiple instances but is not yet widely used. Automated sounding systems to obtain buildup, matte, and slag levels are currently being trialled by various operations (Goff et al., 2011). The combination of these two technologies would remove the operator completely from the furnace roof where they are currently still required to perform soundings. On the tapping floor, the replacement of hand-held pyrometers with online thermal cameras led to a 21% reduction in exposure of the operator to the open taphole while offering real-time continuous temperature measurement of the tapping process (Sanker Jawohir et al., 2022). As early as 1969, the first electric furnaces at RPM made use of clay guns to close the matte and slag tap holes (Mostert, Roberts, 1973). Subsequently, tap hole drilling and plugging machines have become more powerful and sophisticated, allowing more consistent drilling open, without damaging the refractories, and more reliable plugging (Dienenthal, 2014). Alternatives to drilling and plugging machines have proven impracticable and this remains best practice in the PGM smelting industry. Use of emergency systems for tapping operations have improved: push buttons have allowed closure of cooling water supply and air purge to matte taphole face plates in the event of damage (Van Beek et al., 2014). A hydraulically actuated slag shut-off valve has been implemented as an alternative to closing the slag hole with a clay gun in emergencies (Essack, 2014). Emergency water granulation systems have been installed, which provide back-up gravity-fed water in the event of supply failure by pumps. Further separation of people from the hazards has been achieved by using remotely located control rooms. State-of-the-art facilities, as implemented at all the Valterra Platinum smelters, utilise in-plant cameras in critical areas, which provide visibility for operators.

Operational best practices have proven important in managing risk where operation within the design envelope is proceduralised via 'smelting rules' and stable power control is prioritised over stock management. Furthermore, routine maintenance interventions are planned such that vulnerable areas of the furnace are replaced prior to potential failure. Historically 'cold shuts' were performed and in 2009 the first 'hot shut' was implemented at Polokwane where low power inputs were maintained during furnace wall replacement, which prevented a deep thermal cycle and considerably reduced the ratchet on the hearth (Snodgrass et al., 2024).

Conclusion

Significant technological advances have been made in the PGM smelting industry across all unit operations including drying, primary smelting, converting, slag cleaning, off-gas handling, and

risk management. These have resulted in improved safety, better efficiencies, and reduced costs.

With the outlook in demand for PGMs changing as a function of automotive demand requirements, smelting technology will need to continue to evolve. Existing challenges, which require future work include:

- Mitigation of copper corrosion of other copper coolers above and below the main slag-concentrate zone, where corrosion rates are considerably slower, however, still limit component campaign lives, where components are reused. Examples of such coolers are upper plate coolers (above the slag zone), matte tap blocks and flanker coolers.
- Further enhancements are required to improve electrical energy efficiencies, with the cost of electricity being a major contributor to overall smelting costs. Increased use of renewable sources to power the smelting operations will aid in reducing Scope 2 emissions.
- More cost-effective technology solutions for SO_2 abatement are required. With the possibility of further tightening of legislation, increased production, changes in feed metallurgy, technology advancements are required, which may further improve SO_2 capture efficiency, reduce capital and operating costs, and generate saleable byproducts.
- Further automation around the molten materials environment is required to improve engineering controls and further remove personnel from proximity to the hazards.

Acknowledgments

The authors wish to thank Valterra Platinum for permission to publish this paper.

References

Anglo American Platinum. 2016. Anglo American Site Visit: Processing and Polokwane Smelter. https://www.angloamerican.com/~/media/Files/A/Anglo-American-Group/PLC/media/presentations/2016pres/anglo-american-site-visit-processing-and-polokwane-smelter-241116-v2.pdf [accessed 2026-02-08].

Beath, C.B., Cousins, C.A., Westwood, R.J. 1961. The exploitation of the Platiniferous Ores of the Bushveld Igneous Complex with Particular Reference to the Rustenburg Platinum Mines, V*IIth CMMI Congress (Johannesburg: South African Institute of Mining and Metallurgy)*, pp. 238—241.

Bruce, J.T. 1996. Rustenburg and Johnson Matthey, An Enduring Relationship. *Platinum Metals Review,* vol. 40, no. 1, pp. 2—7.

Bezuidenhout, G.A., Eksteen, J.J., Akdogan G., Van Beek, B., Wendt, W., Persson, W. 2017. Implementation of flame optical emission spectroscopy system for converter Fe end-point control associated with Ni-Cu-S-PGM converter mattes. *Minerals Engineering*, vol. 100, pp. 132—143.

Bezuidenhout, G.A., Davis, J., Van Beek, B., Eksteen, J.J. 2012. Operation of a concentrated mode dual-alkali scrubber plant at the Lonmin Smelter. *Journal of The Southern African Institute of Mining and Metallurgy*, vol. 112, pp. 657—665.

Cheng, F., Zhou, X.,Liu, Y. 2018. Methods for improvement of thermal efficiency during spray drying. *E3S Web of Conferences* vol. 53, pp. 01031.

Chibwe, D.K., Akdogan, G., Bezuidenhout, G.A., Kapusta, J.P.T., Bradshaw, S., Eksteen, J.J. 2015. Sonic injection into a PGM Peirce-Smith converter: CFD modelling and industrial trials. *Journal of The Southern African Institute of Mining and Metallurgy*, vol. 115, May, pp. 349—354.

Coetzee, V. 2006. Common-Sense Improvements to Electric Smelting at Impala Platinum. *Southern African Pyrometallurgy 2006, South African Institute of Mining and Metallurgy, Johannesburg*, March, pp. 43—62.

Crafford, M., Monobe, M., Erasmus, G., Matutu, S. 2025. Commissioning of the Zimplats Smelter expansion. 9th *International PGM Conference. Southern African Institute of Mining and Metallurgy, Rustenburg*, October, pp. 185—197.

Cramer, L.A. 2001. *The extractive metallurgy of South Africa's platinum ores*. JOM. pp. 14–18.

Dienenthal, A. 2014. A short history of the development of tapping equipment. *Proceedings of the Furnace Tapping Conference 2014. Southern African Institute of Mining and Metallurgy*, pp. 203—216.

Eksteen, J.J., Van Beek, B., Bezuidenhout, G.A., 2011. Cracking a hard nut: An overview of Lonmin's operations directed at smelting of UG2-rich concentrate blends. *Southern African Pyrometallurgy 2011*, edited by R.T. Jones & P. den Hoed, *Southern African Institute of Mining and Metallurgy, Johannesburg*, March, pp. 231 – 252.

Forbes, J.E. 1977. Oxygen enrichment of the converter air at Rustenburg Platinum Mines. *Journal of the South African Institute of Mining and Metallurgy*, vol. 77, no. 6, pp. 132—136.

Fouche, P.M. 2017. An example of the use of advanced fibre-reinforced plastics in sulphuric acid plants. *The Journal of the South African Institute of Mining and Metallurgy,* vol. 117 no.11, pp. 1023 – 1029.

Goff, T.J., Brogden, N., Nilsson, J.P., Bloemer, P., Lyons, A. 2011. 'Implementation of an alternative matte-level measurement solution at Lonmin Marikana Smelter Division for improved process monitoring', *Proceedings of the SAIMM Pyrometallurgy 2011 Conference*, Johannesburg, South Africa, 9-10 March 2011. *The Southern African Institute of Mining and Metallurgy*, pp. 269 – 278.

Gouldsmith, A.F.S., Wilson, B. 1963. Extraction and Refining of the Platinum Metals, A complex cycle of smelting, electrolytic and chemical operations. *Platinum Metals Review*, vol. 7, no. 4, pp. 136—143.

Govindsamy, D., Georgalli, G.A., Hoosen, A. 2021. Leak detection at Anglo Platinum Converting Process using Digital Twins. IFAC *PapersOnLine* 54-21 (2021), pp. 192 – 197.

Grimsey, E.J. 2021. A comparison of two novel non-ferrous metal recovery equations: Development similarity and industrial significance. *Metallurgical and Materials Transactions B*. vol. 52 no. 5, pp. 2817—2820.

Groenewald, J.W.D., Nelson, L.R., Hundermark, R.J., Phage, K., Sakaran, R.L., Van Rooyen, Q., Cizek, A. 2018. Furnace integrity monitoring using component analysis: an industrial case study. *The Journal of the South African Institute of Mining and Metallurgy*, vol. 118, no. 4, pp. 345—352.

Hatch, 2018. Website article: Northam Converter Dry Slag Granulation. https://www.hatch.com/Projects/Metals-And-Minerals/Northam-Converter-Dry-Slag-Granulation

Hochreiter, R. C., Kennedy, D. C., Muir, W., Woods, A. I. 1985. Platinum in South Africa (Metal Review Series no. 3). *Journal of the South African Institute of Minerals and Metallurgy*, vol. 85 no. 6, pp. 165—85.

Hopf, M., Rossouw, E. 2006. New Opportunities – Exhaustive Monitored Copper Coolers for Submerged Arc Furnaces. *Southern African Pyrometallurgy 2006 International Conference, Cradle of Humankind, South Africa*, 5–8 March 2006. pp. 89—100.

Hoosen, A., Sichone, M., Rambiyana, I. 2018. Improvements to the Anglo Converting Process (ACP) tap-block management. *Furnace Tapping 2018*. Edited by J.D. Steenkamp and A. Cowey, *Southern African Institute of Mining and Metallurgy*, pp. 49—56.

Hundermark, R.J., Nelson, L.R. 2014. Redoubling platinum group metal smelting intensity – operational challenges and solutions. *Proceedings of EPD Symposium in Honor of David G.C. Robertson*, TMS, San Diego, CA, pp. 189 —96.

Hundermark, R., Van Rooyen, Q., Van Manen, P., Steyn, C., Sadri, A., Chataway, D. 2018. Development of Continuous Radar Level Measurement for Improved Furnace Feed Control. *Proceedings of Extraction 2018*. The Minerals and Metals Society, 2018. pp. 287 – 302.

Hundermark, R.J., Nelson, L.R., Berger, B. 2020. Thermal conductivity measurements of solid mattes containing Fe-S-Ni-Cu-Co from 100-450°C. *The 11th Molten Slags, Fluxes, and Salts [MOLTEN 2020]*, Seoul, Korea, May.

Implats. 2025. Annual Integrated Report. https://www.implats.co.za/pdf/annual-reports/annual-integrated-report/2025/integrated-report-2025.pdf

Jacobs, M. 2006. Process Description and Abbreviated History of Anglo Platinum's Waterval Smelter. *Southern African Pyrometallurgy 2006*, South African Institute of Mining and Metallurgy, Johannesburg, March, pp. 17—28.

Johnson Matthey. 1969. Platinum Mining at Rustenburg, Growth of the World's Largest Producer. *Platinum Metals Review*, vol. 13, no. 1, pp. 15 – 22.

Johnson Matthey. 1970. New Electric Smelter at Rustenburg, A further stage in the expansion programme. *Platinum Metals Review*, vol. 14, no. 2, pp. 48 —49.

Jones, R.T. 1999. Special issue on Platinum in South Africa to commemorate the 75th anniversary of the discovery of the Merensky Reef. *South African Journal of Science*. vol. 95, November/December, pp. 525—534.

Jones, R.T. 2005. An overview of Southern African PGM smelting. *Nickel and Cobalt 2005 Challenges in Extraction and Production*. 44th Annual Conference of Metallurgists of CIM. Calgary, pp. 147—178.

Joubert, H., Nourse, R.B., Masters, B., Hundermark, R.J. 2005. Copper cooling design, installation and operational results for the slag cleaning furnace at Waterval Smelter, Rustenburg Platinum, South Africa. *Nickel and Cobalt 2005 Challenges in Extraction and Production*, Edited by J. Donald and R. Schonewille, 44th Annual Conference of Metallurgists of CIM, Calgary, Alberta, Canada pp. 19—35.

Joubert, H., De Villiers, G., Mbedzi, P., Davis, J. 2024. Composite Copper-Graphite Cooler for PGM Furnace Sidewall. *Advances in Pyrometallurgy*, G. Alvear et al. (eds.), The Minerals, Metals and Materials Society, pp. 51—65.

Joubert, H., De Villiers, G., Nel, J., Senekal, D., Mbedzi, P., Davis, J. 2024. PGM furnace crucible upgrade and performance. *Southern African Pyrometallurgy 2024*, Johannesburg, South Africa, March 2024, pp. 221 – 234.

Joubert, H., De Villiers, G., Nkosi, P., Mokgwamme, E. 2025. PGM furnace crucible performance following design upgrade. *Ni-Co 2025, 6th International Symposium on Nickel and Cobalt*, pp. 875—889.

Kapusta, J.P.T., Davis, J., Bezuidenhout, G.A., Lefume, S., Chibwe, D.K. 2012. Industrial evaluation of sonic injection in a Peirce-Smith converter at the Lonmin Platinum Smelter. *Towards Clean Metallurgical Processing for Profit, Social and Environmental Stewardship*. Proceedings of the 51st Annual Conference of Metallurgists. Niagara Falls, pp. 43—58.

Kemp, I.C. 2012. Fundamentals of Energy Analysis of Dryers. *Modern Drying Technology, Volume 4*: Energy Savings, Edited by Tsotsas, E. and Mujumdar, A. S., 1st edn. Weinheim: Wiley-VCH, pp. 1—32.

Kruger, B. 2004. Recovery of SO2 from low strength off-gases. *International Platinum Conference 'Platinum Adding Value'*. The South African Institute of Mining and Metallurgy, Sun City, South Africa, 3–7 October. Johannesburg, pp. 37—46.

Mabiza, L. 2006. An overview of PGM smelting in Zimbabwe – Zimplats Operations. *Southern African Pyrometallurgy 2006, South African Institute of Mining and Metallurgy*, Johannesburg, March, pp. 63—76.

Mabiza, L., Picas, R., Nell, J., Matsetela, B., Erasmus, G. 2011. Characterisation of SO2 in offgas at Zimplats smelter. *Southern African Pyrometallurgy 2011*, Edited by R.T. Jones and P. den Hoed. Southern African Institute of Mining and Metallurgy, Johannesburg, March, pp. 161 —171.

Merkle, R.K.W., McKenzie, A.D. 2002. The Mining and Beneficiation of South African PGE ores – An Overview. *The Geology, Geochemistry, Mineralogy and Mineral Beneficiation of Platinum-Group Elements*. Edited by Cabri, L.J., Special Volume 54. Montreal: Canadian Institute of Mining, Metallurgy and Petroleum, pp. 793 – 810.

Mostert, J.C., Roberts, P.N. 1973. Electric smelting at Rustenburg Platinum Mines Limited of nickel-copper concentrates containing platinum-group metals. *Journal of the South African Institute of Mining and Metallurgy*, April, 290—299.

Nagorski, M., Van der Merwe, M., Mulder, G., DeGorter, M., Kingsley, T. 2025. Factors influencing campaign life of PGM furnace hearths. *9th International PGM Conference*. Southern African Institute of Mining and Metallurgy, Rustenburg, October, pp. 117—128.

Nell, J. 2004. Melting of platinum group metal concentrates in South Africa. *Journal of the South African Institute of Mining and Metallurgy*, vol. 104, (no. 7, pp. 423—428.

Nelson, L.R., Stober, F., Ndlovu, J., De Villiers, L.P.vS., Wanblad, D. 2005. Role of technical innovation on production delivery at the Polokwane Smelter. Nickel and Cobalt 2005: Challenges in Extraction and Production. *44th Annual Conference of Metallurgists*, Calgary, Alberta, Canada, August. pp. 91—116.

Nelson, L.R., Hundermark, R.J., Van der Merwe, K. 2015. Observations on the impact of furnace dimensioning and power density on tap-hole integrity. *The 54th Annual Conference of Metallurgists (COM2015)*, CIM, Toronto, August.

Nelson, L.R., Georgalli, G.A., Hines, K.L, Hundermark, R.J. 2018. Converter processing of platinum group metals, *Mineral Processing and Extractive Metallurgy,* DOI: 10.1080/25726641.2018.1506272.

Nelson, L.R., Schmidl, J. 2025. Short Course: Pyrometallurgical Processes in Copper and Nickel/Cobalt Extraction: Furnace Integrity, *Extraction 2025, Phoenix,* AZ.

Ndlovu, M., Marsden, G., Bezuidenhout, J., Hundermark, R., Erasmus, G. 2023. SO2 abatement at the Polokwane Smelter – The project and the process'. *The 8th Sulphur and Sulphuric Acid Conference 2023*. The Southern African Institute of Mining and Metallurgy Cape Town, March, pp. 1—3.

Northam. 2024. Summarised Financial Results, 30 June 2024.

Rivera Li Kao, O., Garbers-Craig, A. 2025. Decomposition of sulfide phases and subsequent matte collection in the black top of a Platinum Group Metal smelter. *Mineral Processing and Extractive Metallurgy Review*, vol. 46, (no. 5), pp. 616—625.

Plasket, R.P., Ireland, D.A. 1976. Ancillary smelter operations and sulphuric acid manufacture at Impala Platinum Limited. *Journal of the South African Institute of Mining and Metallurgy*, August, pp. 1 – 10.

Sakaran, R. L., Van Rooyen, Q., Van Manen, P. K., Mukumbe, P.P. 2018. Analysis and interpretation of fibre optic temperature data at the Polokwane Smelter. *Journal of the Southern African Institute of Mining and Metallurgy,* vol. 118 (no. 4), pp. 337–344.

Sakaran, R.L., Le Roux, J.D., Garbers-Craig, A.M. 2024. The impact of feed composition on the recovery of base metals in an electric furnace. Southern African Pyrometallurgy 2024. *Southern African Institute of Mining and Metallurgy*, Johannesburg, pp. pp. 321 – 334.

Sanker Jawohir, A., Van der Merwe, K., Potgieter, H.P. 2022. Replacement of hand-held pyrometers with on-line thermal cameras on the tapping floor. *Proceedings of the 8th International PGM Conference. The Southern African Institute of Mining and Metallurgy*. Sun City, November. pp. 87—97.

Sarvinis, J., De Vries, S., Joiner, K., Van Mierlo, C., Voermann, N. 1999. Improvements to BHP Hartley Platinum's Smelting Furnace. *Proceedings of the Copper 99 – Cobre 99 International Conference: Vol. V. Smelting Operations and Advances.* Phoenix, Arizona, USA, 10–13 October. Warrendale, PA: The Minerals, Metals & Materials Society (TMS), pp. 235—250.

Shaw, A., De Villiers, L.P.vS., Hundermark, R.J., Ndlovu, J., Nelson, L.R., Pieterse, B., Sullivan, R., Voermann, N., Walker, C., Stober, F., McKenzie, A.D. 2014. Challenges and Solutions in PGM Furnace Operation: High Matte Temperature and Copper Cooler Corrosion, *Journal of the Southern African Institute of Mining and Metallurgy*, vol. 113, no. 3, pp. 251—261.

Snodgrass, R., Marsden, G., Van der Merwe, K., Shoko, S. 2024. Recent developments at Anglo American Platinum's smelting operations. *Southern African Pyrometallurgy 2024*. Southern African Institute of Mining and Metallurgy, Johannesburg, March, pp. 207 – 224.

Valiyev, A., Hines, K., Maharaj, J., Laher, I. 2025. Fahrenheit 3214: PSM in Electric Furnace Smelting Operations - Challenges and Opportunities, *Proceedings of the 2025 AIChE Spring Meeting and 21st Global Congress on Process Safety. Houston*, TX, 6–10 April.

Van Beek, B., Goff, T.J., Nel, P.E., Rex, E. 2014. An overview of the design, operation, and maintenance practices relating to tap-hole management on a PGM smelting furnace. *Journal of the Southern African Institute of Mining and Metallurgy*, vo. 116, no.1, pp. 27 —34.

Viviers, P., Hines, K. 2005. The new Anglo Platinum Converting Project. *First Extractive Metallurgy Operators' Conference*. Brisbane, Australia, 7–8 November. Carlton, Victoria: Australasian Institute of Mining and Metallurgy (AusIMM), pp. 1 – 8.

Watson, G.B., Harvey, B.G. 1992. A common-sense approach to process improvements to electric smelting of nickel-copper concentrates at Impala Platinum. *Proceedings of the International Symposium on Non-ferrous pyrometallurgy*. The Metallurgical Society of CIM. Edmonton. pp. 289—304.

World Platinum Investment Council (WPIC). 2026. Supply and Demand historical data. https://platinuminvestment.com/supply-and-demand/historic-data [accessed 14 January 2026 ◆

Impact of feed mixture control on arc behaviour in direct-current arc furnace smelting of chromite – a modelling study

by Q.G. Reynolds,[1,2], M.W. Erwee[3], S. Swanepoel[3], R. Fourie[3]

Affiliation:
1 Pyrometallurgy Division, Mintek, Johannesburg, South Africa
2 Stellenbosch University, Stellenbosch, South Africa
3 Samancor Chrome Ltd, Johannesburg, South Africa

Correspondence to:
Q.G. Reynolds

Email:
quinnr@mintek.co.za

Dates:
Received: 19 May. 2026
Published: July 2026

How to cite:
Reynolds, Q.G., Erwee, M.W., Swanepoel, S., Fourie, R. 2026. Impact of feed mixture control on arc behaviour in direct-current arc furnace smelting of chromite – a modelling study. *Journal of the Southern African Institute of Mining and Metallurgy*, vol. 126, no. 7, pp. 427 – 434

DOI ID:
https://doi.org/10.17159/2411-9717/1105/2026

ORCiD:
Q.G. Reynolds
https://orcid.org/0000-0002-5196-8586
M.W. Erwee
https://orcid.org/0000-0001-5067-3439
S. Swanepoel
https://orcid.org/0000-0001-5067-3439
R. Fourie
https://orcid.org/0009-0008-3503-0513

This paper is based on a presentation given at the SAIMM Pyrometallurgy International Conference 2026, 26-28 May 2026, CSIR International Convention Centre, Pretoria, South Africa

Abstract

Unexpected excursions in electrode hoist position are occasionally observed on direct-current arc furnace plants producing ferrochromium, and are not readily explained by changes in electrical power supply or known process disturbances. One possible mechanism for this is variations in feed reductant balance altering the freeboard gas composition and, hence, the thermophysical properties of the arc plasma, changing the arc's effective electrical resistance. This hypothesis is investigated using an integrated computational modelling workflow comprising thermochemical equilibrium simulations in FactSage, plasma property calculations using the open-source minplascalc tool, and magnetohydrodynamic arc simulations using the open-source plasmaArc solver. Three reductant balance conditions were examined across a range of effective slag temperatures. Results show that while the reductant balance does influence freeboard gas composition and certain plasma properties (particularly electrical conductivity and radiation emission coefficient when lower slag temperatures are considered), these two effects act in opposing directions and largely cancel one another. Arc voltages and resistances are consequently not significantly different between reductant conditions. It is concluded that variations in feed reductant balance are unlikely to be the primary cause of the observed hoist excursion events via this mechanism, and directions for future investigation are proposed.

Keywords

pyrometallurgy, ferrochromium, plasma, modelling.

Introduction

Chromium is a critical mineral in South Africa, which harbours most of the world's known ore reserves. It is used primarily as an alloying agent in the manufacture of stainless steel and other specialised metal products. The majority of the chromium supply worldwide is produced as a ferrochromium (FeCr) alloy by carbothermic reductive smelting of chromite ore in electric furnaces (Gasik, 2013; Jones, 2014).

Contemporary pyrometallurgical processes for FeCr production use blended carbonaceous reductants, typically fossil metallurgical coke, coal, and/or anthracite, as a reducing agent and produce significant scope-1 CO_2 emissions. Reducing the carbon footprint of the alloy product is desirable, and several new concepts for low-carbon FeCr production are under investigation. These include the use of plasma-state hydrogen (Dalaker, Hovig, 2023) or light metals (Akhmetov et al., 2025) as replacements for carbonaceous reductants. Many of these concepts are however still at early stages of development, and it is argued by some that carbonaceous reductants from biological sources can be used to achieve carbon-neutral smelting more rapidly and without radical changes to existing furnace designs or process chemistry (Sommerfeld et al., 2024). It is therefore likely that carbothermic smelting in some form will continue to be used for FeCr production in the post-decarbonisation landscape, and studies of such processes remain relevant.

Open arc, open bath direct-current (DC) plasma arc furnace technology is particularly well-suited to chromite smelting due to its ability to handle fine feed materials and high temperatures (Jones, 2014; Oterdoom et al., 2025; Sager et al., 2010). DC furnaces consist of a closed cylindrical crucible, which contains the process material, and one or more graphite electrodes entering through the vessel roof. An electric arc is formed between the electrode tip and the surface of the molten bath below it. The plasma arc is a sustained electrical discharge, which transfers thermal and mechanical energy to the molten bath, which in turn drives the thermochemistry of the reduction process (Boulos et al., 2023; Bowman, Krüger, 2009). Chromite ore and carbonaceous reductants such as metallurgical coke are fed to the furnace together with fluxes and chemical modifiers, producing a waste slag and the FeCr-product alloy.

Impact of feed mixture control on arc behaviour in direct-current arc furnace smelting

For optimal metallurgical performance, electrical control of DC furnaces is important to ensure that open arc operation and correct power input to the process are maintained at all times (Geldenhuys, 2017). This is generally accomplished by a series of nested control loops, the outermost of which moves the electrode hoist up or down to meet a desired furnace voltage or resistance setpoint (Sager et al., 2010). Even with such control measures, large variations in hoist position are sometimes observed on furnace plants and would seem to indicate sudden changes in the effective resistance of the furnace.

An example of this can be seen in data obtained from an industrial FeCr DC furnace plant shown in Figure 1. The period displayed is the time between electrode section additions and covers approximately 10 taps. It can be seen that although the furnace current and voltage are being controlled close to their setpoints, there is a considerable degree of variation in the hoist position, which is a proxy for the arc length inside the furnace. The nett downward trend through the period is expected due to electrode erosion, which occurs at a constant rate at fixed power and current (Kjellberg, Stenkvist, 1989), but the intermittent movements of the hoist up or down (some examples are highlighted with the red arrows) can be rapid and significant. These excursions are not accounted for by changes in the electrical power supply, nor do they appear to correlate with known process disturbances such as furnace tapping or feed interruptions.

Possible explanations for such behaviour are slag foaming events, collapse of feed banks, electrode damage or breakage, sudden changes in process chemistry, power/feed imbalances, and others. The mechanisms by which these could affect the furnace resistance include altering the chemical composition or temperature of the slag bath, changing the geometry of the bath or electrode, or changing the gas composition in the freeboard space (and hence, the electrical properties of the arc plasma).

In this paper, the authors apply an integrated arc modelling workflow comprising thermochemistry simulations, plasma property calculations, and computational multiphysics models of the plasma arc to study process chemistry variations and their effect on freeboard gas composition as a possible explanation for these events. The impact of over- or under-feeding reductant for a given FeCr feed mixture is examined for the case of a representative industrial-scale DC furnace, and the results are discussed in terms of their effect on the electrical behaviour of the arc.

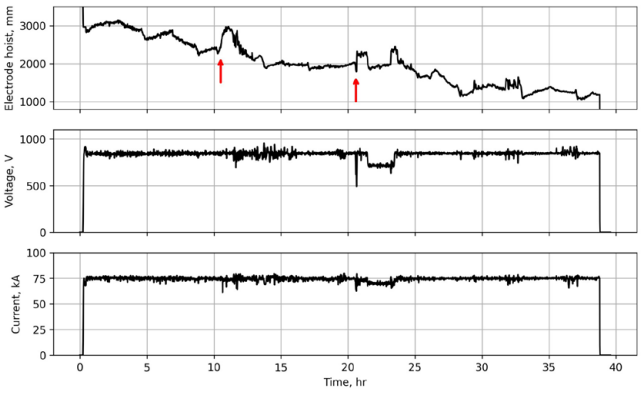

Figure 1—Hoist position and electrical measurements from a DC furnace producing FeCr (red arrows indicate start of hoist excursion events)

Description of modelling workflow

The plasma arc in a DC arc furnace is a high-velocity (km/s), high-temperature (10,000 K) jet sustained by electromagnetic forces acting on thermally ionised gas in the freeboard space above the molten bath. Its ability to conduct electrical current and transfer large quantities of mechanical and thermal energy to the bath makes it the primary energy delivery mechanism of the furnace, and understanding its behaviour is central to the effective operation of DC arc furnace processes (Bowman, Krüger, 2009; Geldenhuys, 2017).

The extreme operating conditions of large-scale metallurgical arcs limit direct experimental characterisation in most cases. Computational modelling provides a practical alternative, and modern approaches have advanced to the point where integrated workflows can account for the effect of metallurgical chemistry on plasma gas composition, and consequently on the thermophysical properties of the plasma (Reynolds et al., 2025a). The modelling workflow employed in the present study consists of three separate steps:

- The first step in the workflow uses the FactSage thermochemical simulation tool (Bale et al., 2016) to compute multiphase thermodynamic equilibria for the process under consideration. Equilibrium calculations were performed using appropriate alloy, oxide, and ideal-mixture gas databases, with feed material composition and process temperature as inputs, yielding the species composition of the gas phase.
- The freeboard gas compositions were then passed to minplascalc (Reynolds et al., 2025b), an open-source plasma property calculator, which determines equilibrium plasma compositions via Gibbs free energy minimisation and computes thermodynamic (density, enthalpy, heat capacity) and transport (viscosity, electrical conductivity, thermal conductivity, radiation emission coefficient) properties as functions of temperature at atmospheric pressure. The resulting property data are stored in lookup-table format for use in subsequent calculations.
- Finally, the plasma property data is used in plasmaArc (Reynolds, 2026), an open-source computational multiphysics solver implemented within the OpenFOAM® framework (OpenCFD Ltd, 2025) to compute the spatial and temporal evolution of the arc. The solver uses a finite-volume formulation on unstructured meshes to calculate numerical solutions to the coupled magnetohydrodynamic (MHD) governing equations describing fluid flow (Equation 1), energy transport (Equation 2), and the electromagnetic field (Equation 3):

$$\frac{\partial}{\partial t}(\rho\mathbf{u}) + \nabla\cdot(\rho\mathbf{u}\otimes\mathbf{u}) + \nabla P = \nabla\cdot\boldsymbol{\tau}_{\mathrm{ij}} + \mathbf{j}\times \qquad [1]$$
$$\frac{\partial\rho}{\partial t} + \nabla\cdot(\rho\mathbf{u}) = 0$$

$$\frac{\partial}{\partial t}(\rho h) + \nabla\cdot(\rho\mathbf{u}h) = \nabla\cdot(\kappa\nabla T) + \nabla\cdot\left(\frac{5k_BT}{2e}\mathbf{j}\right) + \frac{\mathbf{j}\cdot\mathbf{j}}{\sigma} + Q_m - Q_R \qquad [2]$$
$$Q_m = \nabla\cdot(\boldsymbol{\tau}_{ij}\cdot\mathbf{u}) - \frac{\partial}{\partial t}(\rho K) - \nabla\cdot(\rho\mathbf{u}K) + \frac{\partial P}{\partial t}$$

$$\nabla\cdot\mathbf{j} = 0, \qquad \text{with } \mathbf{j} = -\sigma\left(\nabla\phi + \frac{\partial\mathbf{A}}{\partial t} - \mathbf{u}\times\mathbf{B}\right) \qquad [3]$$
$$\nabla^2\mathbf{A} = -\mu_0\mathbf{j}, \qquad \text{with } \mathbf{B} = \nabla\times\mathbf{A}$$

In Equations 1 to 3, ρ is the plasma density, **u** is the velocity field, P is the pressure, τ_{ij} is the viscous stress tensor, j is the current density, **B** is the magnetic flux density, h is the enthalpy, κ is the thermal conductivity, T is the temperature, σ is the electrical conductivity, $K=(½)\ |\mathbf{u}|^2$ is the specific kinetic energy, Q_r is the thermal radiation loss, ϕ is the electric potential, and **A** is the magnetic vector potential. The system of equations is solved subject to boundary conditions described by the authors in previous publications (Reynolds, 2020; Reynolds et al., 2026).

Results and discussion

Three sets of conditions were considered for the DC FeCr smelting process: one with a carbon feed fraction as per normal operations, one with 33% lower carbon feed, and one with 25% higher. The gas phase compositions for each condition were obtained from thermochemical modelling at a range of different slag bath temperatures from a representative process temperature, 1800 °C, up to the point at which no solid or liquid phases remain, approximately 3500 °C. Temperatures approaching the boiling point of process slags are possible in the region where the extremely hot arc plasma connects to the molten bath surface (Barcza et al., 1990), and it is likely that the freeboard gas in the region near to the arc will be partially contaminated with this "vaporised" process material. The gas compositions for each process condition and slag temperature were then used to calculate the associated plasma properties as a function of plasma temperature, and the properties were passed into the MHD arc model to simulate the resulting arc behaviour in an industrial DC FeCr furnace.

Freeboard gas compositions

Thermochemical simulations were performed in the Equilib module of FactSage 8.0. For the gaseous species, the FactPS database was used, with the "include gaseous plasma" option turned on. For oxides, slag, and alloy, the FTOxid and SGTE2017 solution databases were used, respectively. Simulations were done assuming pure SiO_2 and CaO as fluxes, and pure C as reductant. The ore composition used was for a typical LG6 concentrate from the western limb of the Bushveld Complex. The composition, in mass%, was: 15.29% Al2O3, 0.36% CaO, 42.65% Cr_2O_3, 24.78% FeO, 10.65% MgO, 0.21% MnO, 4.54% SiO_2, and 0.64% TiO_2 (Swanepoel et al., 2022). Calculations were performed across a temperature range of 1550 °C to 3500 °C in steps of 5 °C, spanning from the alloy tapping temperature up through the operating temperature range of the DC furnace (nominally ~1800 °C) and beyond. Alloy chemistry and phase equilibria were evaluated at 1550 °C, representative of the alloy tap temperature, while slag chemistry was assessed at 1800 °C, representative of the process temperature. This staged approach provides a consistent baseline for comparing simulation cases. It is acknowledged that industrial smelting does not proceed at full thermodynamic equilibrium; the simulated values are therefore indicative of expected trends rather than absolute predictions. The simulation for the normal case had a target CaO/SiO_2 mass ratio in the slag of 0.87, with a target Si content in the alloy of 0.2% at 1550 °C, based on pilot plant trials of MG-chromite at Mintek (Geldenhuys, 2013). For the under- and over-carbon simulations, the reductant quantity was 33% lower and 25% higher than the normal case, respectively, and was chosen such that the alloy would fall outside of customer specification: insufficient Cr recovery in the under-carbon case, and excessive Si in the over-carbon case.

The results of the thermochemical calculations are shown in Figure 2. In all conditions the gas phase is dominated by the reaction product carbon monoxide. However, it can be seen that trace metallic elements contaminate the gas to some degree in all cases, except for the lowest slag temperatures. As a general trend the fraction of metallic contaminants increases as the slag temperature rises, as a result of the increasing vapour pressure of the oxide components. Magnesium is the most volatile of the slag components, followed by silicon (in the form of SiO gas). Iron and chromium, although not particularly volatile, are also present in significant quantities due to their high concentrations in the feed ore.

The effect of increasing the reductant fraction in the feed mix is quite marked. Magnesium and silicon evaporation begins at lower slag temperatures and reaches higher levels as the reductant fraction is increased. The opposite behaviour is observed for iron and chromium, but this is a weaker trend and may simply be a dilution effect due to the increase in the other metallic components. Of the more minor components, calcium and aluminium start to appear in significant quantities only in the over-carbon case.

Plasma properties

The elemental gas compositions obtained for each reductant condition were used as inputs to a parallelised calculation of the associated plasma thermophysical properties at a range of selected slag temperatures. The full set of plasma species considered included Al, Cr, Mg, Fe, Mn, Ca, Ti, C, and O in atomic form; Alz+, Crz+, Mgz+, Fez+, Mnz+, Caz+, Tiz+, Cz+, and Oz+ as ions (where z denotes the charge number, ranging from 1 to 3), and CO, CO_2, O2, MgO, AlO, SiO, CaO, TiO, CrO, and FeO as molecular species. Calculations were performed using minplascalc

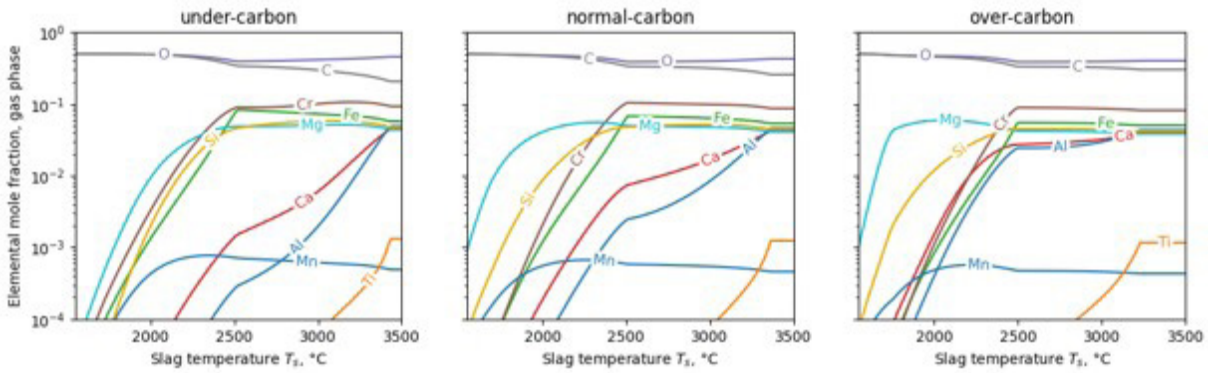

Figure 2—Elemental molar composition of gas phase in equilibrium with FeCr process alloy and slag for different reductant contents in feed

1.0.2, with the required quantum mechanical data for each species obtained from sources documented in Reynolds et al. (2025a). To improve computational efficiency, species of which the constituent elements were absent or negligible in the FactSage gas composition were excluded from the calculations. Plasma composition and thermophysical property calculations were carried out over the temperature range 300 K – 25000 K at a pressure of one atmosphere. At temperatures below 2000 K, reduced species sets were employed to avoid numerical instabilities arising from charged-particle concentrations approaching machine precision.

Plasma property results for gas compositions at slag temperatures of 1800 °C are shown in Figure 3. At this temperature, the freeboard gas is mostly CO with small amounts of Mg and Si. The effect of changing the carbon balance is negligible for all properties, with the exception of electrical conductivity in the temperature range between 5000 K and 10000 K, and the radiation emission coefficient between 2500 K and 15000 K. For both of these properties increasing the carbon fraction in the feed results in higher values, mainly due to the increase in metallic contaminants, which ionise more easily at lower plasma temperatures.

Properties for gas compositions at slag temperatures of 3500 °C are shown in Figure 4. At such elevated temperatures the freeboard gas is heavily contaminated with a large number of metallic species and additional oxygen from the evaporating slag. Interestingly, the overall effect of this is to move the influence of the carbon balance away from the electrical conductivity and radiation emission properties, which are almost identical, to the heat transfer properties of heat capacity and thermal conductivity. These show some differences in the low-temperature peaks, with increased carbon in the feed mixture resulting in higher peaks.

MHDmodelling

Computational multiphysics simulations of the arc in an industrial-scale DC arc furnace were set up using the properties calculated in the afore-mentioned. Separate cases were generated for each combination of slag temperature and reductant balance, with common parameters, as shown in Table 1.

A hemispherical region of the freeboard around the arc was simulated in each case. This region included the arc as well as the tip portion of the electrode and the surface of the slag bath (see Figure 5). Free inflow/outflow boundaries were applied at the surface of the hemisphere to allow mass and energy to be exchanged with the bulk furnace freeboard gas. Although the arc can create a significant depression in the molten slag bath surface at industrial scales due to the stagnation force of the jet (Bowman, Krüger, 2009), this effect was ignored in the present work for the purpose of simplification.

For each model case the calculation was conducted in two stages. In the first stage, using a low-resolution mesh, the arc was initiated in a stagnant region of plasma and simulated until representative flow patterns became established and initial conditions decayed away (typically 100 ms). In the second stage, the model was bootstrapped on the full-resolution mesh using interpolated field values from the first stage and operated for an additional 50 ms to generate data for analysis. Arc voltages were recorded at regular intervals during the simulation as the difference between the minimum and maximum of the electric potential field. The trends were then post-processed using Python scripts to obtain statistical properties of the arc voltage.

Voltages from the model cases for different reductant mixes and slag temperatures are given in Figure 6. It is immediately obvious

Table 1
MHD model parameters for FeCr arc simulations

Parameter	Value
Electrode diameter	0.75 m
Arc length	0.4 m
Arc current	75 kA
Cathode spot current density	1 kA/cm^2
Vaporisation temperature (cathode)	4100 K
Vaporisation temperature (anode)	3500 K
Bulk freeboard temperature	1800 K
Time simulated	50 ms
Mesh resolution (arc region)	4 mm

that the slag temperature at which the freeboard gas is generated has a very strong effect on both the magnitude and behaviour of the voltages; lower temperatures produce higher arc voltages, and more chaotic and unstable operation with large variations over short time scales. In contrast, the effect of reductant balance appears to be rather negligible, especially at higher slag temperatures.

The differences in arc structure and dynamics are visible in Figure 7, where instantaneous temperature fields are compared between the T_s = 1800 °C and 3500 °C cases using the plasma properties associated with the normal-carbon balance. The effective slag temperature has a dramatic effect on the arc stability with higher values of T_s producing relatively compact, steady, and symmetrical arc jets compared to the turbulent flow patterns and highly distorted and chaotic shapes that are seen at lower values.

A statistical analysis of the voltage traces shown in Figure 6(a) for a slag temperature of 1800 °C is shown in Figure 8. Although there are some differences, these are not particularly significant and the averages lie within one standard deviation of one another – this confirms that there is no consistent upward or downward trend in the arc voltages with carbon addition. Given that some differences were observed in both the freeboard gas compositions and the plasma properties as the reductant balance was changed, it is of interest to further investigate this.

In the next set of cases, the sensitivity of the system to the two plasma properties that showed the most differences in Figure 3, plasma electrical conductivity σ and total radiation emission coefficient ε_{tot}, was examined. This was done by holding all properties fixed and equal to the normal-carbon condition except for the property being examined, values for which were taken from the relevant over- or under-carbon plasma property dataset. This allows the effect of the individual property to be isolated.

The Effect of electrical conductivity

The effect of electrical conductivity on the arc simulation results are shown in Figure 9 and Figure 10. It is clear that less reductant in the process feed results in a higher arc voltage, at least for the under-carbon case, where the results are statistically well-separated.

It is likely that this trend is due to the increase in plasma electrical conductivity that accompanies increased reductant addition. Increasing electrical conductivity would be expected to produce a more conductive arc and, hence, a lower voltage if all other parameters are kept the same.

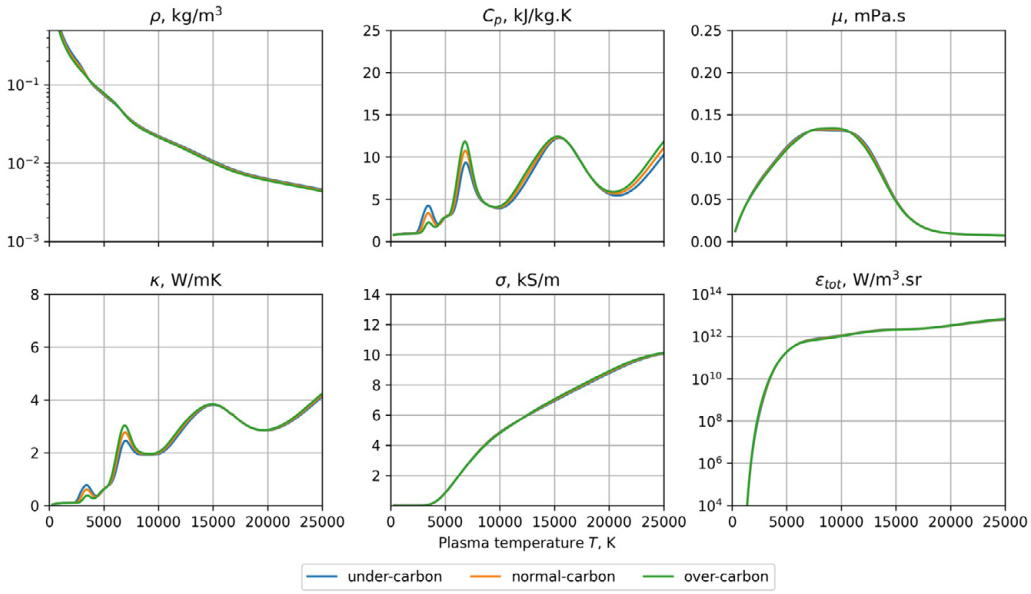

Figure 3—Plasma properties for gas compositions associated with FeCr slag at Ts = 1800 °C; clockwise from top left: density, heat capacity, viscosity, total radiation emission, electrical conductivity, and thermal conductivity

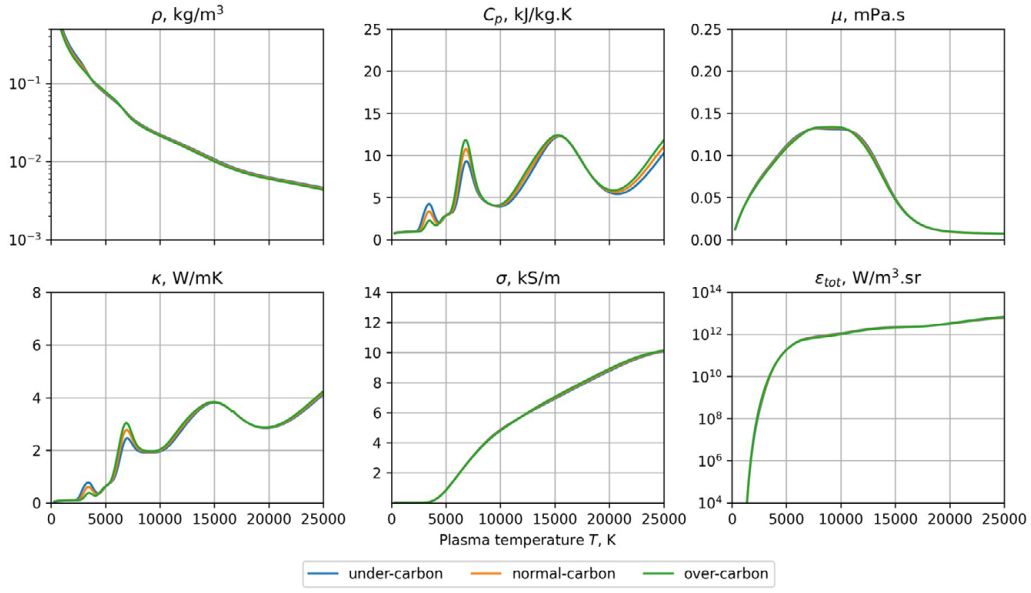

Figure 4—Plasma properties for gas compositions associated with FeCr slag at Ts = 3500 °C; clockwise from top left: density, heat capacity, viscosity, total radiation emission, electrical conductivity, and thermal conductivity

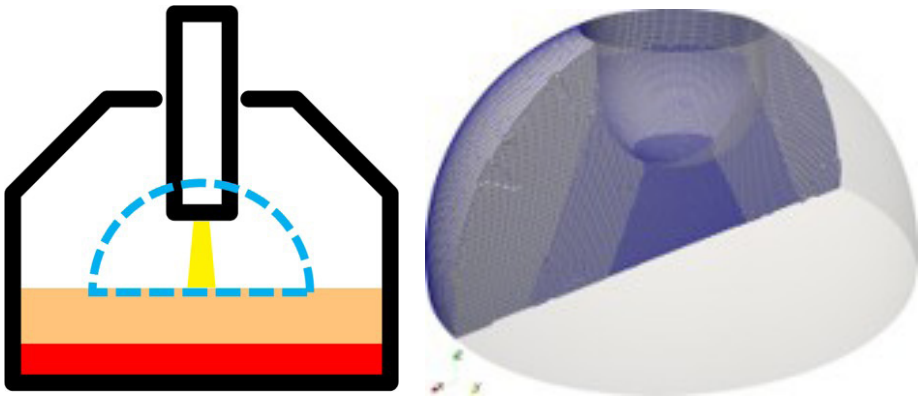

Figure 5—(l) schematic of DC furnace interior showing region modelled in blue outline, (r) rendering of model domain showing finite-volume mesh elements

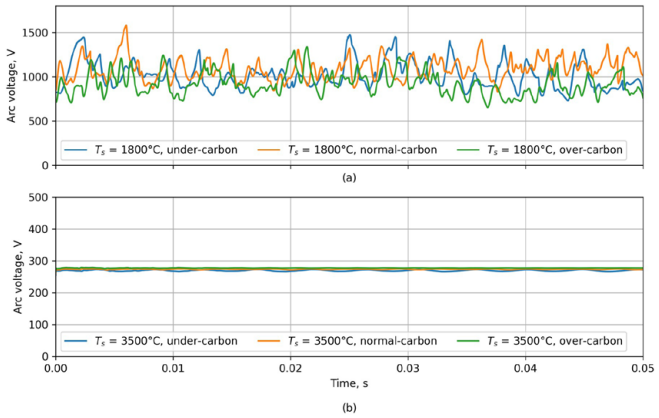

Figure 6—Arc voltages at 75 kA current and 0.4 m arc length, (a) slag temperature 1800 °C, (b) slag temperature 3500 °C

Effect of total radiation emission coefficient

In Figure 11 and Figure 12 the effect of changing the total radiation emission coefficient is shown. With all other properties kept the same the effect of increasing the carbon addition is to decrease the arc's conductivity, producing higher voltages. This is due to the increased reductant in the feed producing a freeboard gas, which generates a more emissive plasma, and although the interplay between absorption and emission can be complex in general three-dimensional arc structures, the nett effect in this particular case is that the arc column loses more energy by radiation as the emission coefficient increases. This cools the plasma and reduces the arc conductivity. As with the electrical conductivity, the effect is most marked for the under-carbon case, whereas the normal- and over-carbon cases are harder to distinguish statistically.

Comparing Figure 10 and Figure 12 with Figure 8 shows that the two plasma properties, which are most affected by the reductant balance at 1800 °C have an opposing effect; as carbon fraction

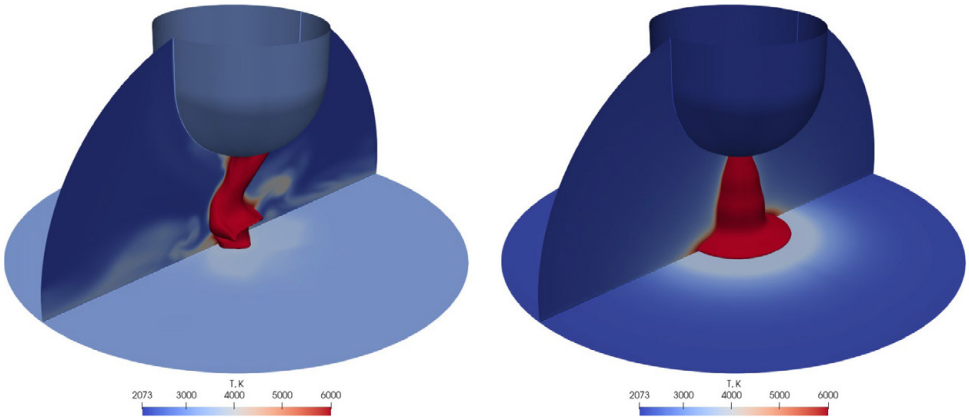

Figure 7—Visualisations of arc temperature field at 75 kA current, 0.4 m arc length, and normal-carbon balance, (l) slag temperature 1800 °C, (r) slag temperature 3500 °C

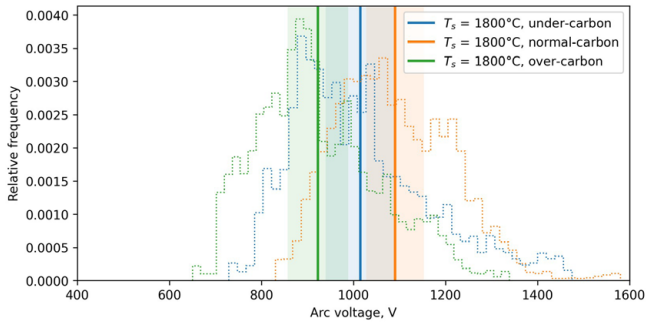

Figure 8—Statistical frequency plots of arc voltages at 75 kA current, 0.4 m arc length, and slag temperature 1800 °C (solid vertical lines are averages, and shaded areas are one standard deviation)

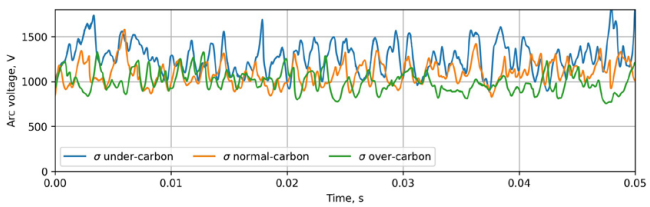

Figure 9—Arc voltages showing the isolated effect of plasma electrical conductivity at slag temperature 1800 °C

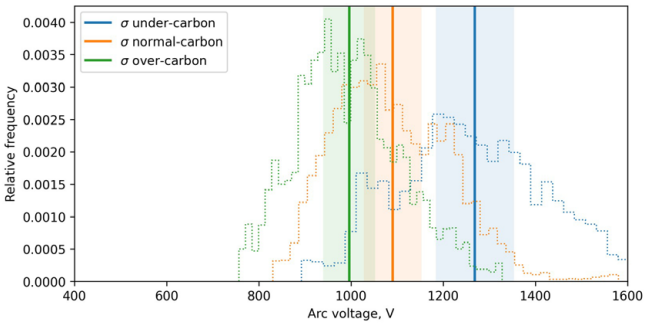

Figure 10—Statistical frequency plots of arc voltages showing the isolated effect of plasma electrical conductivity at slag temperature 1800 °C (solid vertical lines are averages, and shaded areas are one standard deviation)

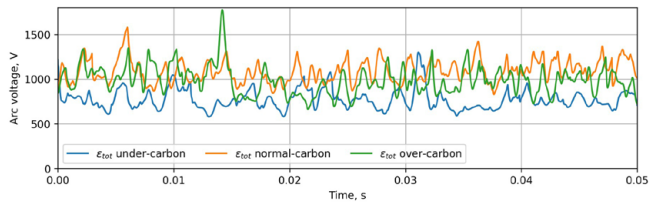

Figure 11—Arc voltages showing the isolated effect of radiation emission coefficient at slag temperature 1800 °C

increases, the electrical conductivity acts to make the arc less resistive as carbon fraction increases, while the emission coefficient acts to make it more resistive. For the particular set of conditions examined in the present work, it is interesting to note that the two effects are almost in balance and produce arcs with similar electrical properties.

Conclusions

A multi-stage computational modelling workflow was applied to the problem of plasma arc behaviour in DC furnaces for carbothermic FeCr production. In particular, the effect of changing the proportion of carbon reductant in the feed to the furnace was studied using a range of numerical calculation and simulation tools.

The equilibrium freeboard gas composition was significantly affected by the change in reductant balance, becoming progressively more contaminated with volatile species such as Mg and Si as the proportion of carbon was increased. This was, however, a second-order effect compared to increasing the effective slag temperature, which produced gases with much higher concentrations of metallic contaminants. Examining the thermophysical properties of plasmas arising from the different process gas compositions then showed that, at low slag temperatures the electrical conductivity and total radiation emission coefficient were most strongly affected, with both increasing as the reductant proportion in the feed was increased. At higher slag temperatures there was minimal effect of changing the reductant fraction, with only the peak values of thermal conductivity and heat capacity being affected over relatively small plasma temperature ranges. Finally, computational MHD simulations of arcs at scales comparable to industrial furnaces showed that changing the reductant balance in the feed had relatively little effect on the arc resistances and voltages produced. This was especially obvious at higher slag temperatures, where metal-contaminated arc plasmas all have similar properties. At lower slag temperatures, a basic sensitivity study showed that increasing electrical conductivity (associated with increasing reductant fraction) caused the arc to be less resistive, whereas increasing radiation emission coefficient (associated with increasing reductant fraction) caused more resistive arcs. Although both effects are quite strong in isolation, when acting together, they largely compensate for each other and produce arcs which display similar electrical behaviour.

It therefore seems unlikely that changes in feed reductant balance are the underlying cause of the large excursions in the electrode hoist position that are occasionally observed on operating DC furnace plants, at least in terms of the mechanism discussed in the present work, whereby the reductant balance affects the freeboard gas composition and plasma properties. Future work in this area would be best directed toward studying the impact of feed contaminants such as moisture or organic volatiles, understanding the effective slag temperature and how to estimate appropriate values for it, and improving the performance of the computational models so that larger sets of data can be generated and analysed for improved statistical significance.

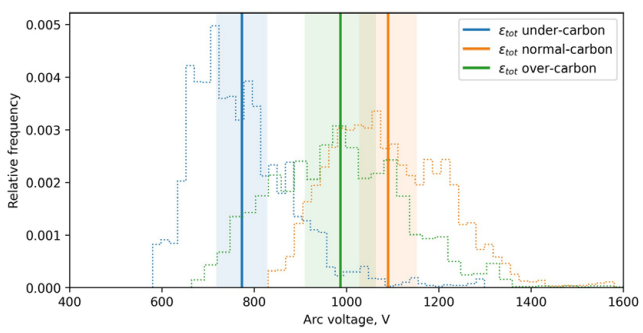

Figure 12—Statistical frequency plots of arc voltages showing the isolated effect of radiation emission coefficient at slag temperature 1800 °C (solid vertical lines are averages, and shaded areas are one standard deviation)

Acknowledgements

This paper is published with the permission of Mintek, and was supported by funding on Mintek Science Vote project IntelliMetTwin MCR-62604. The authors acknowledge the Centre for High Performance Computing (CHPC), South Africa, for providing computational resources for this research project.

References

Akhmetov, A., Zulhan, Z., Sadyk, Z., Burumbayev, A., Zhakan, A., Kabylkanov, S., Toleukadyr, R., Saulebek, Z., Ayaganova, Z., Makhambetov, Y. 2025. Carbon-Free Smelting of Ferrochrome Using FeAlSiCa Alloy. Processes vol. 13, pp. 1745. https://doi.org/10.3390/pr13061745

Bale, C.W., Bélisle, E., Chartrand, P., Decterov, S.A., Eriksson, G., Gheribi, A.E., Hack, K., Jung, I.-H., Kang, Y.-B., Melançon, J., Pelton, A.D., Petersen, S., Robelin, C., Sangster, J., Spencer, P., Van Ende, M.-A. 2016. *FactSage thermochemical software and databases*, 2010–2016. Calphad vol. 54, pp. 35–53. https://doi.org/10.1016/j.calphad.2016.05.002

Barcza, N.A., Curr, T.R., Jones, R.T. 1990. Metallurgy of open-bath plasma processes. *Pure and Applied Chemistry.* vol. 62, pp. 1761–1772. https://doi.org/10.1351/pac199062091761

Boulos, M.I., Fauchais, P.L., Pfender, E. 2023. Plasma in the Metallurgical Industry, in: Boulos, M.I., Fauchais, P.L., Pfender, E. (Eds.), Handbook of Thermal Plasmas. *Springer International Publishing*, Cham, pp. 1581–1660. https://doi.org/10.1007/978-3-030-84936-8_38

Bowman, B., Krüger, K. 2009. Arc Furnace Physics. Verlag Stahleisen GmbH, Düsseldorf, Germany.

Dalaker, H., Hovig, E.W. 2023. Hydrogen Plasma-Based Reduction of Metal Oxides, in: Fleuriault, C., Steenkamp, J.D., Gregurek, D., White, J.F., Reynolds, Q.G., Mackey, P.J., Hockaday, S.A.C. (Eds.), Advances in Pyrometallurgy, *The Minerals, Metals & Materials Series*. Springer Nature Switzerland, Cham, pp. 85–94. https://doi.org/10.1007/978-3-031-22634-2_8

Gasik, M. (Ed.). 2013. Handbook of ferroalloys: Theory and Technology. Elsevier/Butterworth-Heinemann, Amsterdam.

Geldenhuys, I.J. 2013. Aspects of DC chromite smelting at Mintek - an overview, in: Efficient Technologies in Ferroalloy Industry: Proceedings of the Thirteenth International Ferroalloys Congress, International Ferroalloys Congress. Presented at the 13th International Ferroalloys Congress, *Public Association INFACON XIII,* Almaty, Kazakhstan, pp. 31–47.

Geldenhuys, I.J. 2017. The Exact Art and Subtle Science of DC Smelting: Practical Perspectives on the Hot Zone. JOM 69, pp. 343–350. https://doi.org/10.1007/s11837-016-2171-z

Jones, R.T. 2014. DC arc furnaces – past, present, and future, in: Celebrating the Megascale: Proceedings of the Extraction and

Processing Division Symposium on Pyrometallurgy in Honor of David G.C. Robertson. Presented at the TMS Annual Meeting 2014, *TMS (The Minerals, Metals & Materials Society)*, pp. 129–139.

Kjellberg, B., Stenkvist, S.E. 1989. DC Technology for Smelting Furnaces, in: INFACON '89: The 5th International Ferroalloys Congress. Presented at the 5th International Ferroalloys Congress (INFACON V), *The Ferroalloys Association*, New Orleans, USA, pp. 88–94.

OpenCFD Ltd. 2025. OpenFOAM v2506, https://www.openfoam.com/ [WWW Document]. URL https://www.openfoam.com/ (accessed 8.17.25).

Oterdoom, H., Reuter, M., Zietsman, J. 2025. DC Ferrochrome Smelting: The Arcing Zone and Its Influence on Energy Transport and Exergy Dissipation. *Metallurgical and Materials Transactions B* vol. 56, pp. 890–912. https://doi.org/10.1007/s11663-024-03365-y

Reynolds, Q.G. 2020. Toward computational models of arc dynamics in silicon smelters, in: 14th International Conference on CFD in the Oil & Gas, Metallurgical and Process Industries. *Presented at the 14th International Conference on CFD in the Oil & Gas, Metallurgical and Process Industries, SINTEF Academic Press*, Trondheim, Norway, pp. 99–106.

Reynolds, Q.G., Bowman, B., Erwee, M.W., Geldenhuys, I.J., Sandrock, C., Venter, G.A., Xakalashe, B.S., Zietsman, J. 2025a. Plasma soup for the pyrometallurgist's soul. J. *South African Institute of Mining and Metallurgy*. vol. 125, pp. 129–144. https://doi.org/10.17159/2411-9717/758/2025

Reynolds, Q.G., Sandrock, C., Goutier, P.-A., 2025b. minplascalc, https://github.com/quinnreynolds/minplascalc/releases/tag/v1.0.2.

Reynolds, Q.G. 2026. plasmaArc, https://github.com/quinnreynolds/plasmaArc/releases/tag/v1.1.1-openfoam-v2512.

Reynolds, Q.G., Xakalashe, B.S., Tsebe, S.P., Erwee, M.W., Jones, R.T., Geldenhuys, I.J. 2026. Plasma arc behaviour in DC arc furnace smelting of PGM-bearing materials: a modelling study on the effect of reductant choice. J. *South African Institute of Mining and Metallurgy*. Article in press.

Sager, D., Grant, D., Stadler, R., Schreiter, T. 2010. Low cost ferroalloy extraction in DC-arc furnace at Middelburg Ferrochrome, in: Proceedings of the Twelfth International Ferroalloys Congress - Sustainable Future. *Presented at the 12th International Ferroalloys Congress (INFACON XII)*, Outotec Oyj, Helsinki, Finland, pp. 803–814.

Sommerfeld, M., Botinha, R., Friedrich, B. 2024. Enabling CO2 neutral metallurgy for ferrochromium production using bio-based reducing agents. Scientific Reports. vol. 14, pp. 10878. https://doi.org/10.1038/s41598-024-61700-4

Swanepoel, S., Garbers-Craig, A.M., De Villiers, J.P.R. 2022. The Oxidation Behavior of a Selection of South African Chromites. Metallurgical and Materials Transactions B vol. 53, pp. 3805–3824. https://doi.org/10.1007/s11663-022-02643-x ◆

NATIONAL & INTERNATIONAL ACTIVITIES

2026

30-31 July 2026 — Critical Minerals 2026 Conference
From Potential To Prosperity – Building Africa's Critical Minerals Value Chains Through Collaboration, Innovation and Governance
Royal Majestic Hotel, Rosebank, Johannesburg
Contact: Gugu Charlie
Tel: 011 538-0238
E-mail: gugu@saimm.co.za
Website: http://www.saimm.co.za

18-20 August 2026 — CAVING 2026
Ulaanbaatar, Mongolia
Website: https://www.acgcaving.com/

18-21 August 2026 — SAIMM Uranium Conference 2026
Swakopmund Hotel and Entertainment Centre, Swakopmund, Namibia
Contact: Gugu Charlie
Tel: 011 538-0238
E-mail: gugu@saimm.co.za
Website: http://www.saimm.co.za

26-27 August 2026 — ESGS Climate Change in Mining Conference 2026
Climate Change in Mining: Risks, Governance, Sustainability, and Environmental Management
Glenburn Lodge, Muldersdrift
Contact: Gugu Charlie
Tel: 011 538-0238
E-mail: gugu@saimm.co.za
Website: http://www.saimm.co.za

22-25 September 2026 — XIX International Society for Mine Surveying Congress 2026
Century City, Cape Town
Contact: Gugu Charlie
Tel: 011 538-0238
E-mail: gugu@saimm.co.za
Website: http://www.saimm.co.za

7-11 September 2026 — Electra Mining Africa 2026
Expo Centre, Nasrec, Johannesburg
Contact: Gugu Charlie
Contact: Camielah Jardine
Tel: 011 538-0237
Website: http://www.saimm.co.za

21-24 September 2026 — XIX 2026 International Society for Mine Surveying Congress
Century City, Cape Town
Contact: Gugu Charlie
Tel: 011 538-0238
Website: http://www.saimm.co.za

29-30 September 2026 — 7TH Young Professionals Conference 2026
Mintek, Randburg, Johannesburg
Contact: Gugu Charlie
Tel: 011 538-0238
E-mail: gugu@saimm.co.za
Website: http://www.saimm.co.za

12-16 October 2026 — 19TH South African Geophysical Association Conference 2026
Lagoon Beach Hotel & Spa, Cape Town
Website: https://sagaconference.co.za/

18-22 October 2026 — IMPC 2026 XXXII International Mineral Processing Congress
Empowering a future-fit mineral processing industry
Cape Town, South Africa
Contact: Camielah Jardine
Tel: 011 538-0237
E-mail: camielah@saimm.co.za
Website: http://www.saimm.co.za

4-6 November 2026 — Southern African Mine Water Conference 2026
Let's Connect
Glenburn Lodge, Muldersdrift
Contact: Gugu Charlie
Tel: 011 538-0238
E-mail: gugu@saimm.co.za
Website: http://www.saimm.co.za

11-13 November 2026 — MineSafe 2026 Mine Health and Safety Conference
Engineering Health & Safety For Sustainable Future-Ready Mines
Gallagher Convention Centre, Johannesburg, South Africa
Contact: Gugu Charlie
Tel: 011 538-0238
E-mail: gugu@saimm.co.za
Website: http://www.saimm.co.za

5-9 April 2027 — Hoist and Haul 2027
Century City, Cape Town
Contact: Gugu Charlie
Tel: 011 538-0238
E-mail: gugu@saimm.co.za
Website: http://www.saimm.co.za

Company affiliates

The following organizations have been admitted to the Institute as Company Affiliates

Agreenco Environmental Projects
OPTRON
Wekaba Engineering (Pty) Ltd
Jones & Wagener Pty Ltd
CYMOT (PTY) Ltd
Kelnir Projects (Pty) Ltd
DQS Pty Ltd
M84 Geotech Pty Ltd
Sulzer Pumps (South Africa) (Pty) Ltd
EKATO South Africa
CARBOCRAFT (PTY) LTD
Solenis
Pump and Abrasion Technologies (PTY) Ltd
CIGroup ACE Pty Ltd
Sebotka (Pty) Ltd
Mech-Industries (Pty) Ltd
Anton Paar Southern Africa
Trans-Caledon Tunnel Authority
acQuire Technology Solutions
EHL Consulting Engineers (Pty) Ltd
DDP Specialty Products South Africa (Pty) Ltd
Allied Furnace Consultants
Gravitas Minerals (Pty) Ltd
Mining Projection Concepts (Pty) Ltd
African Pegmatite
Ex Mente Technologies (Pty) Ltd
MLB Investments CC
Micromine Africa (Pty) Ltd
Ingwenya Mineral Processing
Maptek (Pty) Ltd
G H H Mining Machines (Pty) Ltd
OPTRON
Geobrugg Southern Africa (Pty) Ltd
Ivanhoe Mines SA
Weir Minerals Africa
Herrenknecht AG
Becker Mining (Pty) Ltd
Rosond (Pty) Ltd
Sound Mining Solution (Pty) Ltd
Roytec Global (Pty) Ltd
Caledonia Mining South Africa
Elbroc Mining Products (Pty) Ltd
Modular Mining Systems Africa (Pty) Ltd
Paterson & Cooke Consulting Engineers (Pty) Ltd
SENET (Pty) Ltd
Tomra (Pty) Ltd
Ukwazi Mining Solutions (Pty) Ltd
Arcus Gibb (Pty) Ltd
SRK Consulting SA (Pty) Ltd
ZUTARI (Pty) Ltd
Minerals Council of South Africa
Bluhm Burton Engineering Pty Ltd
Hatch (Pty) Ltd
Anglogold Ashanti Ltd
Digby Wells and Associates
AMIRA International Africa (Pty) Ltd
Malvern Panalytical (Pty) Ltd
MineRP Holding (Pty) Ltd
FLSmidth Minerals (Pty) Ltd
Glencore
Murray & Roberts Cementation (Pty) Ltd
Redpath Mining (South Africa) (Pty) Ltd
Sibanye Gold Limited
AECI Mining Chemicals, a division of AECI Mining Ltd
Exxaro Resources Limited
IMS Engineering (Pty) Ltd
Rustenburg Platinum Mines Limited - Union
Impala Platinum Holdings Limited
Mintek

IMPC 2026

XXXII INTERNATIONAL MINERAL PROCESSING CONGRESS
18 - 22 OCTOBER 2026 CAPE TOWN SOUTH AFRICA

www.impc2026.com

Empowering a future-fit mineral processing industry

We would like to invite you to attend the
XXXII International Mineral Processing Congress
in Cape Town, South Africa from **18 - 22 October 2026**

IMPC 2026 will be hosted by the Southern African Institute of Mining and Metallurgy (SAIMM)

IMPC
INTERNATIONAL MINERAL PROCESSING COUNCIL

SAIMM
THE SOUTHERN AFRICAN INSTITUTE OF MINING AND METALLURGY

Photo courtesy CTICC

CAPE TOWN INTERNATIONAL CONVENTION SQUARE
1 LOWER LONG STREET
CAPE TOWN 8001

THE SAIMM

IMPC 2026 will be hosted by the Southern African Institute of Mining and Metallurgy (SAIMM). The SAIMM has been in existence for 130 years, having been established in 1894 as a 'learned society' to support mining and metallurgical professionals during the emergence and growth of the early South African minerals industry.

Mining is of great importance to Africa in general, and particularly to Southern Africa. Africa accounts for a major portion of the world's mineral reserves and more than half of gold, platinum group metals, cobalt and diamonds. Southern Africa produces over two-thirds of Africa's mineral exports by value.

CAPE TOWN INTERNATIONAL CONVENTION CENTRE

IMPC 2026 will be hosted at the Cape Town International Convention Centre (CTICC). Since the inception of the CTICC in 2003, Cape Town has been proudly the number one destination for conferences in Africa, according to the latest International Congress and Convention Association (ICCA) statistics.

Cape Town, the "Mother City", is the oldest city in South Africa and has a cultural heritage spanning more than 300 years. Cape Town is a modern, cosmopolitan city and is often rated as one of the premier world holiday destinations. The city has a large range of hotels & guest houses and modern transport infrastructure. The city has numerous activities & attractions, including Table Mountain, Robben Island, Cape Point, the Castle, V&A Waterfront, world class beaches, wine farms, nature reserves, scenic drives, hiking, whale watching, shark cage diving and fine dining.

MINE SAFE 2026
MINE HEALTH AND SAFETY CONFERENCE

ENGINEERING HEALTH & SAFETY FOR SUSTAINABLE FUTURE-READY MINES

HYBRID CONFERENCE

11-12 NOVEMBER 2026 – CONFERENCE
13 NOVEMBER 2026 – INDUSTRY AWARDS DAY
GALLAGHER CONVENTION CENTRE, JOHANNESBURG, SOUTH AFRICA

ZERO HARM

Abstract submission – 31 July 2026 I Extended Abstract/Papers submission- 31 August 2026

BACKGROUND

We are excited to announce our upcoming industry Conference and Industry Awards Day, dedicated to advancing mining safety and health, innovation, and sustainability and recognising the excellent work in creating ZERO HARM future ready mines.
This year's theme, "Engineering Health, Safety for Sustainable Future-Ready Mines", underscores our collective commitment to achieving zero harm while embracing modernisation, technology, and collaboration as the foundation for safer, future-ready mining operations.

This conference will serve as a vital platform for knowledge-sharing and idea exchange among key stakeholders, including mining companies, the Department of Mineral Resources and Energy (DMRE), the Minerals Council South Africa, labour unions, and health and safety practitioners at all levels in the minerals industry.

CONFERENCE THEMES

1. Driving Zero Harm Forward
- Reinforcing the vision of eliminating fatalities.
- Sharing progress, lessons learned, and renewed commitments.

2. Technology in Action
- Case studies of mines implementing breakthrough technologies.
- Practical examples of problems solved through innovation.

3. Future-Ready Mine Design
- Strategies for long-term sustainability and resilience.
- Integrating safety and health into planning and operational frameworks.

4. Engineering Safety Excellence
- Advances in engineering solutions that enhance safety.
- Best practices in design, maintenance, and risk management.

5. Engineering in the Digital Age
- Modernisation and digital transformation in mining operations.
- Leveraging data, automation, and AI for safer outcomes.

6. Technology Advancements and Innovation
- Exploring robotics, wearables, sensors, and predictive analytics.
- Emerging technologies shaping the future of mining safety.

7. Health and Wellbeing in Mining
- Protecting workers' physical and mental health.
- Occupational health strategies, wellness programs, and medical innovations.

8. Sustainability and Responsible Mining
- Environmental stewardship and climate-conscious practices.
- Linking safety with sustainability for long-term industry resilience.

Why Attend?
- Gain insights from global case studies and pioneering projects.
- Network with industry leaders, engineers, and technology innovators.
- Explore practical solutions for building safer, sustainable mines.
- Be part of shaping the future of mining through collaboration and innovation.

Join us as we work together towards Safe Mines, Healthy Lives, and Sustainable Futures!

PARTNERSHIP OPPORTUNITIES

Sponsorship opportunities are available. Companies wishing To partner on this event should contact the Conference Coordinator.

WHO SHOULD ATTEND

The conference should be of value to:
- Safety practitioners
- Mine management
- Mine health and safety officials
- Engineering managers
- Underground production supervisors
- Surface production supervisors
- Environmental scientists
- Minimizing of waste
- Operations manager
- Processing manager
- Contractors (mining)
- Including mining consultants, suppliers and manufacturers
- Education and training • Energy solving projects
- Water solving projects
- Unions
- Academics and students
- DMRE
- Occupational health practitioners
- Leadership and ManagementTechnical and Engineers

SUBMIT AN ABSTRACT

CALL FOR PAPERS

Call for papers on the topics of safety, health and environment
Prospective authors are invited to submit titles and abstracts of their presentations in English and not longer than 500 words. Abstracts should be submitted to:
Include Abstract Submission Deadline: **31 July 2026**
Extended Abstract/Paper Submission: **31 August 2026**

For further information contact:
Gugu Charlie, Conference Co-ordinators
E-mail:gugu@saimm.co.za | Tel: +27 11 538-0238
| Web: www.saimm.co.za